LA-12651-T
Thesis

UC-413
Issued: November 1993

Elastic Scattering of Pions from Tritium and ^{3}He in the Backward Hemisphere in the Region of the $\Delta_{33}(1232)$ Resonance

Scott K. Matthews*

*Graduate Research Assistant at Los Alamos Group MP-10 and N-2. The George Washington University, Department of Physics, Washington, DC 20052.

Los Alamos
NATIONAL LABORATORY
Los Alamos, New Mexico 87545

ACKNOWLEDGMENTS

Many people have taken time and effort beyond what was required, to help me understand some physics, and maybe produce something worthwhile; I would like to thank them here.

First, my advisor, Dr. Bill Briscoe, and my unofficial advisors, Dr. Steve Greene and Dr. Ben Nefkens, who have all tried to help me develop my abilities as well as my goals.

The faculty at The George Washington University have been good friends to me over the years, interested in my life as well as my work. I especially thank Dr. Herman Hobbs and Dr. Francisco Prats for their friendship and advice, and Dr. Barry Berman, Dr. Kalvir Dhuga and Dr. Morton Taragin, for their efforts on the experiments and analysis.

At Los Alamos, I have been made welcome in two groups, MP-10 and N-2. I thank the managements of these groups for providing me with resources and experience, and their members for their advice and comradarie.

Over the years I have been supported by N-2 as a Graduate Research Associate, by The George Washington University as a Teaching Fellow, and by the National Science Foundation, through the research grant of Bill Briscoe and collaborators, as a Research Assistant. I gratefully acknowledge the commitment of all of these to education and research.

Contents

List of Tables

List of Figures

ELASTIC SCATTERING OF PIONS FROM TRITIUM AND ^{3}HE IN THE BACKWARD HEMISPHERE IN THE REGION OF THE Δ_{33}(1232) RESONANCE

by

Scott K. Matthews

ABSTRACT

Several experiments have measured nominally-charge-symmetric scattering of pions from tritium (^{3}H) and ^{3}He. These experiments have covered incident pion energies from 142 MeV to 295 MeV and scattering angles up to 110° in the laboratory. The results have been used to study charge-symmetry breaking and nuclear scattering systematics.

In the work I have extended these measurements to angles near 180° for pion energies of 142 MeV, 180 MeV, 220 MeV, and 256 MeV, which bracket the Δ_{33} pion-nucleon resonance. This is the most extensive set of πT and π^3He data in this kinematical region. It will allow tests of scattering theory of pion-nucleus interactions and charge-symmetry breaking in back-angle scattering, and, within the limits of these two theories, it may help improve our understanding of the structure of these nuclei.

Chapter 1

Physics

1.1 Introduction

Pion scattering from nuclear targets, which is dominated by the strong force, has been used to study nuclear structure for more than two decades. Recent experiments have shown that information on both nuclear structure and the charge symmetry (CS) of the basic π-nucleon and nucleon-nucleon interactions can be extracted by pion scattering from the isomirror nuclei ^{3}He and Tritium (T) [Nef90], [Pil91]. Complementary structure information can be extracted by electron scattering; however this probe can only measure the neutron distributions by spin-dependent interactions. Since the neutrons in T are paired, their resultant spin is zero, and the neutron radius of T cannot be measured in this way.

In the present experiments, we measure pion-scattering cross sections and cross section ratios at several energies near the Δ_{33} resonance, in the backward hemisphere. There is very little other ^{3}He and T data in this kinematical region, [Alb82], [Kal80].

1.2 The A = 3 System

There are two nuclei with three nucleons, Tritium (T) or ^{3}H, and ^{3}He. T has a single proton and two neutrons. The ground state predominantly has the neutrons paired with opposite spins. ^{3}He is the mirror nucleus of Tritium. It has two mainly spin-paired protons and a single neutron. There are no known excited states of either nucleus [Til87]. Their masses are almost identical; T is $\sim$ 20keV more massive than ^{3}He. The binding energies, however, are substantially different: 8.482 MeV for T, and 7.718 MeV for ^{3}He. This is a difference of 764 keV. Coulomb repulsion accounts for all but 40-80 keV of this [Gib91].

In the absence of the Coulomb interaction, and assuming that the nn and pp interactions are the same, we would expect ^{3}He and T to have exactly the same spatial distributions of nucleons. Since the np force is more attractive than either the nn or pp force (the only bound two-nucleon state is Deuterium (D)), the 'odd' nucleon in each case (the proton in T and the neutron in ^{3}He) will feel more force, and so will have a smaller radius than the 'even' nucleons (the neutrons in T and the protons in ^{3}He); this difference is about 0.15 fm [Gib91]. Adding the Coulomb interaction increases the distance between the protons in ^{3}He. This means that the neutron in ^{3}He feels less force from the more-separated protons. Both the neutron and proton radii in ^{3}He should be expanded in this way, by around 0.02 to 0.04 fm [Gib91]. If the pp and nn nuclear forces are not equal, it is similar to adding an extra piece to the Coulomb interaction, and like effects should be seen.

Following [Gib91], the following definitions will be used: 'delta-even' (δ_e) for the difference between the neutron radius in T and the proton radius in ^{3}He, and 'delta-odd' (δ_o) for the difference between the neutron radius in ^{3}He and the proton radius in T. Because of the overall expansion in ^{3}He mentioned above, we expect δ_e to be negative, and δ_o to be positive.

An extensive review of the experimental and theoretical literature through 1987 is given by Tilley *et. al.* [Til87]. Gibbs and Gibson [Gib91] and the references cited therein give a good background for the topics covered in this work, including the basic scattering theory issues as well as historical perspective.

1.3 The Pion-Nucleon System

The pion is a meson with isospin I=1 , and spin S=0. It comes in three charges, corresponding to the three projections of isospin, I_z, 1, 0, and -1. These projections are called π^+, π^0 and π^-, respectively; they have charges +1, 0, and -1, and masses 139.57, 134.96, and 139.57 MeV/c^2. The nucleon has $S = \frac{1}{2}$ and $S_z = \pm\frac{1}{2}$, $I - \frac{1}{2}$ and $I_z = \pm\frac{1}{2}$. These isospin projections are called the proton (p) and the neutron (n), respectively; they have charges +1 and 0, and masses of 938.27 and 939.57 MeV/c^2.

The possible isospin combinations in π-nucleon scattering are $I = \frac{3}{2}$, $I_z = \pm(\frac{3}{2}, \frac{1}{2})$, and $I = \frac{1}{2}$, $I_z = \pm\frac{1}{2}$. The spin possibilities are $S = \frac{1}{2}$ and $S_z = \pm\frac{1}{2}$. The isospin can be regrouped using Clebsch-Gordan coefficients. If we designate a state with $I = \frac{3}{2}$ and $I_z = \frac{1}{2}$, for example, as $|\,\frac{3}{2}, \frac{1}{2}>$, and use similar notation for the other combinations, then we can rewrite the various scattering combinations as

$$\pi^+ p = |\,\tfrac{3}{2}, \tfrac{3}{2}>, \tag{1.1}$$

$$\pi^+ n = \sqrt{\frac{1}{3}}|\,\tfrac{3}{2}, \tfrac{1}{2}> + \sqrt{\frac{2}{3}}|\,\tfrac{1}{2}, \tfrac{1}{2}>, \tag{1.2}$$

$$\pi^0 p = \sqrt{\frac{2}{3}}|\,\tfrac{3}{2}, \tfrac{1}{2}> - \sqrt{\frac{1}{3}}|\,\tfrac{1}{2}, \tfrac{1}{2}>, \tag{1.3}$$

$$\pi^0 n = \sqrt{\frac{2}{3}}|\,\tfrac{3}{2}, -\tfrac{1}{2}> + \sqrt{\frac{1}{3}}|\,\tfrac{1}{2}, -\tfrac{1}{2}>, \tag{1.4}$$

$$\pi^- p = \sqrt{\frac{1}{3}} | \tfrac{3}{2}, -\tfrac{1}{2} > - \sqrt{\frac{2}{3}} | \tfrac{1}{2}, -\tfrac{1}{2} >, \tag{1.5}$$

$$\pi^- n = | \tfrac{3}{2}, -\tfrac{3}{2} >. \tag{1.6}$$

There is an experimentally observed resonance in π-nucleon scattering for incoming pions with energy of $\sim$ 180 MeV with the nucleon at rest. This resonance, called the 'Delta Resonance' (Δ_{33}), occurs when the spatial-angular momentum quantum number ℓ is 1, the total angular momentum quantum number J is $\frac{3}{2}$, and the total isospin I is $\frac{3}{2}$.

Consider elastic π^+ n scattering at 180 MeV. The scattering amplitude will contain a term that looks like

$$< \pi^+ n |M| \pi^+ n >, \tag{1.7}$$

which can be rewritten as

$$\left(\sqrt{\frac{1}{3}} < \tfrac{3}{2}, \tfrac{1}{2} | + \sqrt{\frac{2}{3}} < \tfrac{1}{2}, \tfrac{1}{2} | \right) (M) \left(\sqrt{\frac{1}{3}} | \tfrac{3}{2}, \tfrac{1}{2} > + \sqrt{\frac{2}{3}} | \tfrac{1}{2}, \tfrac{1}{2} > \right),$$

where M is the transition operator. The amplitude does not depend on the I_z value if we assume that CS holds for π-nucleon interactions. Assuming the conservation of I in the π-nucleon interactions, and that the transition does not depend on I_z, so the I_z component can be suppressed, we can rewrite this as

$$\frac{1}{3} < \tfrac{3}{2} |M| \tfrac{3}{2} > + \frac{2}{3} < \tfrac{1}{2} |M| \tfrac{1}{2} > \equiv \frac{1}{3} M_3 + \frac{2}{3} M_1.$$

On resonance, that is, where the incoming pion kinetic energy is 180 MeV, and $M_3 \gg M_1$, this is just $\frac{1}{3} M_3$.

With these assumptions, after forming matrix elements like Eq. 1.7 for $\pi^+ p$, $\pi^- p$, *etc.*, we can write down the following relationships for the scattering cross sections, either total or differential, which are proportional to the square of the amplitudes:

$$\begin{aligned} \sigma(\pi^+ p) &= 9\sigma(\pi^+ n), \\ \sigma(\pi^- n) &= 9\sigma(\pi^- p), \\ \sigma(\pi^+ p) &= \sigma(\pi^- n), \\ \sigma(\pi^+ n) &= \sigma(\pi^- p). \end{aligned}$$

If we assume that a system that has total spin = $\frac{1}{2}$ is invariant under rotations and parity reversals, then it can be shown [Tay72, Chap. 6] that the scattering amplitude can be written as

$$A(\theta, E) = f(\theta, E) + ig(\theta, E) \hat{\mathbf{n}} \cdot \sigma$$

where f and g are called the *non-spin-flip* and ***spin-flip*** amplitudes, respectively. They are the amplitudes for scattering where the third component of the spin of the nucleon is 'flipped' (has its sign changed) or not 'flipped' during the interaction. θ is the scattering angle, E is the total energy, $\hat{\mathbf{n}}$ is a unit vector perpendicular to the scattering plane, and σ is the Pauli representation of the spin, that is, $\mathbf{S} = \frac{1}{2}\sigma$. The differential cross section is the magnitude of this amplitude,

$$\frac{d\sigma}{d\Omega} = \mid f \mid^2 + \mid g \mid^2, \tag{1.8}$$

in the case where the target is not polarized and the scattering asymmetry is not measured. Near the Δ_{33}-resonance energy, the interaction is dominated by the $\ell = 1$ partial wave; the spin-flip amplitude has a sine dependence and the non-spin-flip amplitude has a cosine dependence.

Figure 1.1 shows the basic amplitudes for $\pi^{\pm}$ p, at the pion-resonance energy of 180 MeV, from the VPI phase-shift analysis [Arn85]. Except at far-forward angles, most of the amplitude is in the imaginary parts. The sine and cosine shapes of the spin-flip and non-spin-flip parts are obvious. The $\pi^- p$ amplitudes are $\sim \frac{1}{3}$ of the $\pi^+ p$, as predicted. There will be a dip at 90°, the 'non-spin-flip dip' (NSF dip), in any amplitudes that depend primarily on the non-spin-flip part, because of the cosine dependence.

1.4 Charge Symmetry

Charge Symmetry (CS) is defined as equality under the operation of charge conjugation. In the case of πT and π^3He scattering, charge conjugation changes π^+ into $\pi^-$and *vice versa*, and also changes T and ^{3}He into each other (by reversing the protons and the neutrons). Therefore, if charge symmetry were universal, we would expect π^+T to be the same as π^{-3}He, and π^-T to be the same as π^{+3}He. CS can be broken in four ways in this system. The first charge-symmetry breaking (CSB) effect is Coulomb scattering. The Coulomb force is not charge symmetric; thus the different charge combinations of pions and nucleons are important. In general, Coulomb scattering is of the order $1/137^2$ less than the strong force scattering, so this should be a small effect. However, in the region of the NSF dip, some of the primary amplitudes are going through zero (see Fig. 1.1). We might expect that Coulomb interference could be important there.

The second CSB effect is also due to the Coulomb force. Coulomb repulsion pushes the protons in ^{3}He apart, forcing the neutron radius in ^{3}He to increase as well. Because of this ^{3}He is larger than T, and so the form factor of ^{3}He will fall off more quickly with momentum transfer than will that of T(see Sec. 1.6.2). In general, the ^{3}He cross sections will be less than the T cross sections in nominally charge-symmetric situations. For instance, because of this size difference, we expect

$$\sigma(\pi^+\mathrm{T}) > \sigma(\pi^{-3}\mathrm{He}).$$

The third CSB effect is due to any difference in the nn force with respect to the pp force. For example, if the pp force is greater than the nn force after

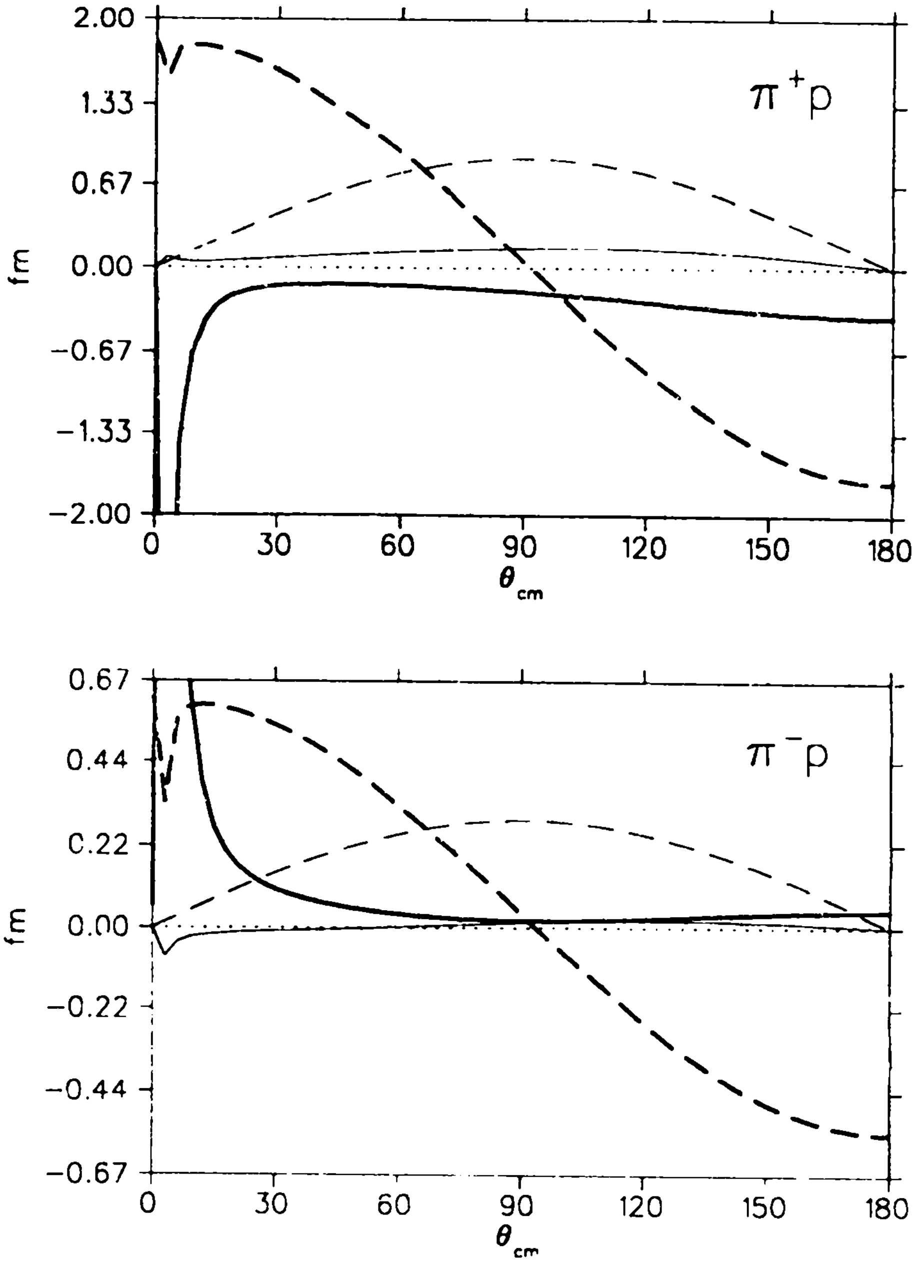

Figure 1.1: π-nucleon scattering amplitudes, for 180 MeV pions and stationary nucleons (in the lab frame), as a function of scattering angle in the π-nucleon center of mass, from the VPI phase shift analysis [Arn85]. The bold lines are the non-spin-flip amplitudes, the lighter lines are spin-flip amplitudes. The real parts of the amplitudes are shown solid, the imaginary parts dashed. The dotted lines show zero amplitude, for reference.

the electromagnetic interaction has been accounted for, then the proton radius will be increased in ^{3}He over the neutron radius in T, beyond the increase due to Coulomb repulsion. This is an example of Nuclear-Charge-Symmetry Breaking (NCSB).

The final CSB effect is a difference in the strong πN amplitudes as a function of isospin projection. A good measure of this is given by pion scattering from Deuterium. Recent measurements by Smith *et. al.* [Smi88] found an overall asymmetry of $\sim -1.5\%$ for π^+D and π^-D scattering at the resonance energy in the backward hemisphere, independent of scattering angle. Neglecting Coulomb effects, this scattering should be charge symmetric; if the reported asymmetry is correct, we can expect it to show up in the current results as well.

1.5 Ratios

Several scattering ratios have been defined by Nefkens *et. al.* [Nef90] that help to illuminate different parts of the pion interactions with $A = 3$ targets, and which also give some evidence for NCSB [Nef90]. They are:

$$\begin{aligned}
\rho^+ &= d\sigma(\pi^+\mathrm{T})/d\sigma(\pi^{+3}\mathrm{He})\ , \\
\rho^- &= d\sigma(\pi^-\mathrm{T})/d\sigma(\pi^{-3}\mathrm{He})\ , \\
r_1 &= d\sigma(\pi^+\mathrm{T})/d\sigma(\pi^{-3}\mathrm{He})\ , \\
r_2 &= d\sigma(\pi^-\mathrm{T})/d\sigma(\pi^{+3}\mathrm{He})\ , and \\
R &= r_1 \times r_2 \ = \rho^+ \ \times \rho^- \ .
\end{aligned}$$

A brief discussion of each ratio is given below.

ρ^+ ... π^+T is in the numerator. At the resonance energy, scattering from the proton will dominate; both spin-flip and non-spin-flip scattering are possible. The denominator, π^{+3}He, is dominated by π^+ on the spin-paired protons, and so predominantly non-spin-flip scattering. Near the NSF dip, at 78° in the π-nucleus center of mass (90° in the π-nucleon center of mass), the non-spin-flip amplitude goes through zero, so most of the scattering is spin-flip. The denominator reflects this dip, since it is primarily NSF, but the numerator can still experience spin-flip on the single proton. Therefore, there is a peak in ρ^+ around 78°. As the scattering angle approaches back angles, the spin-flip amplitude goes to zero, and the non-spin-flip amplitude dominates for single scattering. This means that the denominator, which has twice as many protons as the numerator, is larger, and ρ^+ should decrease at large angles, in a single-scattering picture.

ρ^- ... The systematics are the inverse of those for ρ^+ . Because $\pi^- n$ is predominant, there is a dip in the NSF dip region where ρ^+ has a bump, and the ratio should rise at back angles for single scattering, because the two resonance interactions in the numerator will dominate the single resonance interaction in the denominator as the spin-flip term goes to zero.

r_1 ... The numerator, $\pi^+ {}^3$He , and the denominator, π^-T , are isomirror interactions. Therefore, if CS were strictly observed, r_1 would equal 1.0.

The Coulomb interaction is not charge symmetric. There is twice as much Coulomb scattering in the denominator as in the numerator, because there are twice as many charged nucleons in ^{3}He as there are in T, and so both the pure Coulomb scattering and the Coulomb interference is not the same for numerator and denominator, (see Sec. 1.6.1). Furthermore, the protons in ^{3}He will feel a mutual repulsion, so they will be farther apart than the neutrons in T. This repulsion is reflected in an increased separation, and therefore a decreased form factor, decreasing the cross section in the denominator. Finally, the effect of the Coulomb-nuclear interference depends on the relative phase of the nuclear and Coulomb amplitudes.

The Coulomb-scattering effects are small, so we expect that the the difference in form factors to dominate and r_1 should be greater than 1.0. Generally, r_1 emphasizes scattering from the *unpaired* nucleons, p in T and n in ^{3}He, at the resonance energy.

r_2 ... This ratio is also nominally charge symmetric, and the decrease of the form factor of ^{3}He in the numerator should cause r_2 to be greater than 1.0, as was the case for r_1 . Since r_2 emphasizes the paired nucleons at the resonance energy, it will be primarily non-spin-flip scattering. At the NSF dip, since only spin-flip is left, it will be a ratio of the 'non-resonance interactions', that is $\pi^- p / \pi^+ n$.

R... The Superratio can be formed as the product or r_1 and r_2 , and equivalently of ρ^+ and ρ^- . It will have the same first-order corrections for Coulomb effects in both the numerator and the denominator, so it is less sensitive to Coulomb than the other ratios. If CS is universally true, R is 1.0.

These ratios have been measured in three previous experiments, for a variety of energies in the forward hemisphere [Nef90] [Pil91] [Pil92] [Ber91]; the results are shown in the following figures.

The bump at 78° that corresponds to the NSF dip is obvious in ρ^+ , ρ^- , r_2 and R, for 142 MeV and 180 MeV incident pions. The larger error bars on r_1 and r_2 are due to the fact that the normalizations do not cancel there (see Chapter 3).

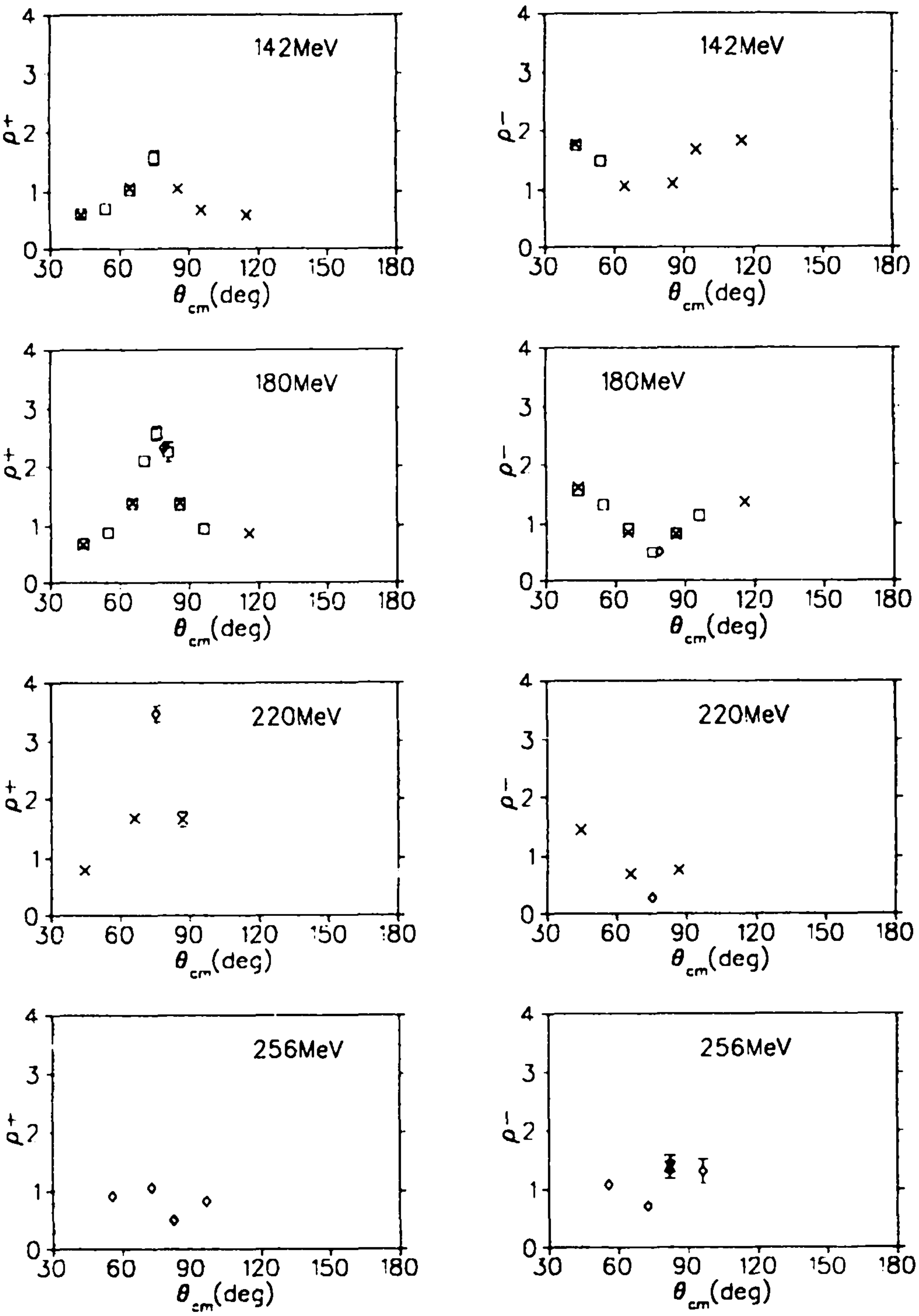

Figure 1.2: ρ^+ and ρ^- from previous LAMPF experiments. □ Exp. 546 [Nef90], × Exp. 905 [Pil91], ◇ Exp. 1032 [Pil92] and [Ber91]. The structure at ~ 78° corresponds to the NSF flip.

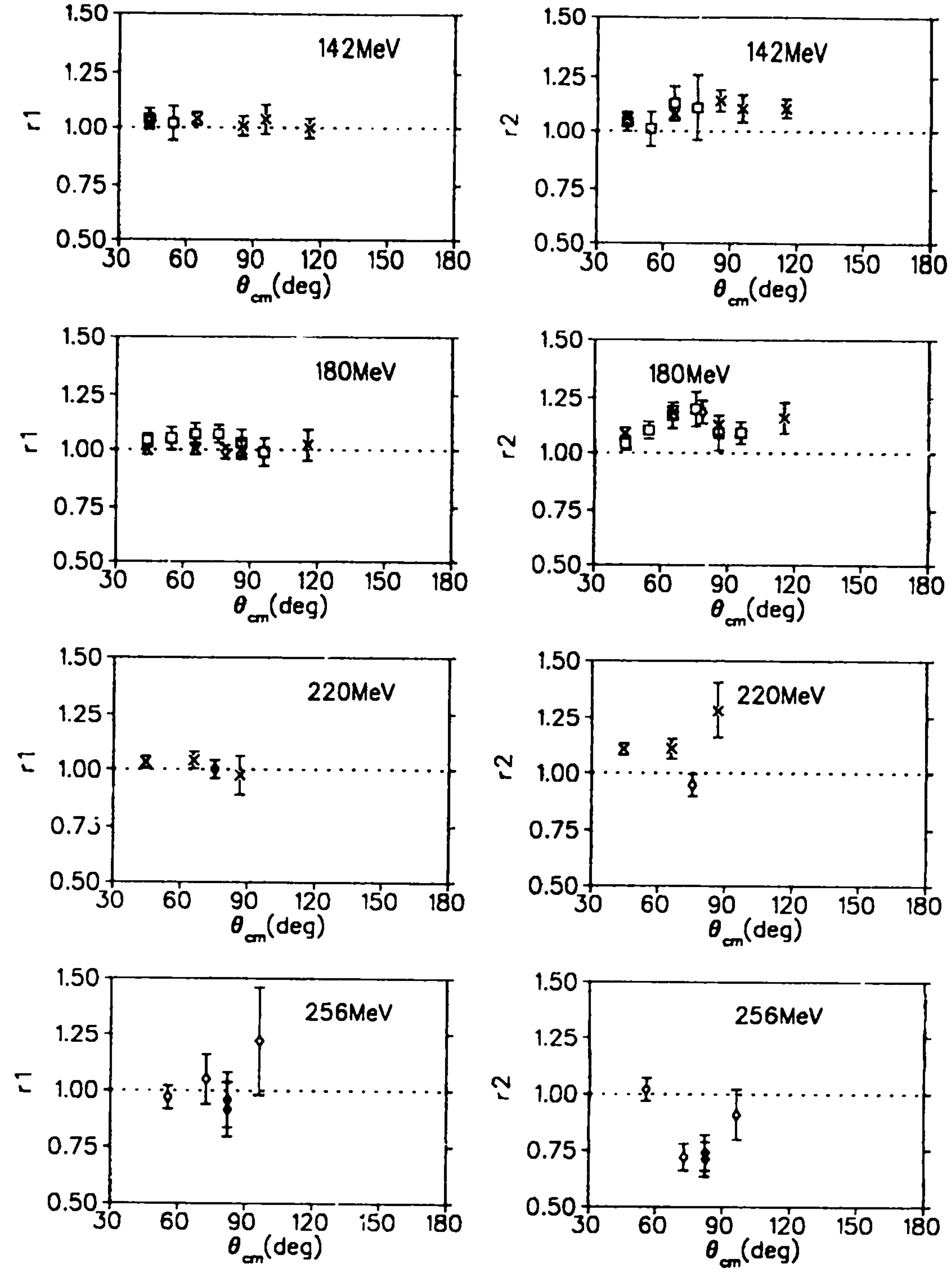

Figure 1.3: r_1 and r_2 from previous LAMPF experiments. □ Exp. 546 [Nef90], × Exp. 905 [Pil91], ◇ Exp. 1032 [Pil92] and [Ber91].

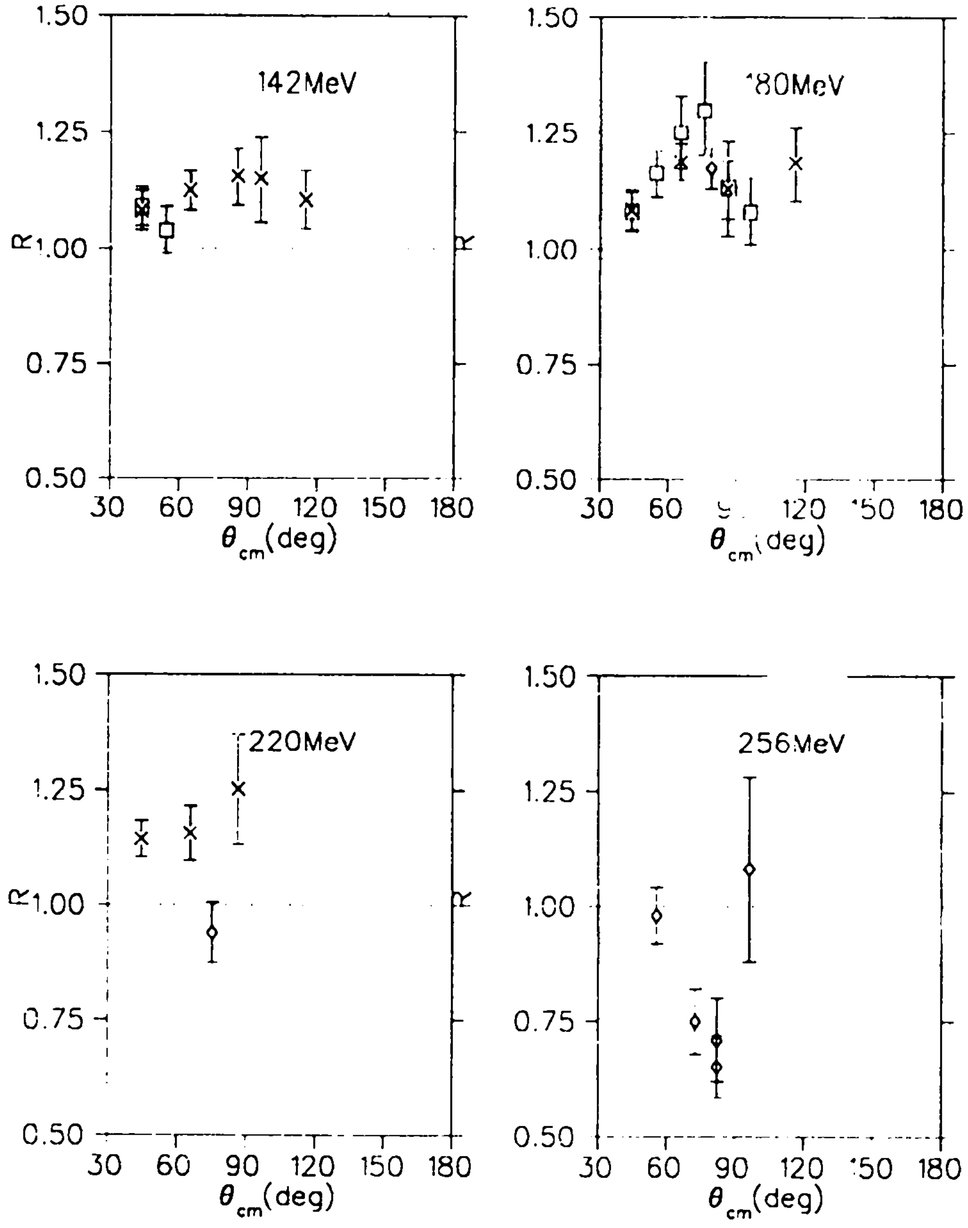

Figure 1.4: R from previous LAMPF experiments. □ Exp. 546 [Nef90], × Exp. 905 [Pil91], ◇ Exp. 1032 [Pil92] and [Ber91].

1.6 Elastic Scattering

Elastic scattering is a scattering reaction that leaves both participants in the same states they occupied before the collision. Although intermediate states that are not the same as the final states can be included in a multiple-scattering calculation, very often it is assumed that both participants remain in their original states throughout the entire process. In single scattering, this is the only possibility. Since there is no rearrangement, this is a good way to study some aspects of nuclear structure. π-nucleus scattering is a combination of two interactions. Because both the pions and the nucleons have charge, there is the Coulomb force. The pions and the nucleons also interact through the strong force, and the proper description of the interaction includes both forces.

1.6.1 Coulomb Scattering

Coulomb scattering is a small part of the interaction because of the coupling constant $\alpha = \frac{1}{137}$, compared to ~ 1.0 for the strong force. The Rutherford formula for Coulomb scattering is

$$d\sigma/d\Omega = \frac{z^2\mu^2}{4p^2\sin^4(\theta/2)}$$

where z is the charge of the nucleus , μ is the reduced mass, p is the center-of-mass momentum and θ is the scattering angle. The fourth power of the sine in the denominator means that the cross section is very large at small angles, and drops off rapidly as the angle increases. In a potential-interaction description of π-nucleus scattering, the Coulomb interaction can be included as a separate term in the scattering amplitude.

$$f = f_C + f_N e^{-i2\phi}$$

where f_N refers to the strong-force amplitude, and 2ϕ describes the phase between the two [Tay72] [Bin78].

Since the cross section is the square of the amplitude, we can write

$$\frac{d\sigma}{d\Omega} = |f_N|^2\left[1 + \frac{|f_C|^2}{|f_N|^2} + 2\frac{|f_C|}{|f_N|}\frac{Re\ f_N}{|f_N|}\left(\cos(2\phi) + \frac{Im\ f_N}{Re\ f_N}\sin(2\phi)\right)\right].$$

The last two terms in the square brackets are the fractional change due to the Coulomb interaction. Especially at back angles, the Coulomb contribution should be small, because of the factors of f_C/f_N. However, in regions where the strong amplitudes are small, such as at the NSF dip, the Coulomb force may become important. Whether it can be neglected must be investigated in each case.

1.6.2 Nuclear Scattering

Many scattering quantities are reported in terms of the four momentum transfer

$$q \equiv (E_f, \mathbf{p}_f) - (E_i, \mathbf{p}_i),$$

where the subscripts refer to the final and initial quantities, that is, for the outgoing and incoming pion. For elastic scattering, the energy is conserved, and

$$q^2 = q^\mu q_\mu = -\mathbf{q} \cdot \mathbf{q}. \equiv t$$

The units used throughout are inverse-fermis squared (fm^{-2}).

An interaction is limited kinematically by the amount of momentum that can be transferred from the projectile to the target. In elastic scattering, we consider the nucleus as a single particle. Momentum and energy must be conserved with this particle and the projectile in any scattering interaction, so for scattering at a given angle the momentum transfer is found from π-nucleus kinematics. However, if we assume that the scattering involved just a single interaction of a pion with one nucleon (single scattering), then the total momentum transfer must come from that interaction. Figure 1.5 and Figure 1.6 show calculations of the momentum transfer for scattering from tritons and nucleons. Four curves are calculated for each energy that is covered by these experiments. The solid curve is for scattering from the Triton. The dashed curve is scattering from an at-rest nucleon. The two dotted curves are for scattering from nucleons with non-zero nuclear momenta. In each plot, the upper dotted curve is for nucleons with nuclear momentum of 200 MeV/c, and the lower dotted curve is for nuclear momentum of 100 MeV/c. For every energy except 295 MeV, it is possible to get the required momentum transfer for scattering out to 180° from single scattering, although for the largest angles, only the tail of the nuclear-momentum distribution will suffice. This means that the probability for single scattering decreases as a function of the momentum transfer. The curves show that single-scattering is important throughout the entire angular range at 142 MeV, and that its importance decreases as the incident energy increases. At 295 MeV, it will be impossible at the largest angles for all but the highest-momentum nucleons. We should be able to have a very large component of single scattering at least to the angle of the NSF dip, since at that point for 180 MeV pions there is good overlap between the π-nucleus momentum transfer and the momentum transfer from 100 MeV/c nucleons, as shown in Fig. 1.5.

1.6.3 Pion-Nucleus Scattering

For a π-nucleus interaction described by a Hamiltonian

$$\begin{aligned} H &= H_0 + V \\ &= H_N + K_\pi + \sum_{i=1}^{A} v_i(\mathbf{r} - \mathbf{r_i}), \end{aligned}$$

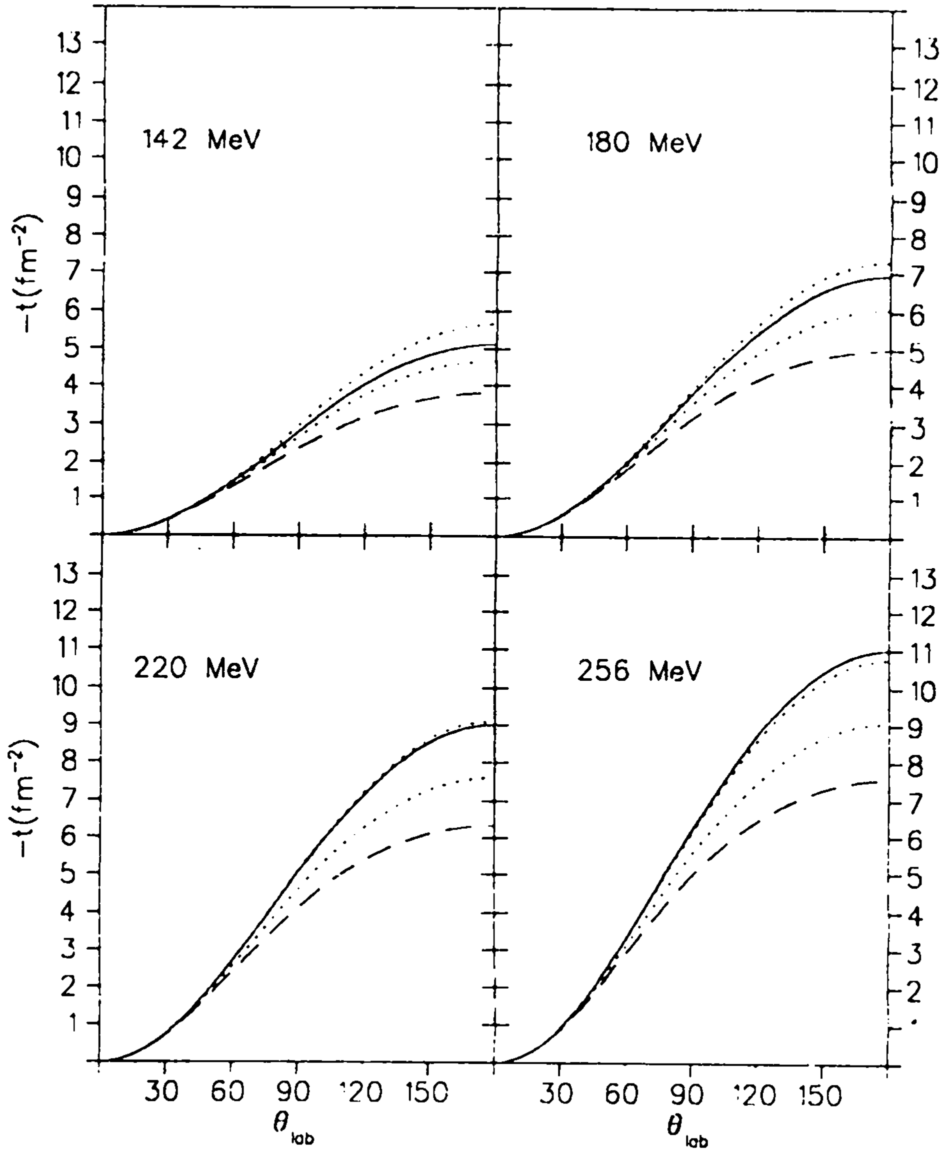

Figure 1.5: Momentum transfer as a function of center-of-mass scattering angle for the π-nucleon and the π-nucleus systems, for four incident-pion energies. In each figure, the solid line is momentum transfer to the nucleus, and the dashed line is momentum transfer from a free nucleon at the same incident pion energy and laboratory scattering angle. The dotted lines are the maximum possible momentum transfer from moving nucleons; with nucleon momentum of 200 MeV/c for the top line in each case, and 100 MeV/c for the bottom dotted line.

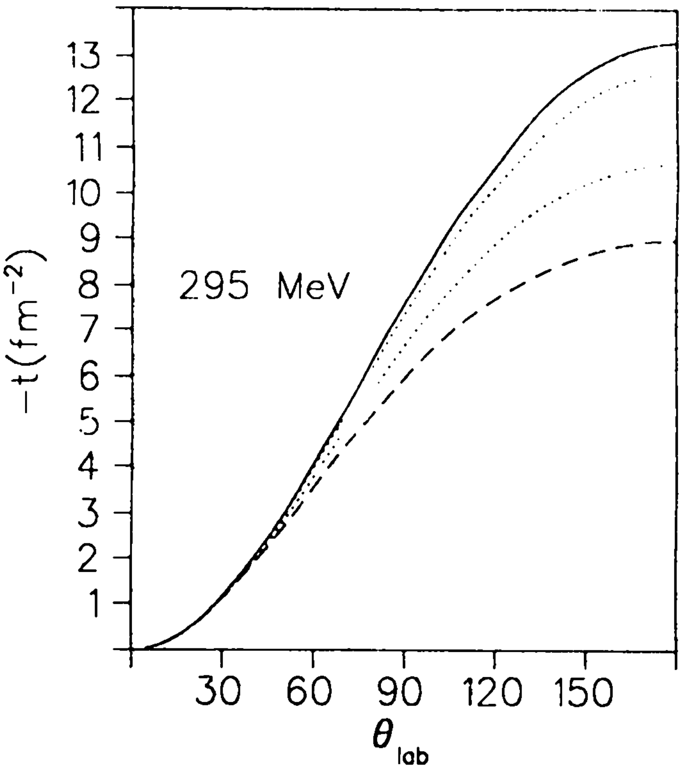

Figure 1.6: Momentum transfer as a function of center-of-mass scattering angle for the π-nucleon and the π-nucleus systems, for an incident-pion energy of 295 MeV. The different lines are described in Fig. 1.5.

where H_N is the nuclear Hamiltonian, A is the number of nucleons in the nucleus, K_π is the pion kinetic energy, and v_i is the interaction between the pion at coordinate $\mathbf{r}$, and the nucleon at $\mathbf{r_i}$, we can write an equation for the T matrix

$$T \;=\; V + VGT = \sum_{i=1}^{A} v_i + \sum_{i=1}^{A} v_i G T.$$

This background material is from [Eis80, Chap. 3,4]. The scattering amplitude is

$$< \mathbf{k'}\ \mathbf{p'}\ \alpha'\ |T|\ \mathbf{k}\ \mathbf{p}\ \alpha >, \tag{1.9}$$

where $\mathbf{k'}, \mathbf{k}$ and $\mathbf{p'}, \mathbf{p}$ are the final and initial momenta of the pion and nucleus, respectively, and α', α refer to the final and initial total spin and isospin. G is the Green function or propagator for the pion in the nuclear medium

$$G = \frac{1}{E - H_N - K_\pi + i\eta},$$

where E is the total energy and η is taken to zero after the integral to determine the amplitude is completed. After some algebra, we can write

$$T_i \;\equiv\; t_i + t_i G \sum_{j \neq i}^{A} T_j, \tag{1.10}$$

$$T \;=\; \sum_{i=1}^{A} T_i, \tag{1.11}$$

$$t_i \;=\; v_i + v_i G t_i. \tag{1.12}$$

t_i is the amplitude for scattering from a single nucleon in the nuclear medium. In the case where the nuclear Hamiltonian can be neglected with respect to the pion kinetic energy,

$$t_i \sim t_i^{free}, \tag{1.13}$$

is the amplitude for scattering from a free nucleon. Note that $t_i = t_i(E)$, where E is the total interaction energy, found in the propagator.

In elastic scattering, the initial and final nuclear states will be the ground state. We expect the first part of the expansion for T_i to be greater than the terms in the summation $t_i G \sum_{j \neq i}^{A} T_j$ because the latter contains products of amplitudes. Retaining only the initial term, 1.9 can be rewritten as

$$\sum_{i=1}^{A} < 0\ |< \mathbf{k'}\ \mathbf{p'_i}\ \alpha'\ |t_i|\ \mathbf{k}\ \mathbf{p_i}\ \alpha >|\ 0 >$$

$$= \sum_{i=1}^{A} \int d\mathbf{p_1} \ldots d\mathbf{p_i}, d\mathbf{p'_i} \ldots d\mathbf{p_A}$$

$$\times \Phi_0^{\dagger}(\mathbf{p_1} \ldots \mathbf{p'_i} \ldots \mathbf{p_A}) t_i^{\alpha}(\mathbf{k'}, \mathbf{k}, \mathbf{p}, E) \delta(\mathbf{p'_i} + \mathbf{k'} - \mathbf{p} - \mathbf{k}) \Phi_0(\mathbf{p_1} \ldots \mathbf{p'_i} \ldots \mathbf{p_A}).$$

The matrix $< \mathbf{k}'\, \mathbf{p}_i'\, \alpha'\, |t_i|\, \mathbf{k}\, \mathbf{p}_i\, \alpha >$ has been replaced by a number that depends on the interaction energy and a delta function that conserves momentum among the pion and struck nucleon. Φ_0 refers to the nuclear ground state. The delta function serves to replace $\mathbf{p}_i'$ with $\mathbf{p}_i - (\mathbf{k}' - \mathbf{k}) \equiv \mathbf{p}_i - \mathbf{q}$.

If we ignore the motion of the struck nucleon, that is take $\mathbf{p}_i = \mathbf{p}_i' = 0$ when considering the amplitude t_i, we have the fixed-scatterer approximation. The amplitude becomes

$$\sum_{\alpha,i} t_{\alpha,i}(\mathbf{k}'\,\mathbf{k}\,E) \int d\mathbf{p}_1 \ldots d\mathbf{p}_A \Phi_0^{\alpha\dagger}(\mathbf{p}_1 \ldots \mathbf{p}_i - \mathbf{q} \ldots \mathbf{p}_A)\Phi_0^{\alpha}(\mathbf{p}_1 \ldots \mathbf{p}_i \ldots \mathbf{p}_A).$$

The ground states have been replaced by functions that refer to the proton and neutron ground states, taken separately. α refers to the nucleon type, and i is an index within this type, such as the first neutron, the second neutron, *etc.* . This removes direct isospin dependence in favor of describing the neutrons and protons individually. We can rewrite the integral as

$$F_\alpha(\mathbf{q}) \equiv \int d\mathbf{r} e^{i\mathbf{q}\cdot\mathbf{r}} \rho^\alpha(\mathbf{r}), \tag{1.14}$$

and the amplitude becomes

$$\sum_{i,\alpha} t_{i,\alpha}(\mathbf{q}, E) F_\alpha(\mathbf{q}). \tag{1.15}$$

The form factor is the Fourier transform of the nuclear density. the ratio between scattering from an extended object. and scattering from a point. The electromagnetic form factors for T are reported in [Jus85],[Bec82] and [Col65], and for ^{3}He in [McC77], as well as others. The charge form factor measured this way. F_{ch}. reflects the spatial distribution of protons in the nuclei, that is it is similar to the body form factor.

The form factors are given as functions of the 4-momentum transfer, squared. q^2. Figure 1.7 shows the ^{3}He charge form factor measured by [McC77]. If we assume a gaussian shape for the nuclear density, then

$$F_{ch} = e^{-q^2 R^2/6} \tag{1.16}$$

where R is the nuclear radius. As the figure shows, an effective radius, $R_{eff} =$ 1.73 fm. gives a good match to the data in the region of the current experiments, up to about $-t \equiv q^2 = 8\text{fm}^{-2}$. $R_{eff} = 1.60$ fm does a similarly good job for the T data. which is not shown.

1.6.4 A Simple Calculation

With the approximation in 1.13, we can use the π-nucleon amplitudes shown in Fig. 1.1 in Eq. 1.15 to get the scattering amplitudes. However, α refers to the proton and neutron, so we need an expression for the neutron form

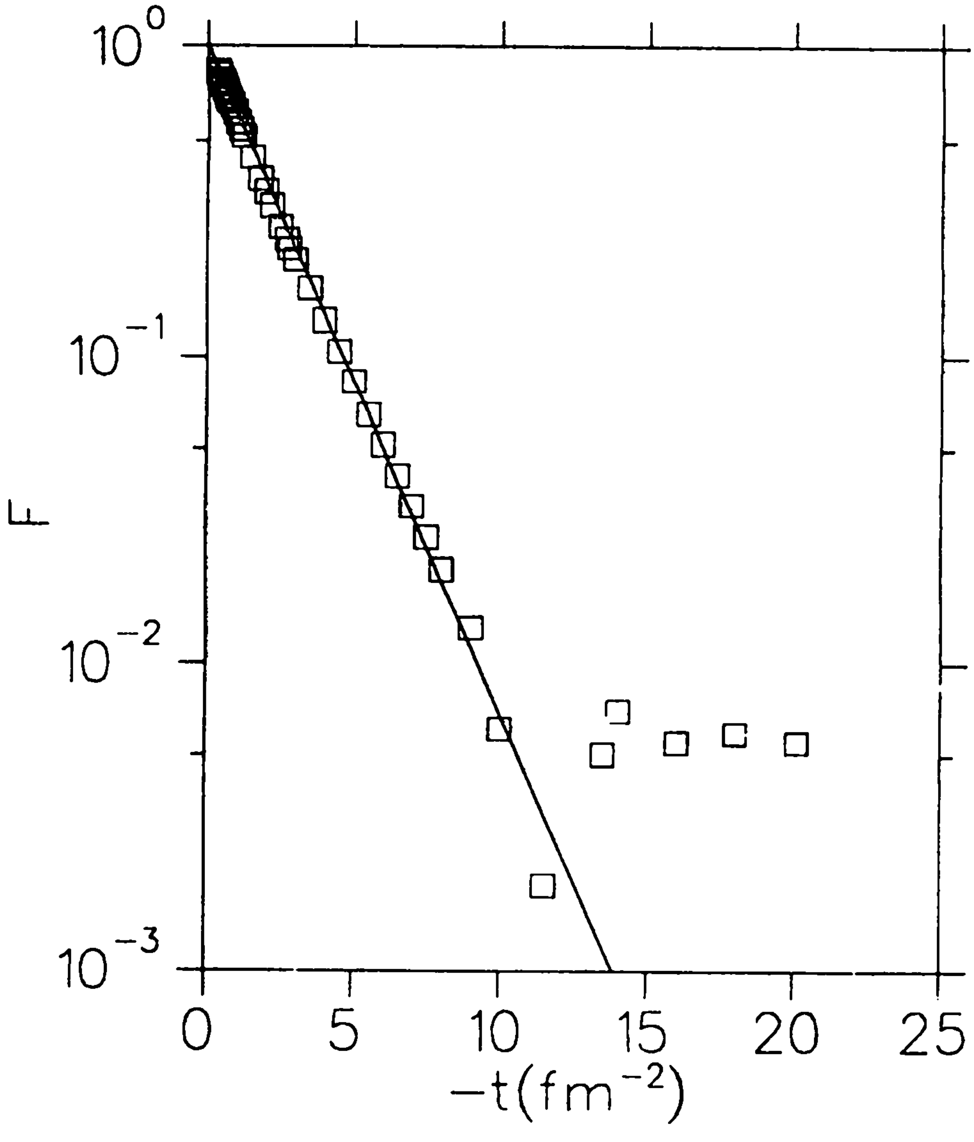

Figure 1.7: Form factors for e^3He scattering, and a gaussian form factor calculated with R = 1.73 fm.

factor. We expect the neutrons and protons to have similar distributions. In particular, under charge symmetry, the neutron in ^{3}He should have exactly the same distribution as the proton in T; likewise, the protons in ^{3}He and the neutrons in T.

Gibbs and Gibson, see Sec. 1.7, suggest that proton repulsion in ^{3}He leads to an increase in the proton radius of ^{3}He over the neutron radius of T of 0.030 fm while the neutron radius of ^{3}He is greater than the proton radius of T by 0.035 fm. In a gaussian form factor such as in Eq. 1.16 we can just change the value of R_{eff} to accommodate these radius differences. In the following calculation, the charge form factors measured in electron scattering are used at each value of q^2 for pion scattering from the protons. Expanding R_{eff}^2

$$R_{eff}^2 = (R_p + \delta)^2 = R_p^2 + 2R_p\delta + \cdots,$$

where R_p is the proton-distribution radius and δ is the small change to get the neutron-distribution radius. Then, we can multiply the measured proton form factors by $e^{-2q^2R_p\delta/6}$ to get the neutron form factors. In doing this we assume the neutron distribution has the same basic shape as that of the protons, but that the neutron distributions' radius is different.

In π-nucleus elastic scattering, we cannot have spin-flip scattering from the spin-paired nucleons, protons in ^{3}He and neutrons in T, because the Pauli principle forbids them to have the same spin in the ground state, and there are no excited states to occupy. We can write out the amplitude for the fixed-scatterer approximation using the free nucleon amplitudes as

$$\begin{aligned}
A(\pi^+\mathrm{T}) &= F_{pT}\,[f(\pi^+p\,) + g(\pi^+p\,)] + 2F_{nT}\,f(\pi^+n\,),\\
A(\pi^{+3}\mathrm{He}) &= 2F_{p^3He}\,f(\pi^+p\,) + F_{n^3He}\,[f(\pi^+n\,) + g(\pi^+n\,)],\\
A(\pi^-\mathrm{T}) &= F_{pT}\,[f(\pi^-p\,) + g(\pi^-p\,)] + 2F_{nT}\,f(\pi^-n\,),\\
A(\pi^{-3}\mathrm{He}) &= 2F_{p^3He}\,f(\pi^-p\,) + F_{n^3He}\,[f(\pi^-n\,) + g(\pi^-n\,)],
\end{aligned}$$

where the form factors are written as, for example, F_{pT}, 'the form factor for protons in T'.

Fig. 1.8 is an example of this calculation, which will be called the Simple Model henceforth, for 180 MeV pions. The match is good up until the vicinity of the NSF dip. From the momentum transfer calculations, we would only expect the fixed-scatterer, that is zero-momentum nucleon, approximation to be good to 60° — 70° in the center of mass, and the dip occurs at about 78°.

Fig. 1.9 shows the same calculation, this time for the ratios ρ^+, ρ^-, r_1 and r_2. The effect of the dip is very prominent for ρ^+ and ρ^-. For example in ρ^+, the numerator is π^+T, at resonance energies this is primarily π^+p, on the *unpaired* nucleon, so spin-flip can occur. In the denominator, the resonance scattering is from *paired* protons, which can not undergo spin-flip scattering. So, as the angle approaches the value for the NSF dip, the denominator goes as the disappearing non-spin-flip amplitude, while the numerator goes with the

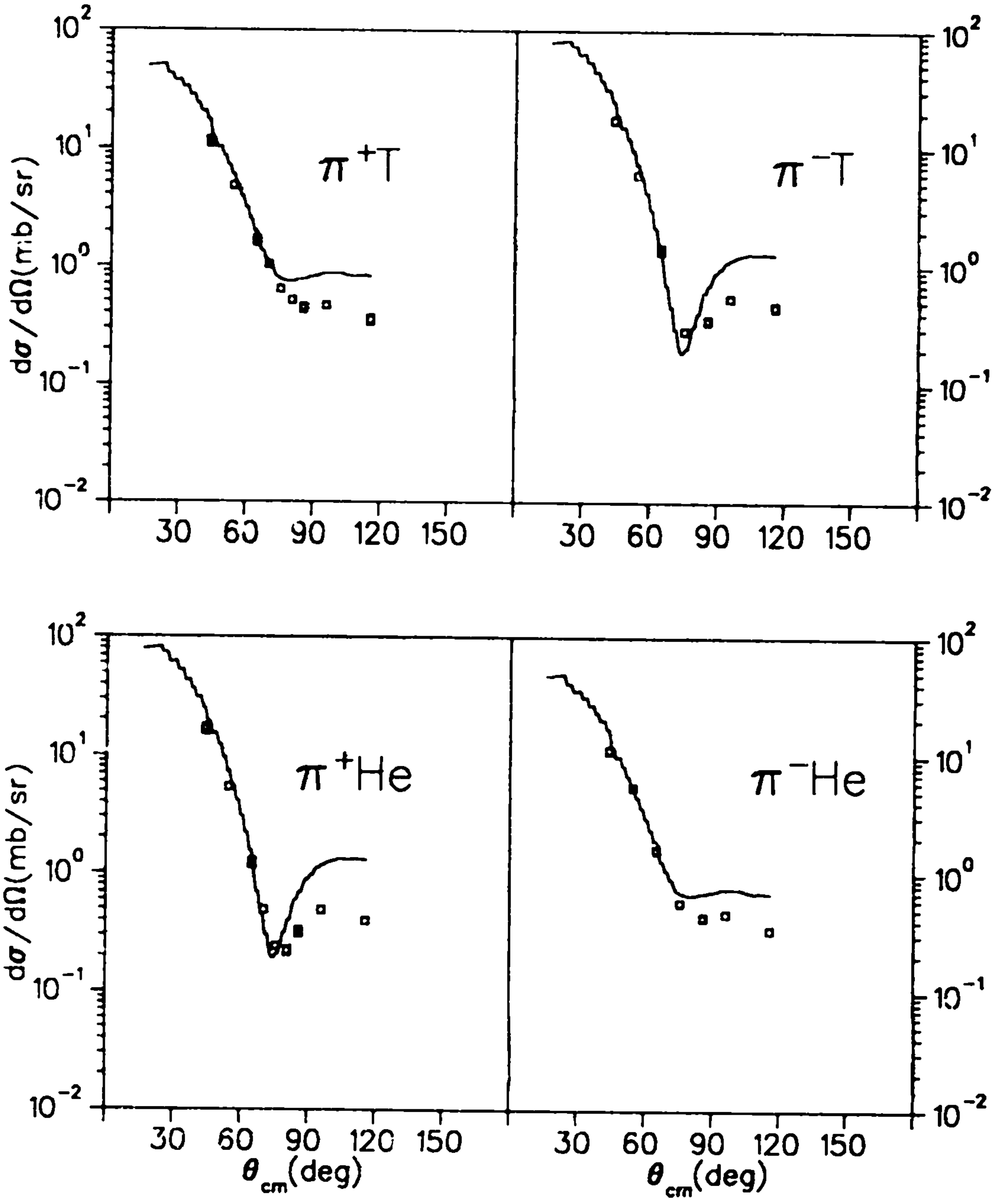

Figure 1.8: A fixed-scatterer impulse calculation of the 180 MeV cross sections from previous experiments [Nef90] [Pil91].

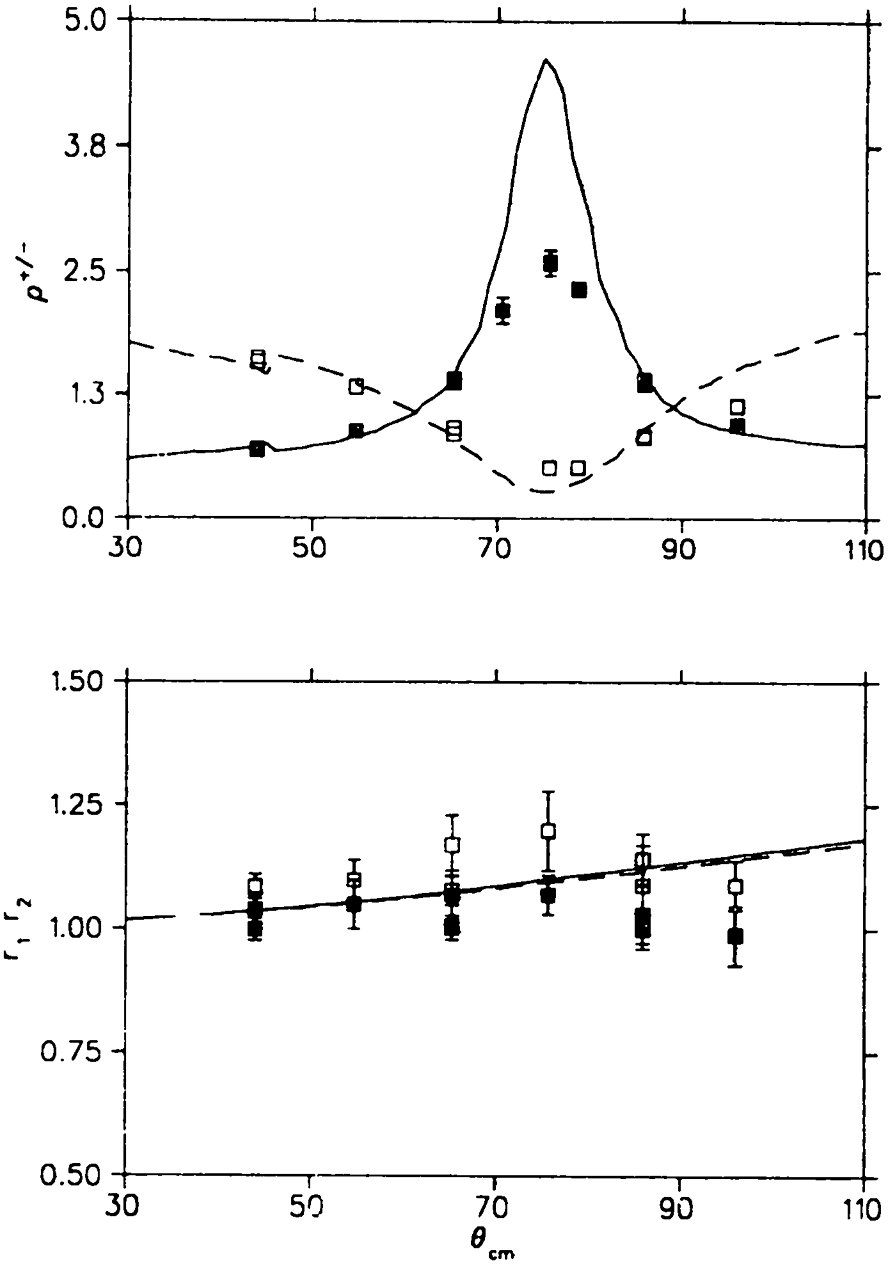

Figure 1.9: A fixed-scatterer impulse calculation of the 180 MeV ratios. *Top:* ρ^+, filled squares, and ρ^-, open squares. *Bottom:* The charge symmetric ratios r_1, filled squares, and r_2, open squares. Data from previous experiments [Nef90],[Pil91],[Pil92] and [Ber91].

peaking spin-flip amplitude, and ρ^+ has a bump. The systematics are exactly the same for ρ^-, except that it is the numerator that goes as the non-spin-flip, and the denominator goes as the spin-flip amplitude, so ρ^- has a dip. The calculated values of ρ^+ and ρ^- match the data well. The size of the effect is somewhat too large at the depth of the dip, and the match is not good at large angles. This latter is expected since we are getting far out in momentum transfer, where the zero-momentum amplitudes (fixed-scatterer approximation) are less and less appropriate, because the kinematics require that scattering takes place from nucleons with higher momenta.

The match of the calculations with r_1 and r_2 is poor. At resonance energies, in the region of the NSF dip, r_1 is primarily

$$\frac{F_{pT}\ g(\pi^+ p)}{F_{n^3He}\ g(\pi^- n)};$$

the amplitudes should be nearly equal (in these calculations they are set equal, as the VPI program only calculates pion-proton scattering), and we may expect the form factor ratio to govern the shape here. The extrapolation to the neutron form factors is very crude; the subtlety of the effect is certainly beyond the calculation. The overall flatness of the curve is expected, but the steady rise is not seen in the data. At this energy and angle, r_2 is primarily

$$\frac{F_{pT}\ g(\pi^- p)}{F_{n^3He}\ g(\pi^+ n)};$$

neither numerator nor denominator are purely $I_z = \frac{3}{2}$. The bump in the data is not seen in the calculation. Both calculations are cut off at 110°, which is well beyond the possible momentum transfer from an at-rest nucleon.

Figure 1.10 shows a series of calculations of the ratios with different values or δ_e and δ_o. As the VPI phase-shift program only calculates amplitudes up to about 5 fm^{-2} (180° in the π-nucleon center of mass), the same amplitudes are used for π-nucleus center-of-mass angles from 110° through 180°. As ρ^+ and ρ^- depend so critically on the amplitudes, their values should not be taken seriously in the backward hemisphere. r_1 and r_2 are not so amplitude-dependent, and we might expect usable back-angle results for these latter two ratios. In the NSF dip region, the different values of δ_e and δ_o can cause small inflections if the proper combinations are chosen. However, this is not surprising as the NSF amplitudes are changing very rapidly here, and so a slight change in any parameter might be expected to have measurable effects. In the backward hemisphere, using different values of δ_e and δ_o change the magnitude, but not the shape, of r_1 and r_2.

In summary, the major features of the scattering at forward angles and resonance energies are well reproduced by the single-scatterer impulse approximation, as seen by the good match for ρ^+ and ρ^-. The calculation is good up to the region of the NSF dip, as expected. The calculation fails to reproduce the subtler features of r_1 and r_2, which are not so obviously related to the π-nucleon amplitude shapes.

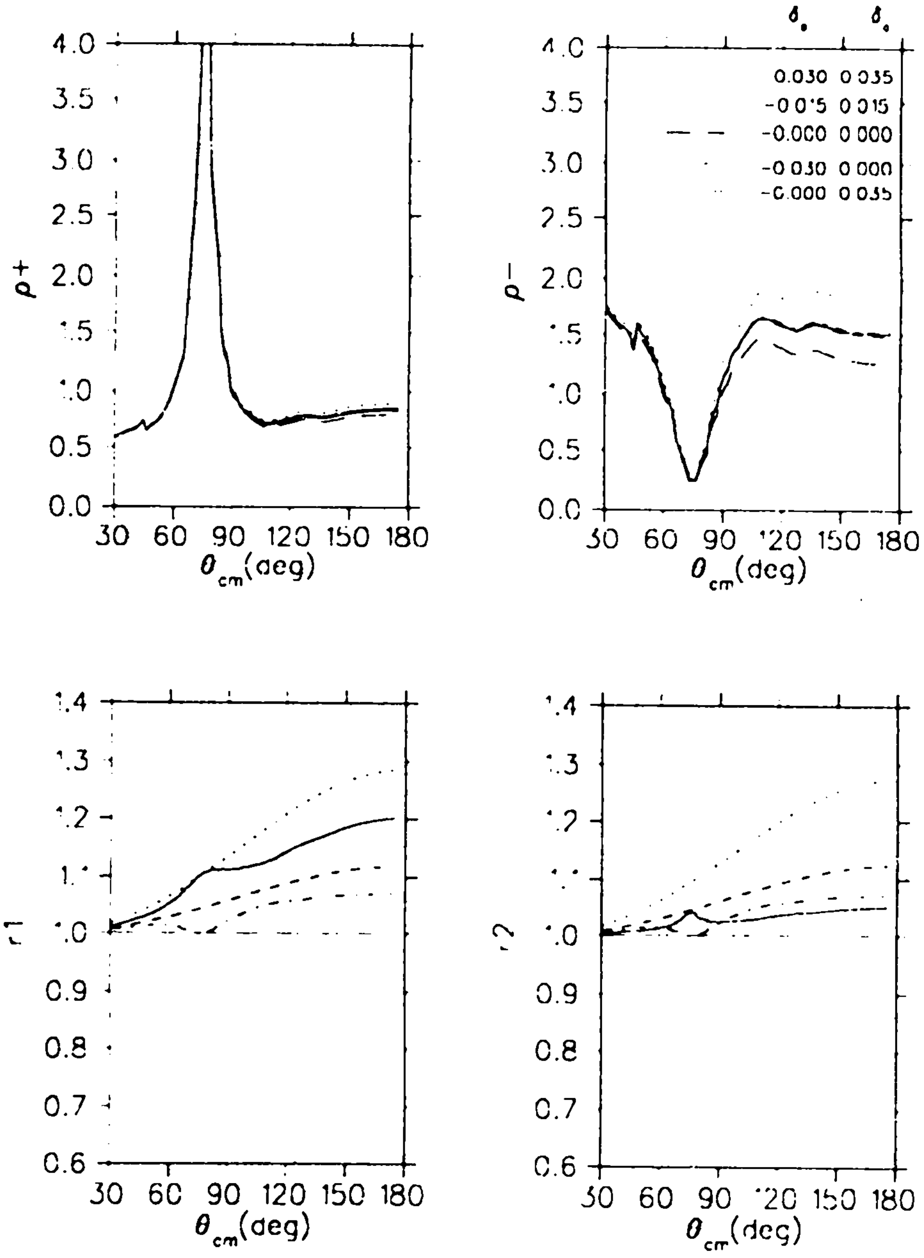

Figure 1.10: Simple model calculation of the ratios at 180 MeV for different values of δ_1 and δ_o. Small changes can cause shape changes in the dip region and large variations in magnitude at back angles, for r_1 and r_2. ρ^+ and ρ^- are not affected appreciably in the forward hemisphere.

1.6.5 The Optical Model

Using equations 1.12, we can derive a more general scattering result [Eis80, Chap.4]. We will be taking the expectation value of T between nuclear ground states and pion states,

$$< T >=< \sum_i^A (t_i + t_i G \sum_{j\neq i}^A T_j) > \sim < \sum_i^A (t_i + t_i G T) >,$$

assuming in the last line that making the sum over j include the i term would only give an error of order $1/A$. This is an acceptable result for large A; for A = 3, it is necessary to make a correction [Gib91] [Ker59]. Ignoring the pion states for now, we take the nuclear ground-state expectation value

$$\begin{aligned} < 0\,|T|\,0 > &= < 0\,|\sum_i^A t_i|\,0 > \\ &+ \sum_\mu < 0\,|\sum_i^A t_i|\,\mu > G_\mu < \mu\,|T|\,0 >, \end{aligned}$$

where the summation over μ is over a complete set of nuclear states, and the subscript on G means that it has the nuclear energy H_μ in the denominator. We can separate the summation into two parts, $\mu = 0$ and $\mu \neq 0$. Then

$$\begin{aligned} < 0\,|T|\,0 > &= < 0\,|\sum_i^A t_i|\,0 > \\ &+ < 0\,|\sum_i^A t_i|\,0 > G_0 < 0\,|T|\,0 > \\ &+ \sum_{\mu\neq 0} < 0\,|\sum_i^A t_i|\,\mu > G_\mu < \mu\,|T|\,0 >. \end{aligned}$$

We assume the final term is not as important as the other two because it involves transitions to excited states and then back to the ground state, and this is less likely than remaining in the ground state the whole time. Defining

$$V_c \equiv < 0\,|\sum_i^A t_i|\,0 >$$

we write

$$< 0\,|T|\,0 > = V_c + V_c G_0 < 0\,|T|\,0 >.$$

This is the form of the Lippman-Schwinger equation for the scattering matrix T for scattering from a potential V. Taking the Born approximation for the scattering amplitude

$$B = < \mathbf{k}'\,|V_c|\,\mathbf{k} >$$

is the first-order optical model. In pion scattering, it has been experimentally determined that a good approximation for the π-nucleon interaction is [Eis80, page 196]

$$< \mathbf{k}' \,|t(E_\pi)|\, \mathbf{k} > = b(E_\pi) + c(E_\pi)\mathbf{k}' \cdot \mathbf{k},$$

for spin and isospin saturated nuclei, with pion energies below 300 MeV. Assuming that the pion interaction is the same with each nucleon, we can rewrite Eq. 1.15 as [Eis80, page 195]

$$< \mathbf{k}' \,|V_c|\, \mathbf{k} > = A < \mathbf{k}' \,|t|\, \mathbf{k} > \int e^{i(\mathbf{k}-\mathbf{k}')\cdot\mathbf{r}} \rho(\mathbf{r}) d\mathbf{r}.$$

Kisslinger noted [Kis55] that this result would be obtained if

$$V_c = Ab(E_\pi)\rho(\mathbf{r}) - Ac(E_\pi)\nabla \cdot \rho(\mathbf{r})\nabla.$$

The problem is thus reduced to determination of b and c at a given energy, and for a given density.

Many groups have enlarged upon this idea, with potentials that include spin and isospin dependent parts, and sophisticated functions for the various coefficients introduced, including b and c above [Lan75], [Str79].

Some applications by other authors to the forward-hemisphere data from these experiments are discussed below.

1.7 Other Calculations

Several groups have calculated the cross sections, as well as some of the ratios. A few of these are considered below.

Nefkens *et. al.* performed an analysis of the forward-hemisphere data using an impulse approximation similar to the one performed in Sec. 1.6.4; that calculation was done after seeing Nefkens' work. The authors used the VPI phase-shift analysis for the π-nucleon amplitudes, and, in calculating the ratios, assumed an exponential shape for the form factors. They also include a shadowing factor designed to model the fact that the nucleon under consideration will be hidden by the other nucleons a certain fraction of the time. Assuming that $f(\pi^+ p\ ) = 3f(\pi^- p\ )$ and $f(\pi^+ p\ ) = f(\pi^- n\ )$, and assuming that the isomirror relations hold as well, and that these also hold for the spin-flip amplitudes, the authors derive the relationships

$$r_2 \sim (F_{nT} / F_{p^3He})^2 \ and$$

$$F_{nT} = [1 + (0.03 \pm 0.02)q^2] F_{p^3He} .$$

The latter equation can be rewritten, assuming that the terms in the square brackets are the expansion of an exponential, as

$$F_{nT} = F_{p^3He}\, e^{0.03q^2} = F_{p^3He}\, e^{2\times 0.05\times 1.74q^2/6};$$

that is $\delta_e = -0.05$, in rough agreement with the value found by Gibbs and Gibson (see Sec. 1.6.4 and below).

Electron scattering from ^{3}He has shown that there is a slight density depletion at $r = 0$ [McC77]. Equation 1.14 can be written as follows, if the density is assumed spherical:

$$F(q) \propto \int j_0(qr)\rho(r)r^2 dr$$

where j_0 is the spherical Bessel function. We can transform this and write

$$\rho(r) \propto \int j_0(qr)F(q)q^2 dq.$$

The integrand in the latter is a damped sine function; if we write the form factor as the sum of two gaussians, $F = F_1 + F_2$, we can match the density depletion well.

Barshay and Seghal[BarS5] have assumed a correlation among the nucleons in ^{3}He that allows them to fit a form factor written as the sum of two gaussians to the known form-factor shape. The diagram shown in Fig. 1.11 is from their paper. The np distance is the same in both nuclei in the figure, and by using this and defining the center of mass to be at the same place for both, they derive the equation

$$R_p^2 + 2R_n^2 = 3R_t^2.$$

Next, they define the form factors as

$$F^T = (1 - \epsilon)e^{-R_1^2 q^2/6} + \epsilon e^{-R_t^2 q^2/6},$$

for the equal proton and neutron form factors of T, and

$$F_{p,n}^{He} = (1 - \epsilon)e^{-R_2^2 q^2/6} + \epsilon e^{-R_{p,n}^2 q^2/6},$$

for the proton and neutron form factors of ^{3}He. R_1 and R_2 are the numbers that give the 'regular' gaussian form factors, that is they are the radii for uncorrelated nucleons. Using the correlation equation and the known values of the T and ^{3}He charge form factors from electron scattering, the authors determine the following values for the parameters:

$$\begin{aligned}
\epsilon &= 0.27, \\
R_1 &= 1.67 fm, \\
R_2 &= 1.74 fm, \\
R_T &= 1.12 fm, \\
R_p &= 1.31 fm \text{ and} \\
R_n &= 1.02 fm.
\end{aligned}$$

The authors calculate r_1 and r_2 using the single-scattering impulse approximation given in Sec. 1.6.4, but they use only the p-wave part of the amplitudes, that

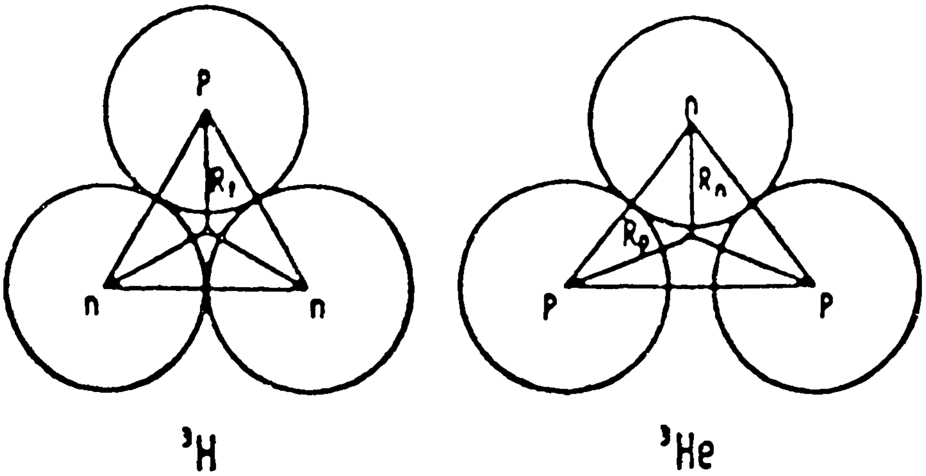

Figure 1.11: Figure from [Bar85], T on the left, and ^{3}He on the right. T is an equilateral triangle, with nucleon radius R_t. ^{3}He is an isosceles triangle with proton and neutron radii R_p and R_n, respectively.

is

$$\begin{aligned}
f(\pi^+p\ ) &= f(\pi^-n\ ) = 2\cos(\theta),\\
f(\pi^+n\ ) &= f(\pi^-p\ ) = \frac{2}{3}\cos(\theta),\\
g(\pi^+p\ ) &= g(\pi^-n\ ) = \sin(\theta)\ and\\
g(\pi^+n\ ) &= g(\pi^-p\ ) = \frac{1}{3}\sin\theta.
\end{aligned}$$

Figures 1.12 and Fig. 1.13 reproduce the authors' calculations (on the left in each figure), and show the same calculations done using the VPI-phase-shift amplitudes instead of the p-wave forms, (on the right in each figure). Note that the authors did not calculate ρ^+ or ρ^- , but as they gave the values for all of their parameters, it is easy to do the calculation using their method; this is done here. Their r_2 result is especially intriguing as the bump and return to 1.0 is reproduced fairly well. Their r_1 calculation has a similar but smaller bump; the shape is similar to that reported by Exp. 546 (□, [Nef90]), but the other data, taken with the new targets and using Deuterium for normalization cross sections (×, [Pil91] and ◇, [Pil92], [Ber91]), are flatter, and further from the calculation. Their ρ^+ and ρ^- results are shifted from the data, but have the correct shapes otherwise. The calculation was redone, using the VPI amplitudes with the authors' form factors; the results are shown on the right in each figure. ρ^+ and ρ^- are now a good match for the data, but r_2 no longer comes back to 1.0 after the hump. There is still a slight inflection; evidently the good match in the authors' result was somewhat fortuitous, as smoothing out the cosine dependence by including other than p-waves eliminates the good match with the data.

Kim, Krell and Tiator [Kim86] and Kim, Kim and Landau [Kim87] have done optical model calculations in an attempt to explain the forward-angle ratios. In their calculations, they consider only the Coulomb interaction as a source of CSB.

The first of these papers looks at both nuclear-Coulomb interference and Coulomb repulsion of the protons of ^{3}He; no spin dependence is included in the calculation. The densities are exponentials

$$\rho_p(r) = N_p e^{-\frac{3}{2}r^2/r_p^2}\ ,\ \rho_n(r) = N_n e^{-\frac{3}{2}r^2/r_n^2},$$

where the subscripts n and p refer to neutrons and protons respectively, and N is the number of nucleons of a type, either neutrons or protons. The authors find a nuclear-Coulomb interference-related structure in r_1 , r_2 , and R, around 90° in the π-nucleus center of mass, which is well beyond the ~ 78° location of the NSF dip, with CSB due only to Coulomb interference, and not proton repulsion. When they include proton repulsion in ^{3}He, by increasing r_p by 0.03 fm in ^{3}He, they see a similar structure; this addition makes r_1 , r_2 and R greater than 1.0 in the backward hemisphere. In both cases, the backward hemisphere ratios are smooth and structureless. These calculations, which are sketched over the data

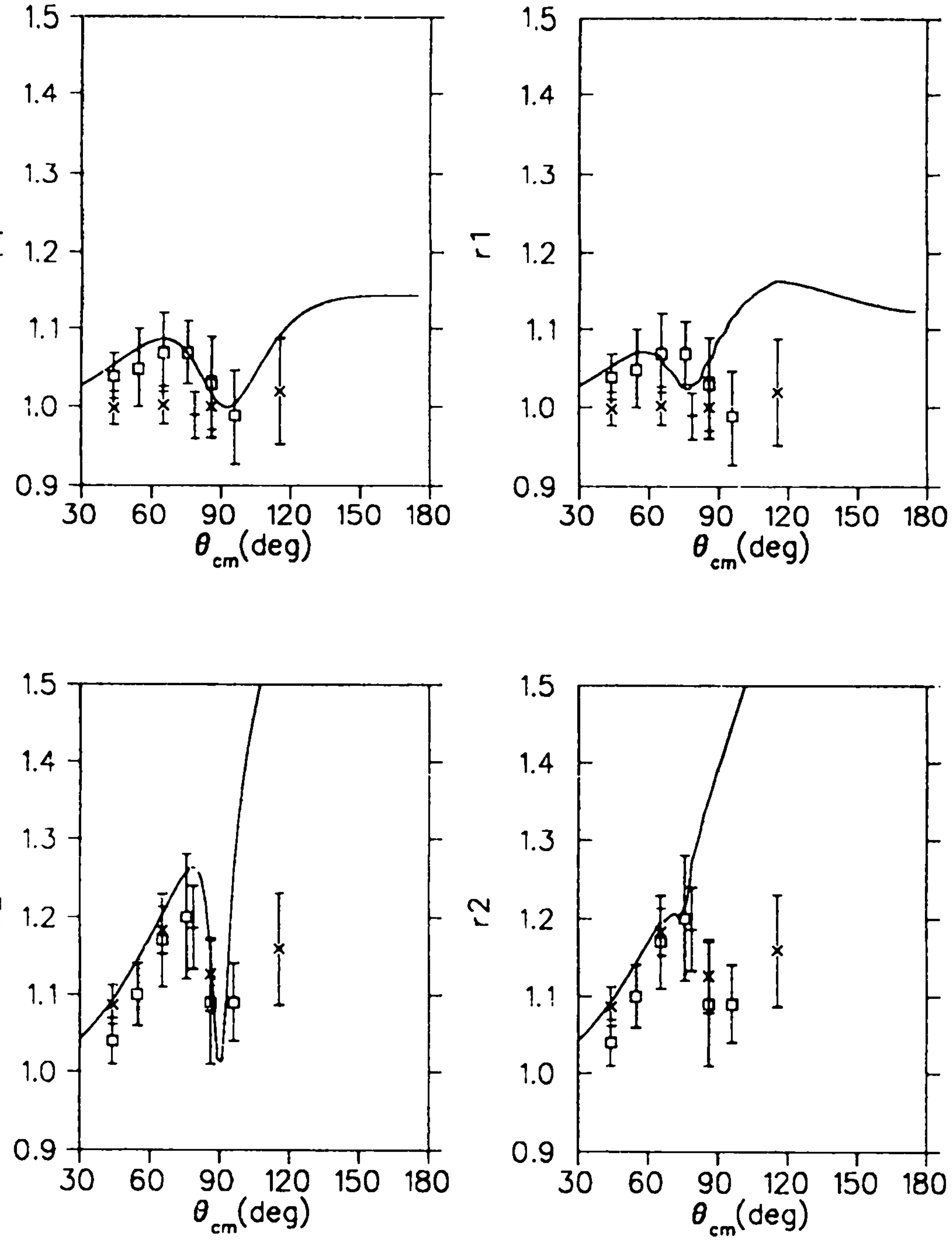

Figure 1.12: r_1 and r_2 calculated in a single-scattering impulse approximation, using sum-of-gaussian form factors, from [Bar85]. *left:* Using p-waves only. *right:* Using VPI-phase-shift amplitudes. The bump in r_2 is reproduced fairly well using the p-wave-only formulation.

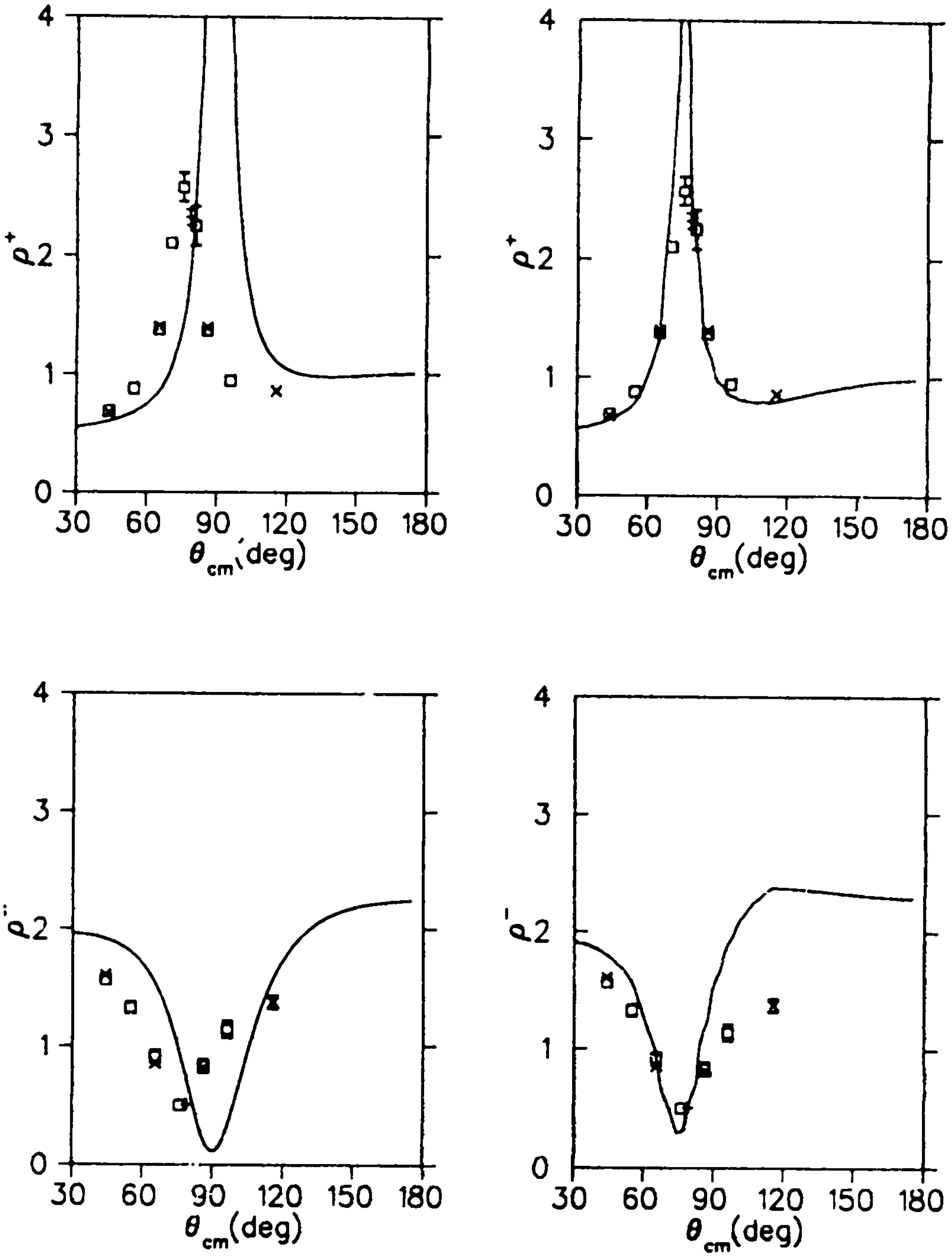

Figure 1.13: ρ^+ and ρ^- , using sum-of-gaussian for factors from [Bar85] and a single-scattering impulse approximation. *left:* p-wave-only amplitudes. *right:* VPI-phase-shift amplitudes.

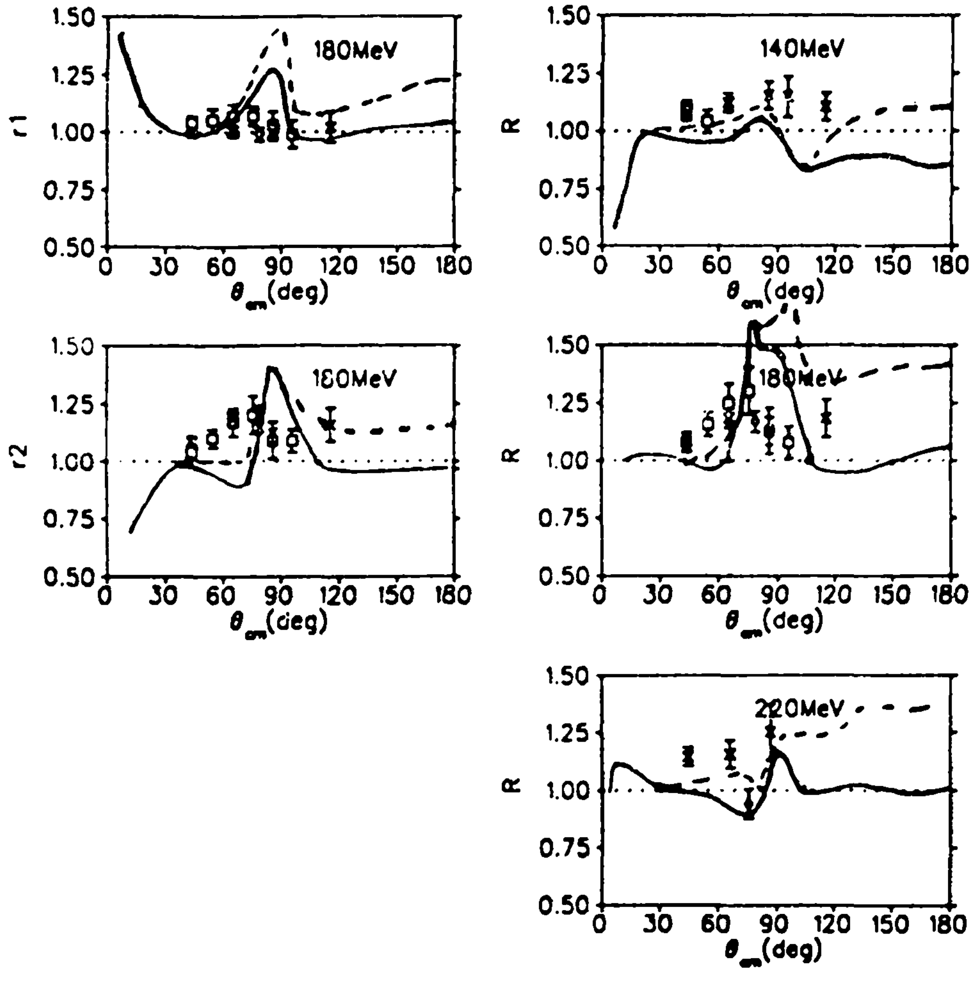

Figure 1.14: Ratio calculations by Kim, Krell and Tiator [Kim86], sketched over the data. The solid lines are their calculation for π-nucleus scattering including Coulomb interference, but no Coulomb repulsion in ^{3}He. For the dotted lines, they add Coulomb repulsion in the form of an additional 0.03 fm separation in the ^{3}He-proton radius. The data available when this calculation was done was only from experiment 546. □ Exp. 546 [Nef90], × Exp. 905 [Pil91], ◇ Exp. 1032 [Pil92] and [Ber91].

in Fig. 1.14 which was taken from the reference, show that while the calculation does not represent the data very well, the nuclear-Coulomb interference should not be ignored, and that at least at back angles, the optical-model calculation is very sensitive to the nucleon separation, which means that it is very sensitive to the form factors.

The second paper [Kim87] considers only nuclear-Coulomb interference as a source of CSB. The authors use a momentum-space optical potential, which includes spin-flip interactions. They do a credible job on R on the large-angle side, matching the slope and coming back to 1.0 around 100° in the π-nucleus center of mass, where they found the nuclear-Coulomb interference structure in the previous paper. The rest of the angular region is not a very good match. Specifically, their curves are very flat between 30° and 65°, where the data show a significant deviation from 1.0 with a smooth slope in r_2 , and consequently in R. Their bump is too narrow in r_2 and R; however the height is in keeping with the later data sets (◇, ×) and they find the peak at the right location (around 78° in the π-nucleus center of mass). In their previous paper, added proton separation in ^{3}He gave some deviation from 1.0 in the region forward of the NSF dip, and some added deviation and shape in the backward hemisphere; possibly this lack explains the corresponding lack in these regions in the second paper. Figure 1.15 is a sketch of their results over the existing data. Kim *et. al.* claim to have shown that the structure in R in the NSF dip region is due solely to Coulomb interference. However, as suggested by Briscoe and Silverman [Bri89], considering that they have only identified a structure whose location is near the NSF dip, while missing the amplitude and width of the structure as well as failing to reproduce the rest of the data, it seems more reasonable to say that they have shown that Coulomb interference has a non-negligible effect in this region, and should be included in any complete treatment.

A more recent momentum-space optical-model calculation has been performed by Gibbs and Gibson [Gib91]. Their calculation includes spin-flip scattering and Coulomb scattering and repulsion. They calculate cross sections and R. They state that the major dependence found in their scattering calculation was on the neutron and proton radii. Actually, they assume that the proton radii are known from elastic electron scattering, and they search for values of δ_e , which is the difference between the neutron radius in T and the proton radius in ^{3}He, and δ_o , which is the difference between the neutron radius in ^{3}He and the proton radius in T. For each combination of the scattering-theory parameters, they perform a chi-square fit to the data to determine the best values of δ_e and δ_o . Their results are

$$\delta_e = -0.030 \pm 0.08 fm$$

and

$$\delta_o = 0.035 \pm 0.07 fm.$$

Figure 1.16 shows their calculation of R : they do a reasonable job on the forward

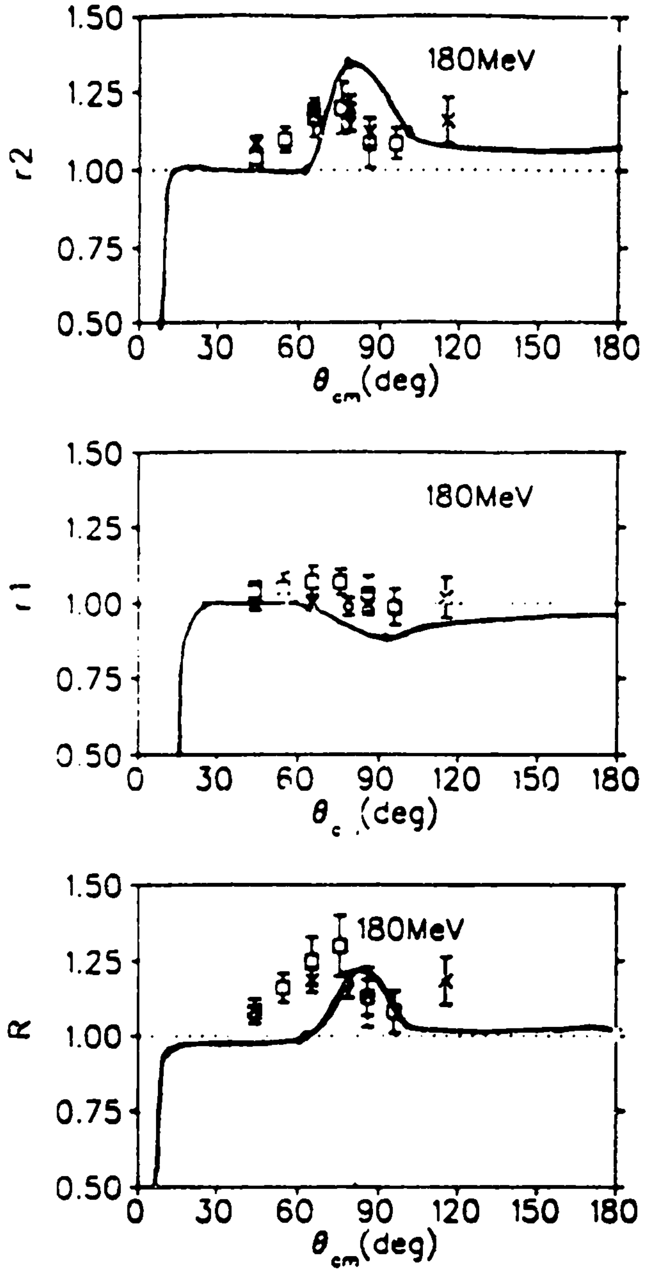

Figure 1.15: Calculations by Kim, Kim and Landau [Kim87]. CSB is included by nuclear-Coulomb interference only. The large-angle slope of R is well represented, in the region that the authors previously found the interference related structure in R. Only the experiment 546 data was available at the time of the calculation. □ Exp. 546 [Nef90], × Exp. 9C [Pil91], ◇ Exp. 1032 [Pil92] and [Ber91].

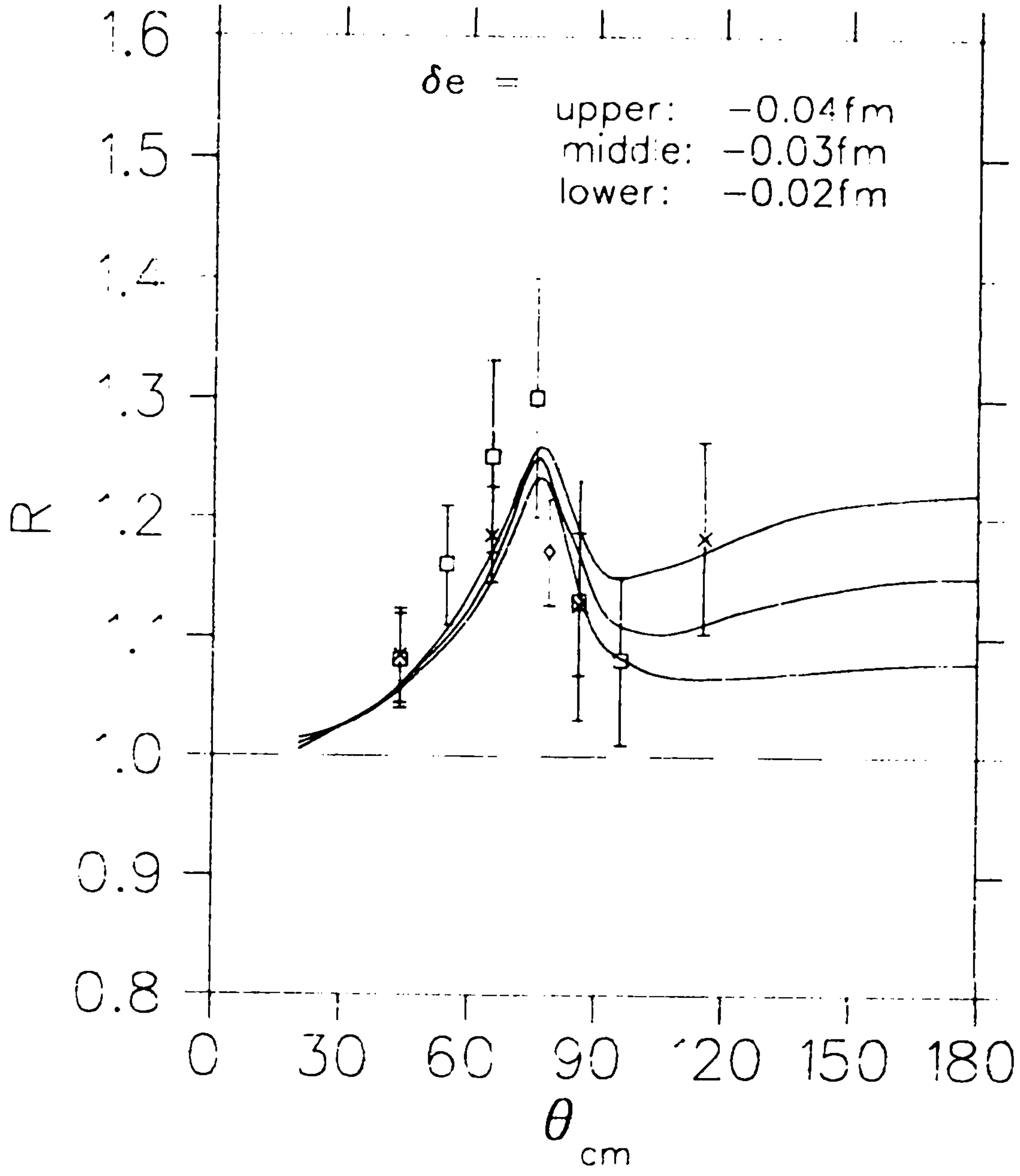

Figure 1.16: R from Gibbs and Gibson[Gib91]. The three curves show the effects of varying δ_e by ±.01 fm, assuming δ_o = 0.035 fm. □ Exp. 546 [Nef90], × Exp. 905 [Pil91], ◇ Exp. 1032 [Pil92] and [Ber91].

hemisphere data. Variations of 0.01 fm in δ_r make a noticeable change in their backward hemisphere curves.

Figure 1.17 shows their cross section calculations, using the parameters that gave the best R results. They have produced a good match in the dip region, although a little high for π^{+3}He. The similarity of the symmetric pairs is obvious (diagonal from each other in the figure).

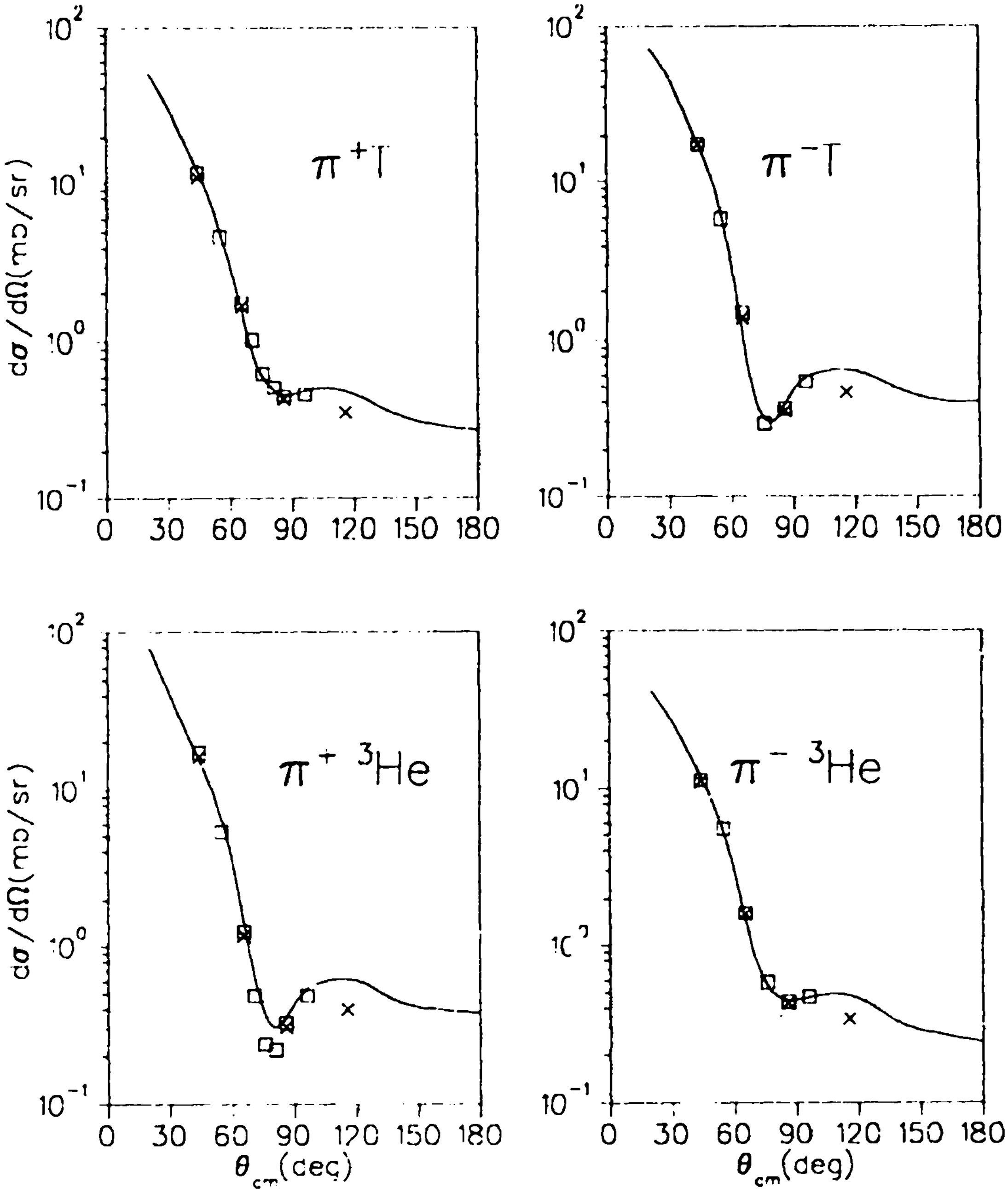

Figure 1.17: Cross section calculations from[Gib91]. The dip region is reproduced quite well. □ Exp. 546 [Nef90], × Exp. 905 [Pil91], ◇ Exp. 1032 [Pil92] and [Ber91].

1.8 Summary

The most dramatic features of the forward-hemisphere results are due to the NSF dip. The simple ratios ρ^+ and ρ^- were well-reproduced by the Simple-Model calculation done in Sec. 1.6.4; the most important input was the π-nucleon amplitudes, which were taken from the VPI phase-shift analysis, assuming a non-moving nucleon. The calculation failed to reproduce the bump in r_2 . In that calculation, Backward-hemisphere values of r_1 and r_2 depend mostly on the radii used in the exponential form factors. Kinematical considerations indicate that multiple scattering should be relatively more important in the backward hemisphere.

Calculations by Kim and collaborators [Kim86] [Kim87] failed to reproduce the ratios but did show that Coulomb interference could make important contributions in the region of the NSF dip.

Finally, calculations by Gibbs and Gibson [Gib91] yielded precise values of δ_e and δ_o and matched the forward-hemisphere cross sections and R data quite well. This calculation included Coulomb interference in a potential interaction model. The authors state that they need to include NCSB in the form of added proton repulsion in a nuclear model in order to reproduce the values of ρ^+ and ρ^- found in the scattering calculation.

Backward-hemisphere measurements will extend the pion-elastic scattering data from T and ^{3}He into previously uncharted regions. Data taken farther from the NSF dip will not suffer the difficulties due to the steeply changing amplitudes in this region, and so it may be possible to understand systematics of the scattering calculations that are obscured near the dip. As the scattering angle approaches 180°, the spin-flip amplitudes approach zero, and comparisons with scattering from spin-zero nuclei, specifically ^{4}He, might be revealing.

The question of charge-symmetry breaking remains. In the backward hemisphere, we might expect to benefit from a lack of Coulomb interference, if this latter is primarily manifested in the region of the NSF dip, as suggested by the authors mentioned in Sec. 1.7. However, the expected increase in the importance of multiple scattering in the backward hemisphere may introduce complications that outweigh the benefits.

Historically, measurement of the excitation function near 180° (Experiment #1064) was proposed to and accepted by the LAMPF Program Advisory Committee before the angular distribution experiment (Experiment #1155) was proposed. The proposal for Exp. 1064 [Bri86] stated that the primary purpose of the experiment was to provide πT and π^3He cross-section data in kinematical regions previously uncharted for these nuclei. It was noted that comparison of the charge-symmetric ratios near the NSF dip, where non-spin-flip scattering is nearly zero, to the ratios measured near 180°, where nearly all of the single scattering is spin-flip (recall the sine dependence of the spin-flip amplitudes), might show the relative amounts of NCSB in the spin-flip and non-spin-flip amplitudes.

The primary justification for Exp. 1155 [Bri87] was a series of preliminary calculations by Gibbs and Gibson [Bri87] showing that a R calculation at 180 MeV would be rather insensitive to model variations in the description of the π-nucleon force, and would depend mostly on the nuclear radii chosen for the nucleons in T and ^{3}He. They stated that a complete angular distribution, and thus a complete measurement of the momentum-transfer dependence of the problem, would be necessary to correctly derive the radii (recall that the radius and momentum transfer are related through the form factors). These preliminary calculations eventually led to the full calculation and back-angle predictions discussed in Sec. 1.7.

The goal of this work is to provide the back-angle excitation-function and angular-distribution data needed, to extend the data base, to test the backward-hemisphere predictions of the authors discussed in Sec. 1.7, and to explore the relative CSB of the non-spin-flip amplitudes.

Chapter 2

Experimental Equipment and Setup

2.1 Introduction

The experiments were performed over a six week period in the summer of 1989, using the Energetic Pion Channel and Spectrometer (EPICS) at the Clinton P. Anderson Meson Physics Facility (LAMPF), which is a part of the Los Alamos National Laboratory, in Los Alamos, New Mexico. In addition to the standard EPICS setup we used an extra bending magnet, a special target changer and high-pressure gas targets.

2.2 LAMPF

LAMPF is a quarter-mile-long proton accelerator that produces a beam of 800-MeV protons at currents of up to 1000 μa. In addition to the main proton beam (H^+), H^- ion beams can be transported on the opposite phase of the RF. The H^- beams serve the proton and neutron scattering areas, and can be polarized for some applications; these latter beams were not used in these experiments.

The protons are focused on graphite production targets to produce secondary pion beams. Pions of various momenta are selected by magnetic optical systems ('channels') which have entrances at angles to the proton beam downstream of the targets; the angles are selected to maximize pion flux in a given momentum range. Different pion channels produce pion beams with different qualities, such as special energy ranges and linearly dispersed momentum. The pion beams are focused on nuclear targets, and the scattering-reaction products are analyzed in order to understand the reaction processes and ultimately the nuclear structure of the targets.

2.3 EPICS

2.3.1 Channel and Spectrometer

The EPICS channel produces a pion beam with an energy range of 70 - 300 MeV. The beam is 8 cm wide and 20 cm high with a vertical momentum dispersion of $10cm/percent$. The rate for π^+ is about 3×10^7 *per* second at 70 MeV and increases to about 26×10^7 *per* second at 290 MeV. Rates for π^- are about one-fifth of the π^+ rates, depending on the beam energy; the ratio reflects the relative production rate in the graphite target. The beam is monitored in several ways. There is a toroid upstream of the production target in the proton line which monitors the proton current. Since the pion production at any particular energy and angle (the angle of the channel relative to the proton beam) is proportional to the proton current, the toroid current is proportional to the pion current. However, if the primary proton beam is shifted slightly due to tuning changes in the accelerator, it will hit the production target at a slightly different angle and location, causing the pion flux and angle to change as well. Therefore the proportionality constant between the pion beam current and that of the proton beam, as measured by the toroid, is dependent on the proton-beam steering at the production target.

The second monitor is an ion chamber in the production-target box that views the graphite production target. As the ion-chamber current is proportional to the proton-beam current, using the former to normalize the pion beam has the same problems as using the toroid does. This monitor failed during the experiment; it has not been used for any quoted results.

The primary pion-beam monitor is an ion chamber that views the pion beam directly. It is mounted on a stand in the experiment area and intercepts the beam after it passes through the target and scattering chamber. This ion chamber is faced with a 1-inch graphite slab to reduce the number of protons that are detected (protons are present in the π^+ beam from scattering of the proton beam on the production target). The current from the ion chamber is proportional to the total energy deposited by all the charged components of the beam: muons, electrons, protons and pions. Since these constituents are in constant proportion to each other at each energy, the ion-chamber current is proportional to the pion current at each energy.

Seestrom [See81] found that there is a proportionality inconsistency between π^+ and π^-. Quantifying this difference requires a detailed knowledge of the pion-beam composition and its interaction with the ion-chamber gas. This is not important in these experiments, because all cross sections and cross-section ratios have yields of like polarity in both their numerators and denominators, so the proportionality constants cancel (see Chap. 3).

Protons can be removed from the pion beam by moving one or more polyethelene or beryllium degraders into the beam in the channel. A proton traversing the degrader loses more energy than a pion of the same momentum. After the traversal, passing the beam through a bending magnet separates the lower momentum protons from the pions. The protons miss the target at the end of the channel and are lost. In this experiment, the protons and the pions were not kinematically matched after scattering, that is the scattered protons had too little momentum to make it through the spectrometer, so the degraders were not used.

The channel terminates at the scattering chamber, which holds the target in vacuum. The channel and scattering chamber are often vacuum coupled, but the scattering chamber used in the back-angle setup for these experiments rotates with the spectrometer pivot, and no provisions have been made to provide coupling. Instead, the beam pipe was terminated with a thin Kapton window. A few-inch air gap separated it from the mylar window of the scattering chamber, which was 25 cm × 120 cm by 0.038 cm thick. The mylar was epoxied to an aluminum frame, and this frame was bolted to the window frame of the scattering chamber. Entries to the scattering chamber required releasing the vacuum and removing the frame, which flexed the window and glue. A new window was required every few entries.

The spectrometer is mounted on air pads and can be rotated up to a floor angle of 120° relative to the beam. It consists of two large dipoles that bend the beam in a vertical plane for momentum analysis and a quadrupole triplet at the spectrometer's entrance to provide point to point focusing in the vertical plane, which maintains the momentum dispersion of the incoming beam, and point to parallel focusing in the horizontal (scattering) plane. The coordinate system at EPICS is right handed with the positive z-direction along the beam. The x axis is positive downward and the y axis is positive to the left, looking downstream.

Particle tracks are monitored with three groups of wire chambers. The first group brackets the focal plane of the quadrupole triplet, one x-direction and one y-direction chamber upstream and the same x-y combination downstream, allowing determination of the x and y position of a particle track as well as the angle of the track with respect to the central ray. After the dipoles four x-y pairs are used to analyze the position and angle again.

Three scintillators provide event timing. The first (S_1) is just before the front chambers, and the second and third (S_2, S_3) are behind the last chambers. A good event must be seen by at least one pair of front chambers and the two rear scintillators; this combination forms the trigger. S_1 can be removed from the flight path, as was done for this experiment. When S_1 is left in, it is included in the trigger as well. A time-of-flight correction is done between the front and rear detectors based on the particle's energy as well as its calculated flight path length, in order to reference events in the front and rear of the spectrometer to a common time.

Figure 2.1 is a schematic diagram of the EPICS spectrometer, seen in the vertical plane. A hardware trigger is made from signals from several component detectors of the spectrometer. If each of these detectors outputs a logical signal simultaneously, it indicates that a particle has passed through the complete spec-

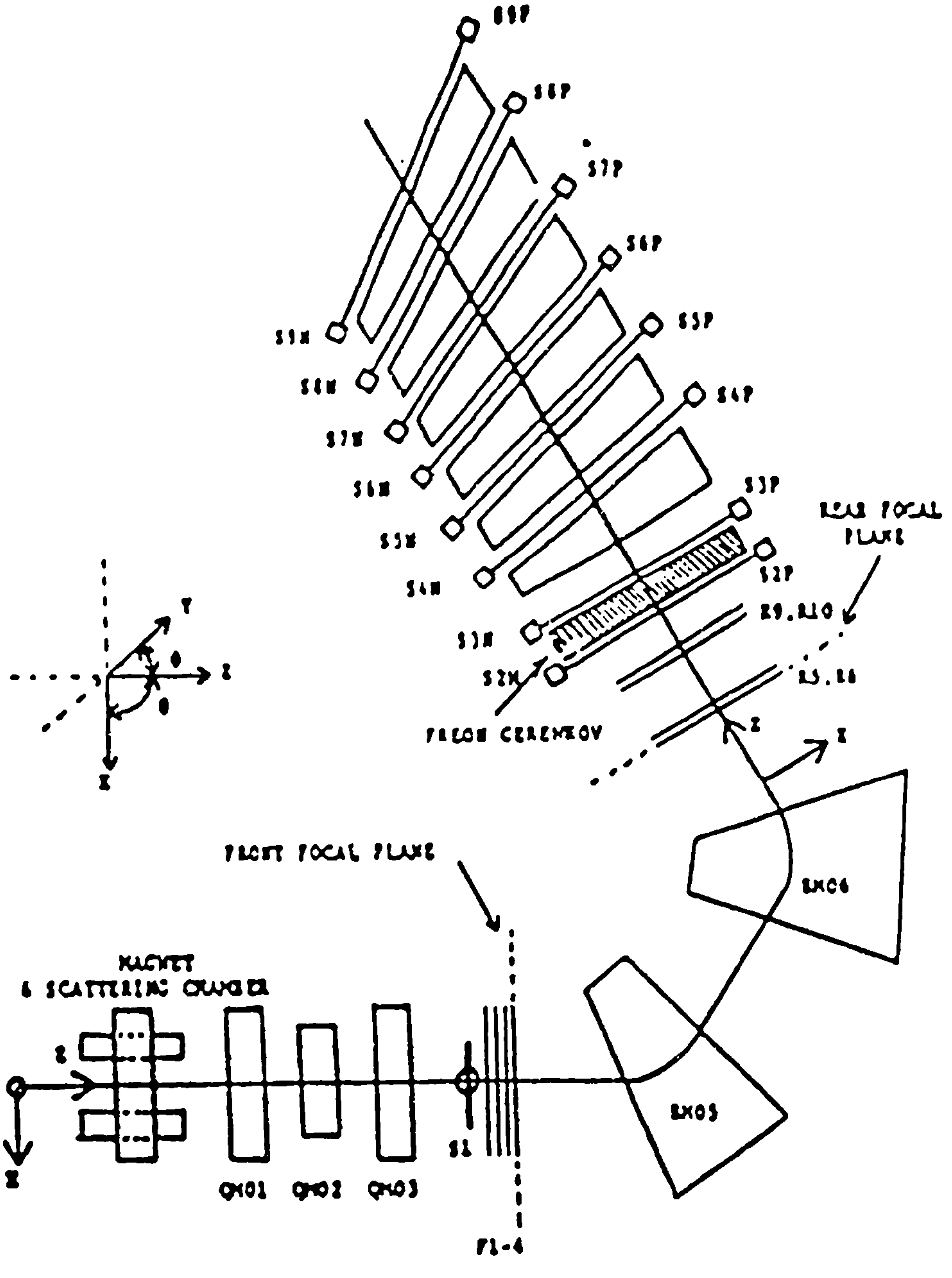

Figure 2.1: A schematic view of EPICS from the side.

trometer. A logical AND is formed and input to the LAMPF trigger module, which is a rack mounted module with several inputs. In response to an input, such as the event trigger, the trigger module signals the data-acquisition systems, over the data bus, that it has an event to be processed, and indicates the event's priority. Recently, a buffering capability has been added that allows up to 15 events to be stored and read out later. The LAMPF beam structure has a pulse that lasts for about 10% of the RF cycle, so that data can be stored during the pulse, and then read out from the buffers during the time between pulses.

The detector outputs are processed by time-to-digital (TDCs) converters, which digitize the time between start and stop pulses, and analog-to-digital converters (ADCs) which measure pulse height. Also, scalar registers keep count of pulses from discriminated detectors and current digitizers. This data is stored in the buffers and read out for each event. Readout is controlled by a LAMPF Micro-programmable Branch Driver (MBD), and the events are processed and written to tape by a micro-Vax computer.

On-line analysis is also possible for most of the events, depending on the data-taking rate. The angle, momentum, and target location of each scattering event are calculated using the wire chamber information (see Sec. 2.3.3). The excitation energy of the target nucleus, 'missing mass', is calculated from these results, and all of the calculated and raw data are histogrammed and can be displayed immediately.

2.3.2 Wire Chambers

EPICS has six x-chambers and six y-chambers. Their construction, calibration, and operation are discussed in [Ate81] and [Mor82]. They are drift chambers with interleaved sense and field wires. The signal wires are 0.8 cm apart, so that each drift cell is 0.4 cm. Each anode wire is connected to a delay line. Both ends of the delay line are read out, and each is used as a TDC stop; the times recorded for the two ends are called t_1 and t_2. A sum ($t_1 + t_2 \equiv t_s$) and a difference ($t_1 - t_2 \equiv t_d$) are formed for each event. The sum is the time it takes the signal to propagate from one end of the delay line to the other plus the time between the start and the actual event, plus twice the time it took the signal to get through the drift cell and down the signal wire to the drift line. If we assume that propagation down the signal wire is instantaneous, then t_s

equals the drift time plus a constant. For EPICS chambers, we assume that each drift cell is uniformly illuminated, which is reasonable for such small cells. Then, the number of particles seen per unit drift time is

$$\frac{dN}{dt} = \frac{dN}{ds}\frac{ds}{dt} = cv(t)$$

where s is the drift cell position. Integrating gives

$$s(t) = \frac{1}{c}\int_0^t \frac{dN}{dt}dt$$

and so s is a function of t. The histogram $N(t_s)$ is binned in 0.8 ns bins, and then integrated to give a table for $s(t_s)$. This creates a lookup table for s, with a nominal resolution of $\sim 40\mu m$ [Mor85].

The difference in the times ($t_1 - t_2 \equiv t_d$) is used to decide which wire was hit. If we assume that

$$x = a_0 + a_1 t_d + a_2 t_d^{\,2}$$

where x is the position along the delay line, and a_2 should be small, then if we histogram the quantity

$$k = nearest\ integer(\frac{x}{w})w$$

where w is the wire spacing, we can find values for $a_{0\,1,2}$ by minimizing χ^2 in

$$\chi^2 = \sum_i (x_i - k_i)^2$$

[Mor82]. All of these calibrations are done with standard EPICS software.

The interleaved cathode wires are bussed into two sets, the odds and the evens. Thus, a signal that happens in a cell will be seen either by an even or an odd cathode wire, and this signal allows us to determine on which side of the signal wire the event occurred.

2.3.3 Calculated Quantities

The wire chambers are used to measure eight quantities for each event. These are the x and y positions in the front chambers, X_{front} and Y_{front}, the angles the track makes with the central ray in the vertical and horizontal planes, θ_{front} and ϕ_{front}, and the equivalent quantities in the rear chambers, X_{rear}, Y_{rear}, θ_{rear} and ϕ_{rear}. These are enough to calculate four target quantities, X_{target}, Y_{target}, θ_{target} and ϕ_{target}, corresponding to the values of the positions and angles at the target, that is, at the scattering event.

Each of the target positions and angles can be written as functions of the chamber quantities, for example

$$\begin{aligned} X_{target} &= a_{11} X_{front} + a_{12} Y_{front} + \ldots \\ &+ a_{21} X_{front}^{\,2} + a_{22} X_{front} Y_{front} \ldots \end{aligned}$$

where terms are included up to third order. In order to find the coefficients, segmented targets are used to give definite values of X_{target} and Y_{target}. For example, to calibrate Y_{target}, a set of three vertical graphite rods are placed in a standard EPICS target holder. If a rudimentary set of coefficients is available from a beam optics-calculation, then *elastic*-scattering events can be predicted fairly well from the chamber quantities. (Elastic events are necessary so that a complete kinematical calculation can be performed for each event). A reasonable Y_{target} histogram can be formed using these coefficients. Since the position of the rods is precisely known, each broad peak in the intermediate histogram can be assigned a true value of Y_{target}, and this value, and these for many other events, can be used in the above equations to solve for the true coefficients. Once the coefficients are determined (this is also done with standard EPICS software), a file of the coefficients is created. When an event is analyzed, the chamber quantities are combined with the appropriate coefficients to get the target quantities.

In order to get the coefficients for θ_{target} and ϕ_{target}, we need not only a set of rods, but a set of slits as well, in order to have known angles to look at. The slits are placed beyond the rods, so that the angle between a rod and a given slit is known. A two dimensional plot of angle *vs.* rod position shows different groups of points; each group refers to a rod and angle, and grouping the points for each angle gives the known quantity needed for the polynomial calibration. The same procedure as for X_{target} and Y_{target} is followed thereafter. θ_{target} and ϕ_{target} were not recalibrated with the bending magnet in place.

θ_{check} and ϕ_{check} are useful quantities as well. θ_{check} is the difference between θ_{front} and θ_{rear}. We expect that the optics will preserve this angle, and so θ_{check} should be zero. If a pion decays into a muon during its flight in the spectrometer, and then the muon is detected in the rear chambers, θ_{front} will not be the same as θ_{rear} because the muon usually comes off at an angle. If the angle is large, then the muon will not be within the spectrometer's acceptance, and so the event is lost. However, if the decay happens at one of the spectrometer's focal points, the acceptance will be large, and the muon may not be lost. In this case, requiring θ_{check} and ϕ_{check} to be within 10 mrad of zero is an effective method of muon rejection, as less than 1% of decay muons fall within this cone at EPICS energies ([Mor85], and see Sec. 2.3.4).

δ is the fractional difference in the particle's momentum (p) from the central momentum of the spectrometer (p_0).

$$\delta = \frac{p - p_0}{p_0}.$$

It is computed from an expansion like the target quantities are; it is also calibrated with elastic scattering.

Once X_{target} has been calibrated, we can tell where x, the x-dimension of the target the particle scattered. Since x is the direction of the beam dispersion, we know the incoming-particle momentum. Since we know the outgoing angle as well, we know the momentum of the particle, and if we know the central momentum of the spectrometer, we know the true δ for elastically scattered particles.

If δ has been crudely calibrated, then the missing mass calculation can identify events in the elastic peak, and these elastic events can be used to determine the coefficients in the delta expansion. In practice, the spectrometer is tuned for several different central momenta so that the scattered particles illuminate the entire area of the rear chambers; this gives a set of polynomials that is good over the entire focal plane.

The calculated quantities give a complete description of the scattering event; incoming and outgoing momenta are completely specified, and so a description of the interaction that includes nuclear excitation of the target is possible. The spectrum of scattered pions is plotted as a function of the excitation energy of the target, and called missing mass.

2.3.4 Muon Rejector

Muons in the spectra can come from several sources. They are present in the pion beam at the level of a few percent. Since they do not interact via the strong force, their cross sections are much smaller than those of the pions. To get an order-of-magnitude estimate of this problem, we note that the Coulomb-muon cross sections should be on the order of $(\frac{1}{137})^2$ smaller than the strong-force dominated pion elastic cross sections. Assuming the beam is 10% muons, we would have a fraction of muons in the scattered pions of $\frac{1}{137}^2 \times .1 = 5 \times 10^{-6}$, which is negligible.

Scattered pions can also decay into muons. Many of the muons from decay can be removed by the angle checks (see Sec. 2.3.3), but some will be inside the 10 mrad cone used for this test. Furthermore, if the decay happens before the first set of wire chambers, then the muon will be a legitimate particle in terms of this test. These muons form an extra background in all of the histograms.

Figure 2.2 shows a spectrum for elastic scattering at 120°. Pions decay into muons and neutrinos with 30 MeV/c of momentum in the pion rest frame. The decay is isotropic in this frame, and transforms into forward and backward cones in the lab frame. For 180 MeV pions, scattered from T at 120°, the half-angle of the cone is 9°, much larger than the 1.5° half-angle of the spectrometer acceptance in the y-z plane. At these kinematics, the pion has 245 MeV/c momentum, and muons that decay parallel to the pion momentum, forward or backward, have momenta of 254 MeV/c and 132 MeV/c, respectively, or deltas of of 3.7% and -46%. The positive value, which corresponds to counts to the left of the peak in missing mass, is well within the acceptance. A 3.7% delta corresponds to -7.8 MeV excitation in the pion missing mass spectrum, about 800 channels to the left of the peak in Fig. 2.2. Muons with angles to the central ray of 1.5° will have forward momentum of 254 MeV/c × cos(1.5°) ~ 254 MeV/c, since cos 1.5° = 0.9997, so the resolution of the muon and pion peaks should be similar. Figure 2.2 has a mark at -8.0 MeV, to show the location of the muon peak. The base of the pion elastic peak is ~ 8 MeV wide, and assuming the same base for the muon peak, we would not have any overlap of the tails.

The distance from the target to the front chambers is about five meters. In this distance, for 180 MeV pions scattered at 120°, 42% of the pions decay, so about half of the particles passing the first chambers are muons. If 5% of these decays are in the forward direction such that the muons match the spectrometer acceptance, the muon peak on the left side of the pion elastic peak will have 5% of the pion peak's area. The spectrum shown in Fig. 2.2 has the smallest

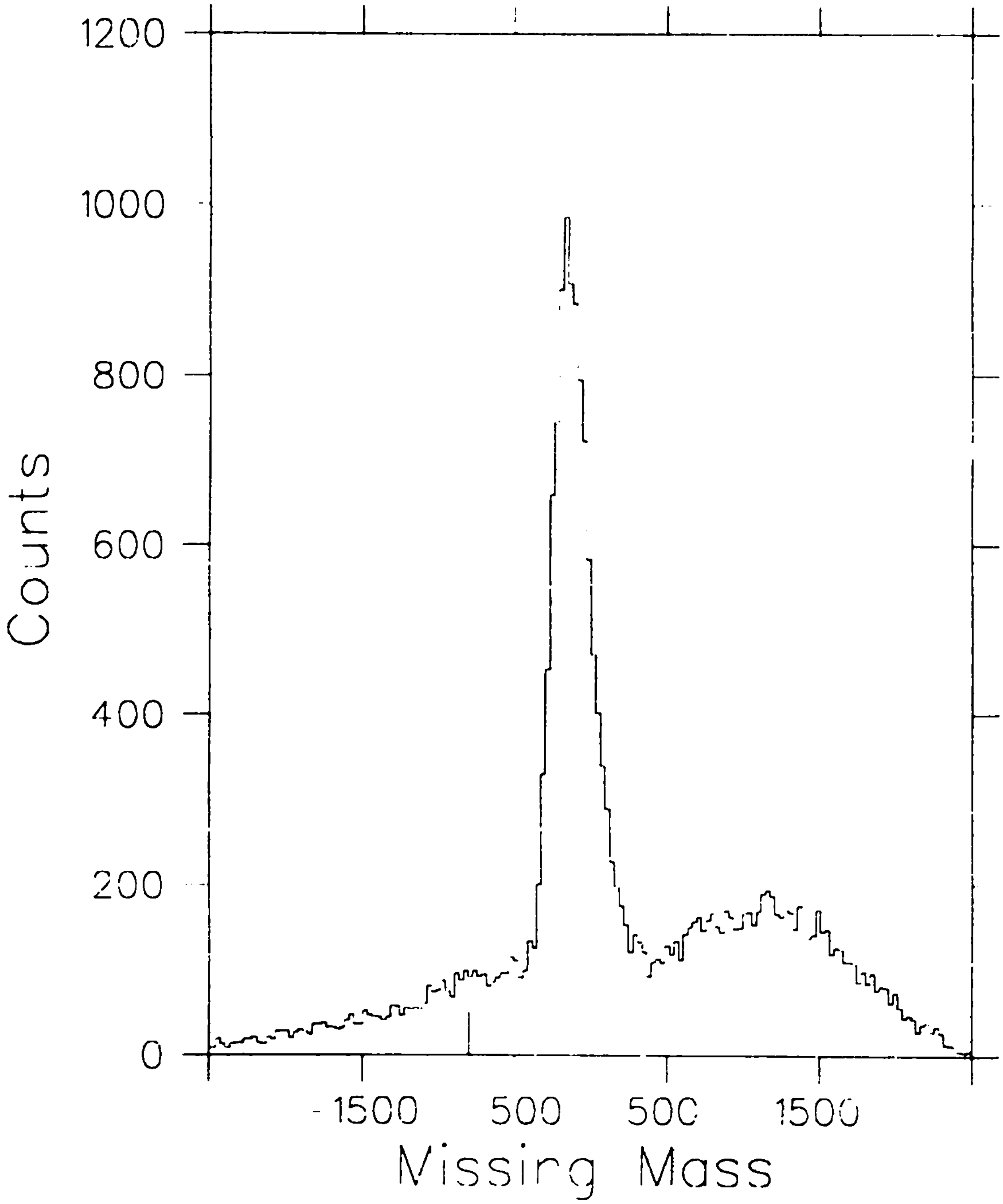

Figure 2.2: Spectrum for π^+T at 120°. The mark to the left of the elastic peak is where muons that came from the forward decay of elastically-scattered pions should show up. The units are 100 bins *per* MeV, *e. g.* 500 = 5 MeV excitation.

background level of any of the points. The region to the left of the peak between −12 MeV and −4 MeV, which would contain most of the elastic muon counts on that side, has 2282 counts, with a statistical uncertainty of $\sqrt{2282} = 48$ counts. The pion peak has 8400 counts, so the muon peak should have 5% of this, 420 counts, or approximately 9 times the uncertainty quoted, or 18% of the counts in this region. Thus we might expect to be able to see the muon peak in this case, but it is not obvious in Fig. 2.2. The slight bump could be easily accounted for by statistics. For other runs with lower peak to background ratios, the muon peak will be harder to see.

Two methods of removing background counts are discussed in Sec.3.6. The first involves scaling a foreground and a background run to each other using the region to the left of the elastic peak, (the 'supra-elastic' region). There are 3387 counts in the region to the left of the elastic peak in Fig. 2.2, with an uncertainty of $\sqrt{3387} = 58$. The number estimated for the muon peak, 420, is significantly larger than this uncertainty and so the muon peak could have a non-negligible effect in scaling for this low background point. The other method discussed is drawing a straight line under the pion peak. The line passes through the end of the tail of the pion peak on each side. Since there is little or no overlap between the pion and muon peaks, the presence of the muon peak is not important for this method.

Finally, there is the question of the breakup counts that are seen in the muon spectrum. These counts come from pions that were scattered in a reaction where the target nucleus broke up. The counts start about 5 MeV to the right of the elastic peak in missing mass, which means that muons due to this process will underlay the pion peak. For the 120° scattering shown in the figure, the ratio of pion counts in an 8 MeV-wide slice of the break-up region to the number in the pion peak is 0.1%, after background subtraction. In keeping with the previous estimates, 5% of this number, or 0.005% of the pion peak area will be the added background under the pion peak due to break-up pions which decayed into muons, which is negligible.

A muon rejector has been installed at EPICS to remove this background [Mor85]. It consists of a series of six layers of alternating thin plastic scintillator paddles and graphite absorbers, followed by a final scintillator, that begins after the rear chambers (see Fig. 2.1). The scintillators are designated $S_4 \cdots S_9$; numbers $S_1 \cdots S_3$ are the trigger scintillators in the main spectrometer (see Fig. 2.1).

Since muons have a greater range than pions of the same momentum, and since pions are easily removed by strong interaction scattering with the absorber nuclei, while muons are not, a thickness of absorber can be added that will remove most of the pions and few of the muons. Then, any particle that passes the absorber and is detected by the scintillator is assumed to be a muon. The graphite slabs are wedge shaped with the thickest part being in the positive x direction (perpendicular to the scattering plane and downward, at the target), so that the higher momentum particles that have the largest radii in the dipoles will go through proportionally more absorber. Aluminum sheets can be added before the first absorber to fine tune the ranging effect. A program called ALUM takes the central spectrometer momentum as an input and calculates both the thickness of aluminum to use for the fine tuning, and the scintillator to use as the detector.

For example, a pion scattered elastically from T at 160° in the laboratory has momentum 233.5 MeV/c. For this value ALUM calculates that $2\frac{1}{4}$ inches of aluminum should be added, and that S_4 should be used as the detector to identify muons. Tests at LAMPF [Mor85] have shown that when properly used, the system correctly identifies around 96% of the muons that would otherwise be classified as pions, and that only 2% of the pions were misidentified as muons.

However, there was a mistake in calculating the scattering angle during this experiment (see section 2.4). The angle was always smaller than planned, and this means that the scattered momentum was actually higher than was thought. Since this erroneous (high) momentum was used as the input to ALUM, too little aluminum was used in each case, so that extra pions made it though the absorber and were counted as muons. Figure 2.3 shows two spectra. The first is missing mass for scattering at 120° and energy 180 MeV. The muon rejector is not used. The second plot shows the counts seen by the muon rejector, that is, the counts that are left out of the analysis if the muon rejector is used. There is a peak that is visible in this spectrum as well, made up principally of pions that were misclassified. The peak contains about 1000 counts, while the peak in the un-corrected spectrum contains about 8500. So, approximately 12% of the pions have been rejected.

During the experiment, the muon rejector was mis-set more than once, *e. g.* at 180 MeV and 120 [illegible] the log book shows $2\frac{5}{16}$ inches of aluminum used for the π^+ runs, and $2\frac{1}{4}$ inches used [illegible] π^- runs; the later is the correct value. The difference in the ratio calculated [illegible] and without the muon rejector was smaller than the statistical errors for this point, and some variation would certainly be expected because of the changes in counting statistics described in the previous paragraph.

Finally, the muon rejector could not be used for the 142-MeV point because the muon and pion ranges are too close to each other, so pions and muons can not be separated.

In conclusion, decay muons can in principle be seen in the pion spectrum, to the left of the peak. Their numbers are such that they could affect background subtractions based on scaling foreground and background runs to each other in that region. The effect should decrease as the signal-to-noise ratio in the pion spectrum decreases; for this experiment, that means as the scattering angle increases. Background removal by means of approximating the background with a straight line though the tails of the elastic peak will not be affected by the muon peaks because of the separation of the muon and pion peaks in missing mass. In runs where incorrect amounts of aluminum were used to adjust the muon and pion ranges in the rejector, or where the too-low energy of the scattered particles

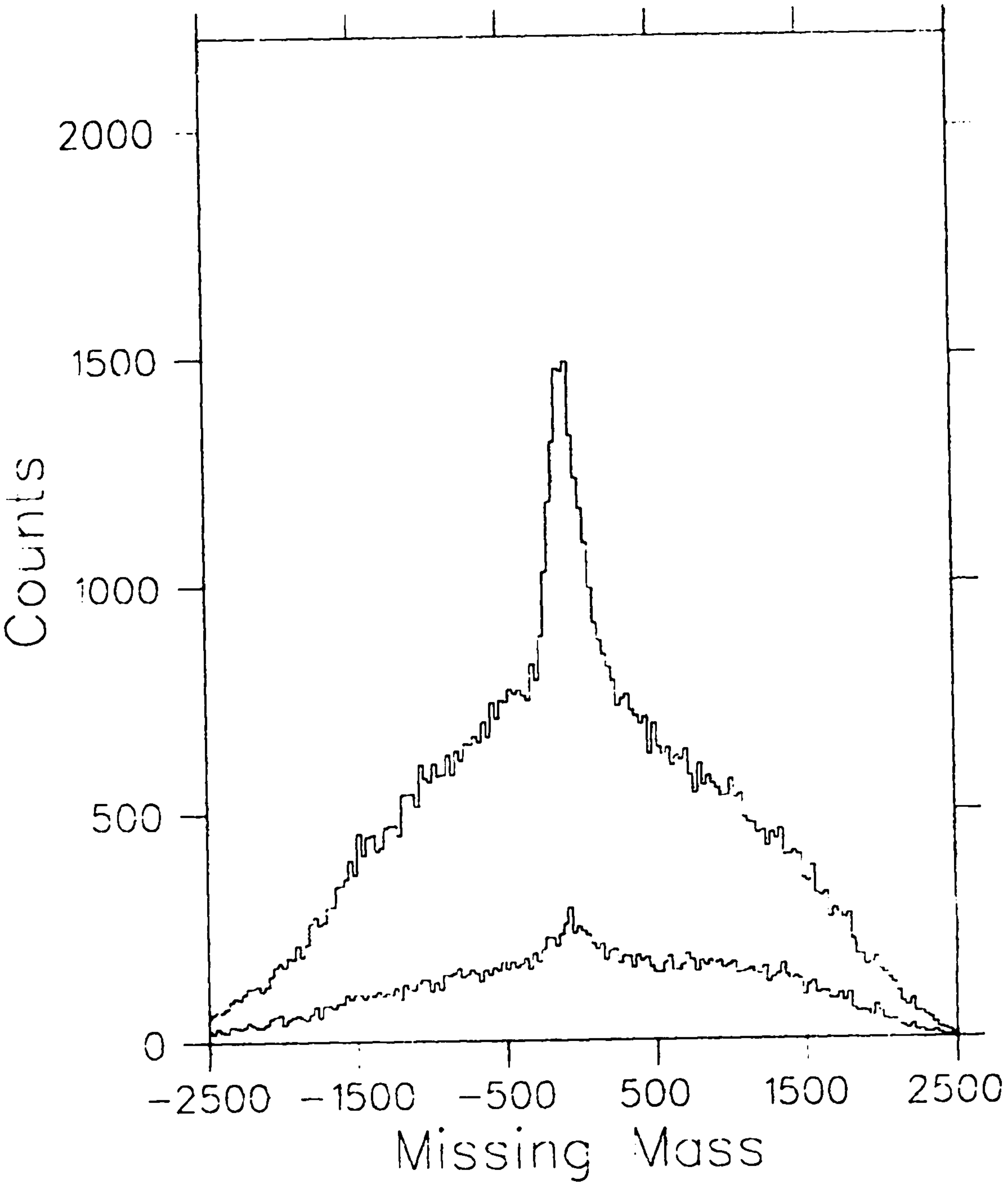

Figure 2.3: Two spectra for the same run, pion scattering from T at 180 MeV, 160°. The lower spectrum is the 'rejected' counts, that is, the ones tagged by the muon rejector. The peak in the lower spectrum has 10% of the counts in the peak in the upper spectrum.

means that the muons cannot be separated from the pions, the muon rejector should not be used.

2.4 EURYDICE

It is necessary to add an extra dipole magnet at the scattering chamber to reach scattering angles greater than 110°. This magnet is called EURYDICE [Bur86], and it can be run at either polarity and at field values in excess of 15 kG. The magnet poles are one meter in diameter, and the pole gap is 25 cm. EURYDICE is placed so that its field is perpendicular to the scattering plane, and the scattering target is at the magnet pole's center. Incoming and outgoing charged particles are bent by the magnetic field so that particles scattered into the backward hemisphere can be seen by the spectrometer, which is at more forward angles.

The standard EPICS pivot is moved downstream 52 cm from its normal position, and the spectrometer is moved back along its pivot arm 30 cm; both adjustments are to accommodate the size of the magnet and scattering chamber. The scattering chamber is built into the space between the magnet poles, and the spectrometer couples to this chamber, which has thin mylar windows where the main beam enters and exits. If the windows are over stressed, they can rupture when the chamber is pumped down; this happened once during the experiments, but no damage was done to the targets or devices in the chamber. When the spectrometer is rotated, the magnet rotates as well, so the same part of the magnet is always facing the spectrometer. The incident beam pipe is covered with a Kapton window that faces the mylar window on the scattering chamber, so the incoming beam must traverse these two windows and a small air gap.

Figure 2.4 shows a schematic view of EURYDICE, looking down at the scattering plane. The beam enters from the left and is bent towards the target, which is at the magnet's center. Most of the beam continues on through the target, through a mylar window opposite the target, and out into the experimental area. One of the beam monitors was an ion chamber (the use of this beam monitor is what distinguishes *norm1* among the normalization factors) which was placed just beyond the window to intercept the beam. The scattered particles are bent to the right as they exit, and the spectrometer is placed so that, when the proper field is used, the scattered particle travels along a path parallel to the spectrometer axis once it leaves the field. Note that this is always the *same* path: the field is selected so that particles of a given momentum have the radius necessary to follow that path. Since the magnet turns with the spectrometer, this means that particles entering the spectrometer always travel through the same part of the magnet, regardless of kinematics and scattering angle. This is advantageous because then all of the particle trajectories suffer the same distortions due to field irregularities, making the acceptance more constant from point to point and from target to target.

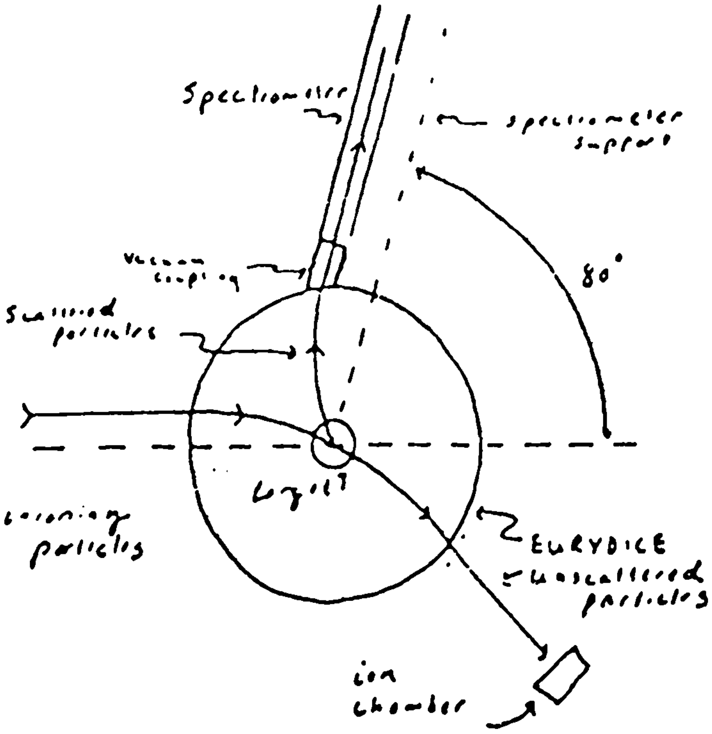

Figure 2.4: EURYDICE in place. Beam enters from the left, and the spectrometer is shown at a floor angle of 80°.

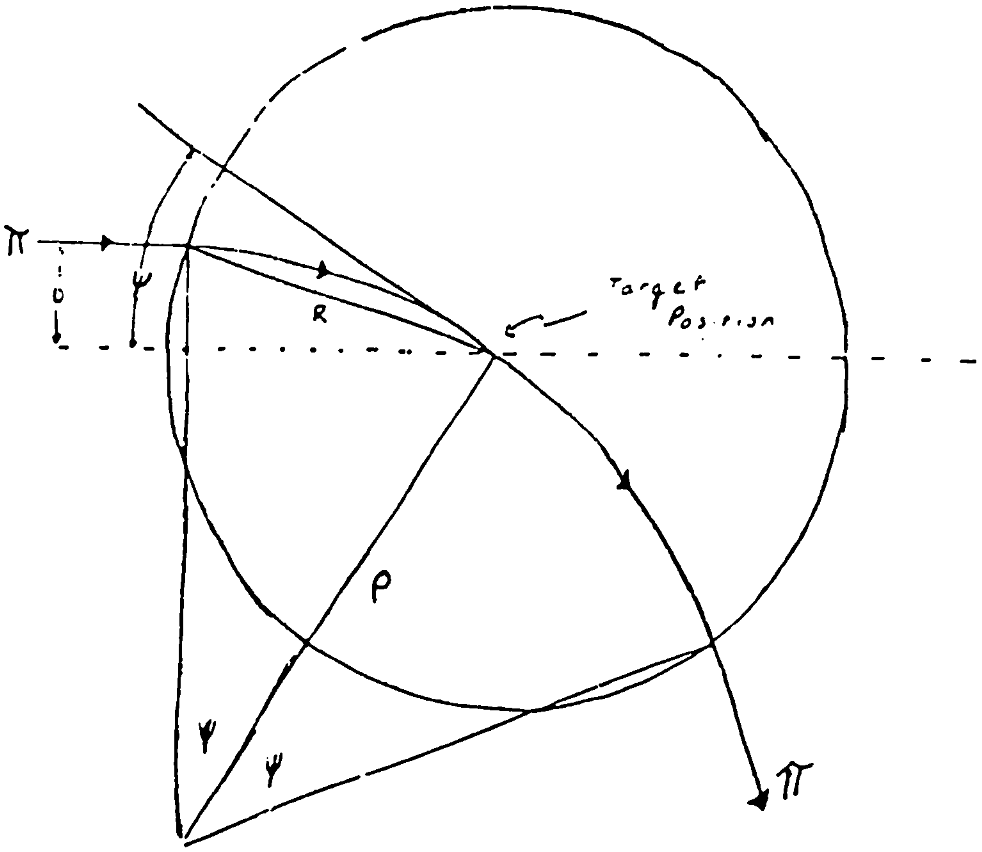

Figure 2.5: EURYDICE geometry for an incoming particle, figure from [Bur86].

The scattering geometry is most easily described in two parts. The scattered particle has less momentum than the incoming particle, but other than that, all of the geometrical factors have the same relationship before and after scattering. Figure 2.5 shows the geometry for an incoming particle. Several parameters can be defined here:

D — the distance that the magnet's center is offset from the incoming beam,

Ψ — the bend angle of the incoming beam — note that this angle is repeated several places by simple geometry,

ρ — the radius of curvature of the incoming beam,

R — the effective radius of the magnetic field as seen by the incoming beam.

Two relationships can be derived from this geometry

$$\begin{aligned} D &= R^2/2\rho \text{ and} \\ \sin(\Psi/2) &= R/2\rho. \end{aligned}$$

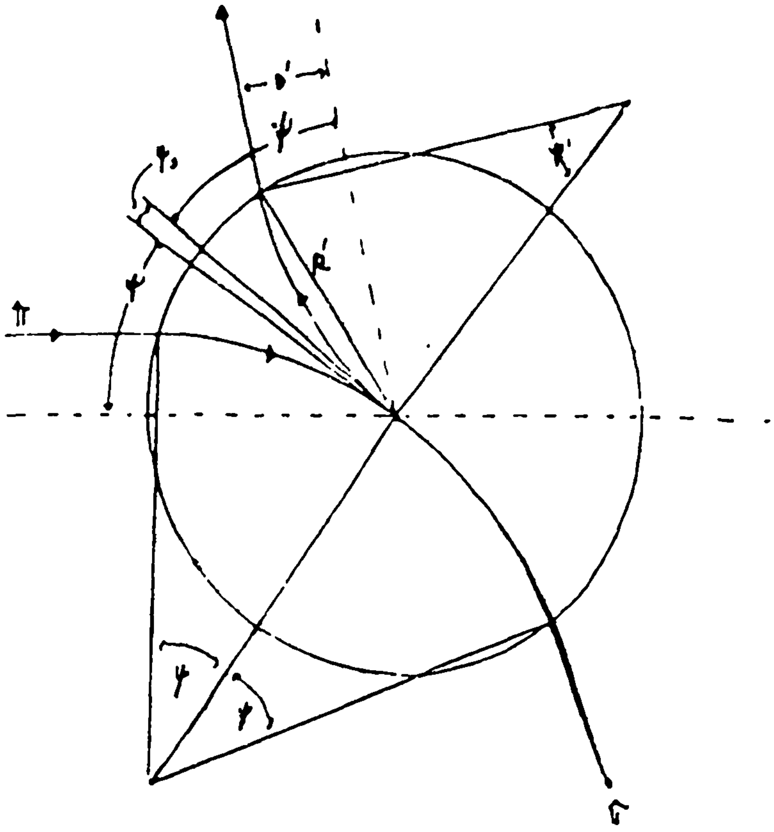

Figure 2.6: Complete scattering geometry for EURYDICE, figure from [Bur86]

The outgoing particle has the same relationships (imagine that the particles are reversed, the outgoing particle now incoming). The variables are denoted with primes. Figure 2.6 shows the complete geometry. D' and ρ' are *fixed* values — the particle always travels outward along the path shown, and the spectrometer position and magnet field are adjusted to make this so. Once the magnetic field is known, for a given scattering angle and momentum, the incoming parameters are all determined. The field and the incoming momentum give $\rho = p/0.29979B$, and the relation given earlier determines D from these values. The scattering angle is given by

$$\theta_S = \pi - \Psi_S$$

and the floor angle for the spectrometer is

$$\theta_F = \pi - (\Psi + \Psi' + \Psi_S) = \theta_S - (\Psi + \Psi').$$

The floor angle referred to here is relative to the EPICS pivot. However, since the pivot moves in order to set the offset, the true floor angle must be derived from a knowledge of θ_F and the offset needed to match the incoming beam. The spectrometer is lined up with radii drawn on the floor, and the offset D is set using a pneumatic jack that slides the spectrometer on its pivot. A computer program called EURYD86 takes the target, momentum and scattering angle as inputs, and gives the proper values to use for the offset and the floor angle, as well as the EURYDICE field.

The field was monitored with an NMR probe in the scattering chamber. The probe is read out in the counting house, where a remote control panel allows the power supply to be set while watching the probe readout. The power supply is controlled by setting a control voltage, which is proportional to the magnet power supply current, and therefore proportional to the magnetic field, when the magnet is being used on the linear part of its hysteresis curve. If the magnet is cycled correctly, down to zero and then to maximum voltage for the power supply, to avoid mistakes due to hysteresis variations, the field can be reset to the same value by coming back to the same control voltage. During some of the runs the probe was not working and it was necessary to set the field by the control voltage values only. There were no obvious effects due to this necessity, and no corrections have been made.

2.4.1 Target Geometry and Ray Tracing

An incorrect Eurydice field map was used during these experiments. The field map is used to calculate the effective field radii given the incident and scattered pion momenta. These radii in turn allow the calculation of the proper EPICS angle and offset. Since these calculations were made with erroneous inputs, EPICS viewed a different angle at each position than planned (usually about 5° less). The momentum of the scattered pion at this new angle was not what the spectrometer was tuned for. For example, the first point was nominally 120°. A 180-MeV pion scattered at 120° from T has momentum 244.9 MeV/c. The true scattering angle was [illegible]14°, so the momentum of the scattered pion was actually 247.2 MeV/c. The difference is is $(247.2 - 244.9)/244.9 \sim 0.9\%$. As the momentum acceptance is greater than ±7%, this does not mean that the particles could not be analyzed. However, this difference does affect the performance of the muon rejector. Since the actual scattered pions have more momentum than was used to calculate the proper aluminum thickness to use for the ranging adjustment in the rejector, not all of the pions will be ranged out, and some will be tagged as muons. The magnitude of this pion loss is discussed in Sec.2.3.4.

Another problem with this use of EPICS was the thick targets. The EPICS software assumes all scattering comes from a thin target at the center of the scattering chamber in the z direction; call this the midplane. There is no way to get z-position information for the scattering events, and so thick targets like ours introduce an ambiguity that cannot be resolved.

The Problem with Thick Targets

Consider a particle that is scattered from the far side of a thick target (the edge nearest the spectrometer), and is scattered at a steep angle in the vertical plane. The nominal magnification by the quadrupoles for an event in the midplane of the target is -1 in x. A track that starts at a certain x position where the event did not take place in the midplane will appear to have come from a different x position in the mid plane. This value of X_{target} will be used in the δ calculation, and so missing mass will be affected. Likewise, the particle appears to have the values of Y_{front} and ϕ_{front} that correspond to a different Y_{target} location. Y_{front} and θ_{front} are both part of the δ calculation, and so they also affect the missing-mass value.

The angular acceptance of the spectrometer is nominally ±5° in the vertical plane, so assuming a one-inch offset of the scattering plane from the midplane, and a 3° scattering angle in the x-z plane, the value of X_{front} measured will differ from the true value by $\sin(3°) \times 2.54$ cm $= .13$cm.

A particle scattered in the horizontal plane looks like it came from the midplane, offset by the sine of half of 180° minus the scattering angle, times the size of the z displacement of the target. In this example, for 120° scattering, the y position error is $\sin((180 - 120)/2) \times 2.54 = 1.27$ cm.

The first-order EPICS optical description of the quadrupoles is

$$Y_{front} = 0.2\phi_{target} \tag{2.1}$$

$$\phi_{front} = -5Y_{target} \tag{2.2}$$

and the lowest-order terms in the δ calibration for this experiment are

$$\delta = -0.2X_{front} + 0.23X_{rear} + 0.0028Y_{front} + 0.00094\phi_{front} + \cdots$$

This can be rewritten with the optics equations as

$$\delta = -0.2X_{front} + 0.23X_{rear} + 0.0028 \times .2\phi_{target} - 5 \times 0.00094Y_{target} + \cdots$$

for the case where the x-z and y-z plane effects are complementary. The change in δ due to the target extension will be $-0.2\times0.13 - 5\times0.00094\times1.27 = -0.0086$. This corresponds to $0.0086 \times 245 = 2.1$ MeV/c shift in momentum for 180 MeV pions scattered from T at 120°. The 0.13 cm change in X_{target} corresponds to a change in δ of .00013; for 287 MeV/c incident pions this is .037 MeV/c. The change in momentum is therefore dominated by $\delta_{spectrometer}$. The 2.1 MeV/c change corresponds to an 1.9 MeV energy shift.

As a quick check on the magnitude of this effect, two sets of vertical rod targets were inserted during the calibration of EPICS with another bending magnet, which was being used for a double-charge-exchange experiment. The geometry of this set-up is not the same, because the particles only traverse this magnet after scattering, not before *and* after as with EURYDICE, but the trace-back problem is similar. The first set of rods was the standard set, but the second had the rods offset along the z-direction 1.5 inches. There was not time to take much data, but on-line results showed that the missing mass peak for carbon was shifted about $\frac{1}{2}$ MeV to the left for the extended target. That is, the spectrometer attributed more energy to the scattered particles. Since the rods give precise Y_{target} values, we can see how the extension in the z direction affects this quantity. The rods' traced-back positions were shifted to the left about 1 cm.

Because all of these effects happen for scattering centers upstream *and* downstream of the midplane, the result is a decrease in resolution on the order of 1 or 2 MeV. Since the experimental targets were cylindrical, they did not present a uniform thickness to the beam; the loss of resolution will be the greatest near the target's center in the x-z plane. We always use the entire elastic peak when comparing runs of different kinematics, *e. g. T and D* , so the results should not be affected in those cases. For ratio calculations we always use the same region in runs with the same kinematics, both in missing mass and Y_{target} . The effects discussed here will be the same in all cases where the kinematics are the same. The peaks should have the same shapes, and so comparison of the same part of the peak in each case is legitimate. This is discussed further in Chap 3.

Ray Tracing

During analysis, we want to eliminate as many background counts as possible. Since the principle background is the aluminum side walls of the target canisters, we need to get a good idea of what represents the walls and what is the gas volume in Y_{target} , the projection of the target in the y - z plane. Figure 2.7 shows how scattering from the central part of the target is distributed in the horizontal plane. The upper plot is a missing-mass plot from π^+T scattering at 116°. The elastic peak is clearly visible. If we put a gate around this peak the counts in the gate include all of the particles scattered elastically by the gas, and some background. In the region of missing mass covered by the spectrometer, most of the gas scattering is in the elastic peak, and so the gate identifies most of the particles that were scattered in the gas. If the background is not too large, then the gas scattering is a large fraction of the gated particles, and using this gate to histogram Y_{target} gives an idea of the shape of the gas volume in Y_{target} .

The bottom plot shows Y_{target} with and without this cut. The large 'wings' on the sides are eliminated by the cut, which shows that they are not predominantly from the gas, and so must come from the target walls.

In order to see exactly where the particles are going, a ray-trace program was written for EURYDICE, using a simple two-step Eulerian integration. Field values from a recent field mapping of EURYDICE were scaled to provide the correct field for a given kinematics. Figure 2.8 shows the results for a flat target, as is usually used at EPICS. The incoming rays define the horizontal size of the actual EPICS beam. The spectrometer is shown as it would normally be positioned. The spectrometer has a good overlap with the scattered particles.

The next step was to use a cylindrical target, as was used in the experiment, (see sect. 2.5). The target size was chosen as the size of the gas volume. Particles enter in the beam and proceed to the target. Outside of the target (and not shown) is a region of aluminum that contributes energy loss; scattering from

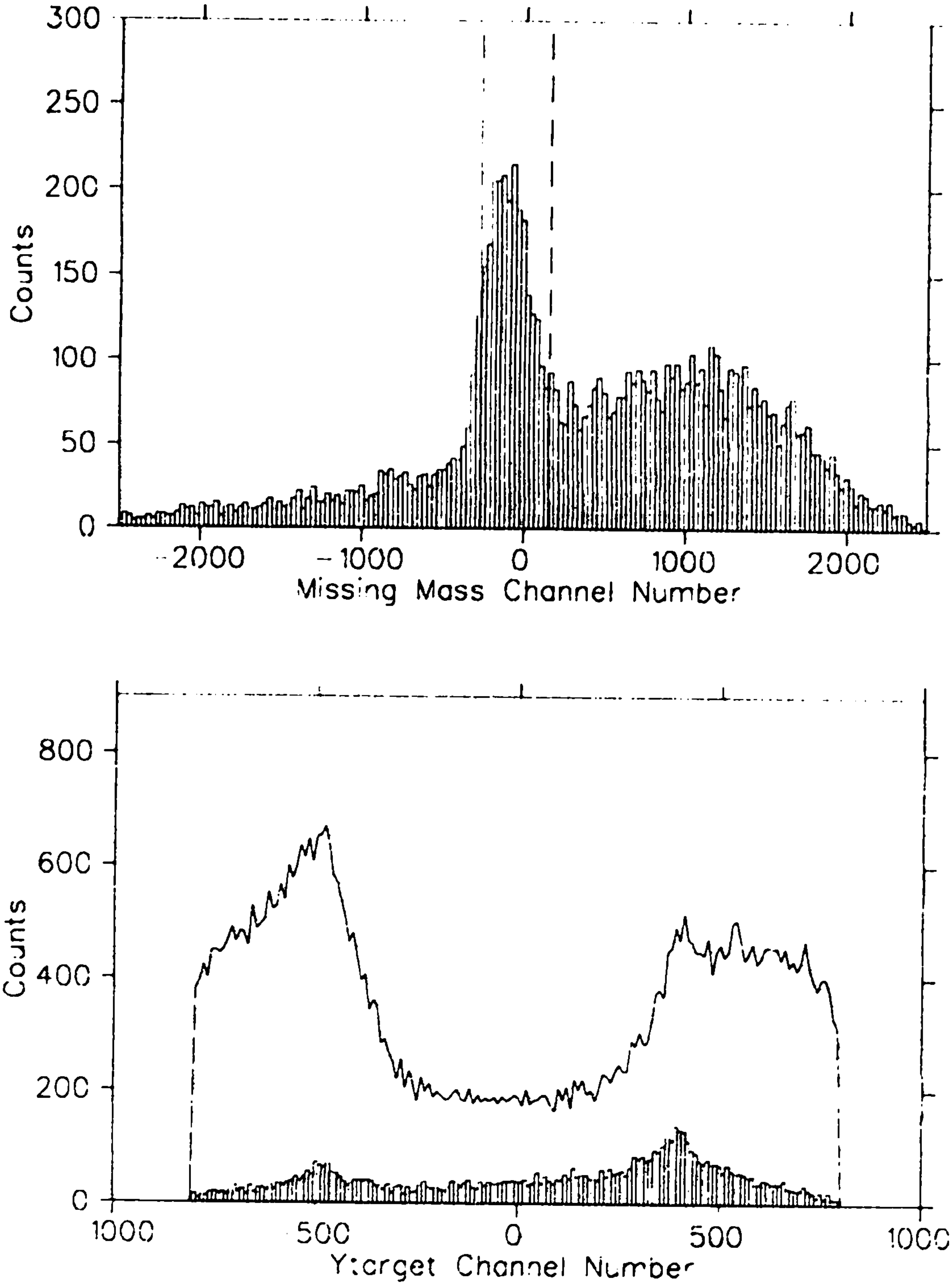

Figure 2.7: *Top:* Missing mass for T scattering for $\theta_{lab} = 116^{\circ}$. The dashed lines show the cuts that were used to define the elastic peak. *Bottom:* Y_{target} for the same run, and Y_{target} with the missing-mass peak cut from the upper histogram. The 'gas volume' evidently extends over all Y_{target} .

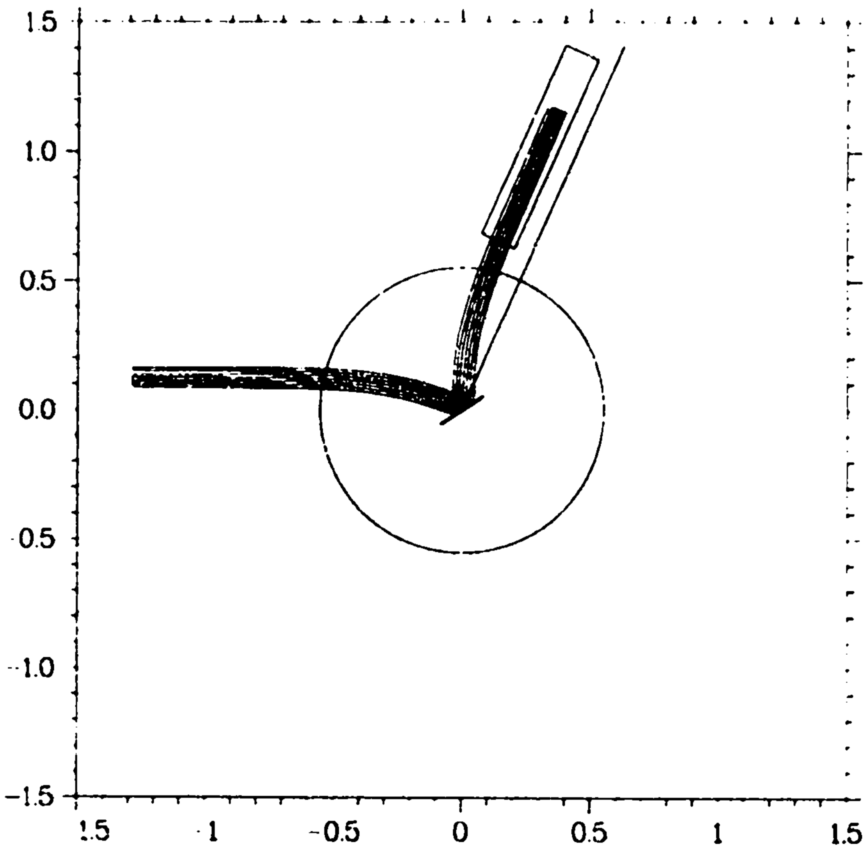

Figure 2.8: Scattering from a traditional EPICS target, at 116°. Output from the trace program. The pion beam is shown entering at left, scattering at 116°from a thin target, and entering the spectrometer. The rays are within the spectrometer accepta: as defined by the tracing program (see text). The units are meters.

the aluminum walls is not considered. In the gas, the particles lose energy due to interactions with electrons, both before and after scattering. The target is built up out of small pieces. Each piece is evaluated separately and the number of scattered events that are accepted by the spectrometer is recorded, where acceptance is defined as being within ±1° of the central ray for the spectrometer, and physically within the bounds of the front y-direction chamber, at the position of the first dipole.

Figure 2.9 shows the full ϕ_{front} histogram from replayed runs compared with calculated y distribution of the rays from the trace program for four points. ϕ_{front} is measured at the front chambers, and is linearly correlated with the y position at the spectrometer entrance. The units of the ϕ_{front} histograms have been scaled to the units from the trace program. The spectrometer's center is at 25, and the edges at 0 and 50. The scale is expanded on each side for clarity. Because the linear relationship between y position and ϕ_{front} is only first order, we do not expect a perfect match. Furthermore the replayed histograms include the scattering from the target walls, which is discussed below.

The overlap for the four points is fair. At forward angles there are no big problems, but at large angles the centroids of the trace results and the replay histogram do not line up. However, a wide cut on the histogram, centered on the histogram centroid, will include most of the gas volume, as represented by the trace output.

Figure 2.10 shows the result of scattering from each target piece. Many of the incoming rays are not accepted. This figure shows how the scattering at a single angle is spread out by the cylindrical target; scattering at many angles will be accepted from at least part of the target.

Figures 2.11 , 2.12 , 2.13 , and 2.14 show scattering from the front part of the target, that is , the part first intercepted by the beam, which will be called the 'nearside', and from the opposite or 'farside', wall. At more-forward angles, rays coming from the two walls are well separated. As the scattering angle increases, the separation is lost, and the rays cover the entire spectrometer entrance. Although the runs were done with gas scattering only, the aluminum walls of the can will have the same correlation with scattering angle, and their density means that the walls contribute a large part of the scattering. Evidently the target wings are images of the walls; the left wing is the nearside wall, the right wing the farside wall. Figure 2.15 shows how the scattering angle was distributed. The scattering angle is correlated with the z-direction displacement of the scattering center.

Figure 2.16 shows histograms of acceptance fraction as a function of angle, for the full target gas volumes, at four representative points. The acceptance covers between 10° and 14°, increasing with scattering angle, as opposed to the 3° normally quoted for EPICS. The number called the acceptance here is the ratio of the number of rays that were scattered and accepted to the total number input. Since this experiment is done with the same size beam for each target piece, many rays do not intercept the target at all. So, this acceptance is the

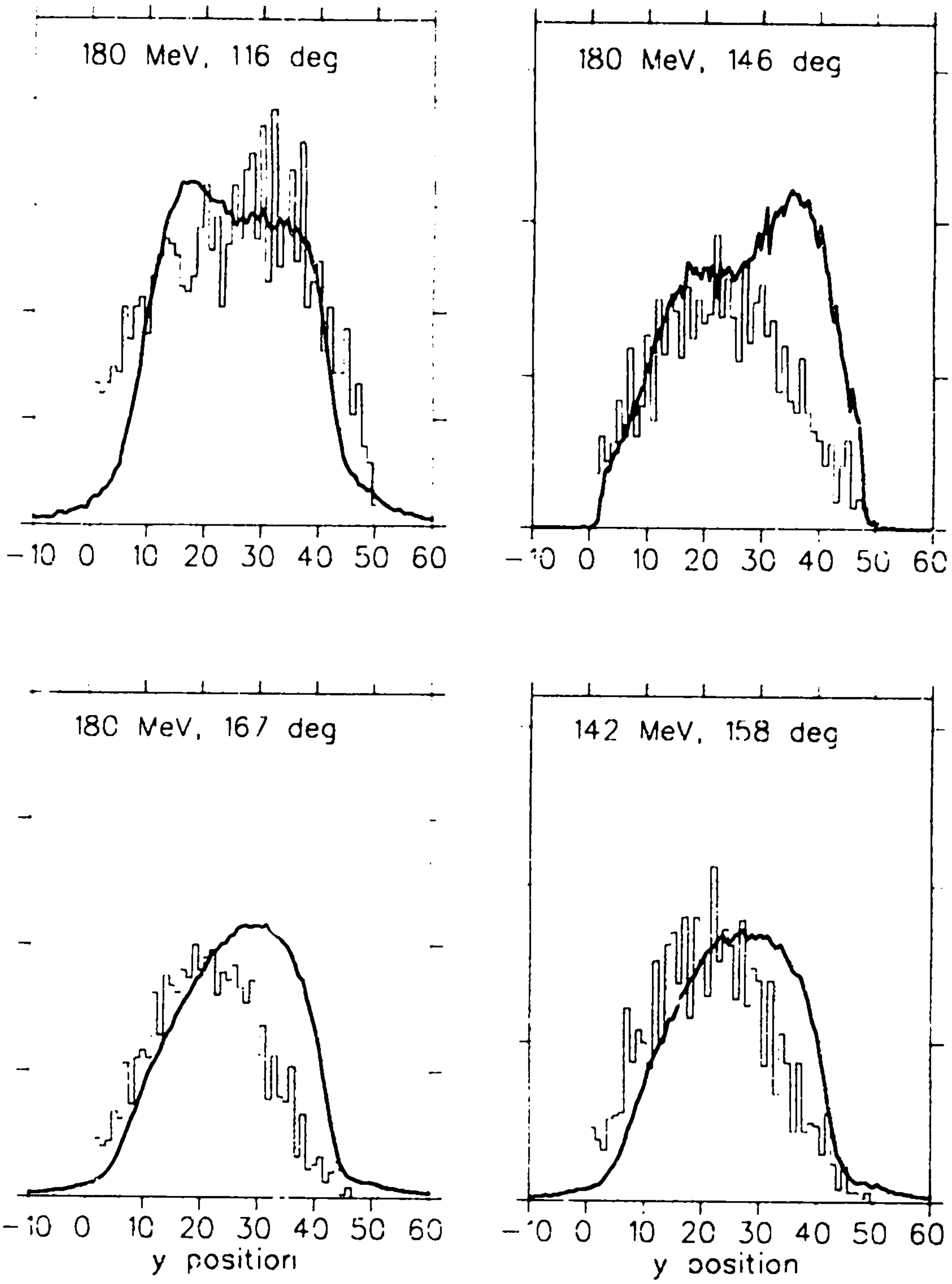

Figure 2.9: A comparison of the ray tracing output (thin lines) and ϕ_{front} as calculated by the spectrometer (thick lines).

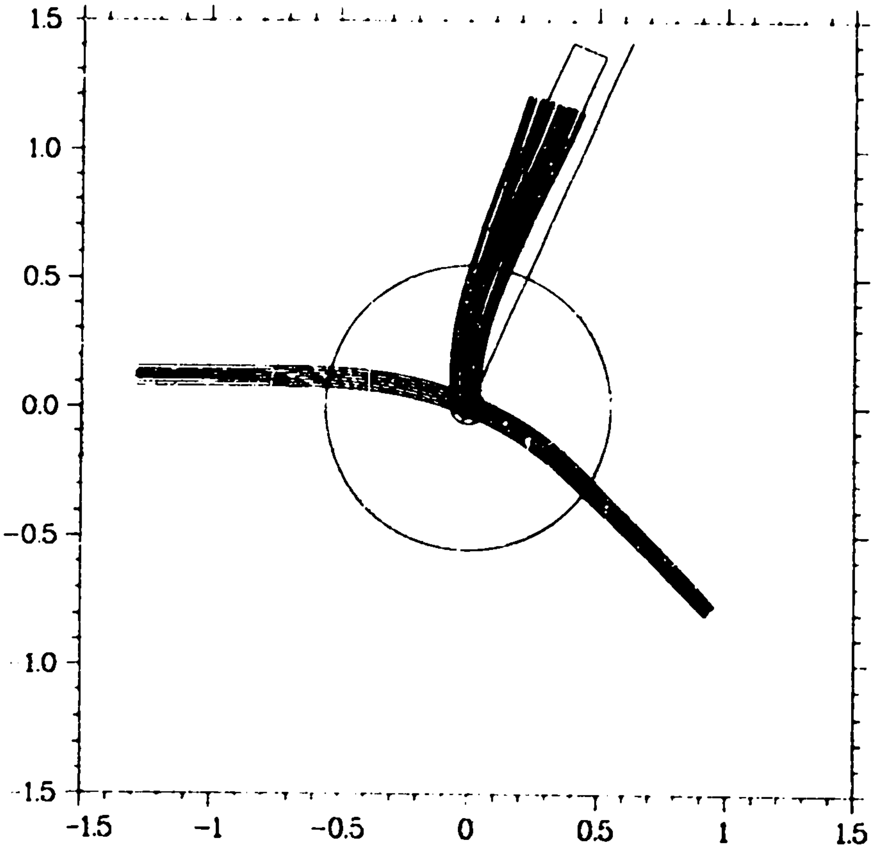

Figure 2.10: Scattering from a cylindrical target at 116°. The figure shows the unscattered beam continuing through the chamber, and the scattered rays, many of which are not within the spectrometer's acceptance. Note that the beam is narrower than the target. The units are meters.

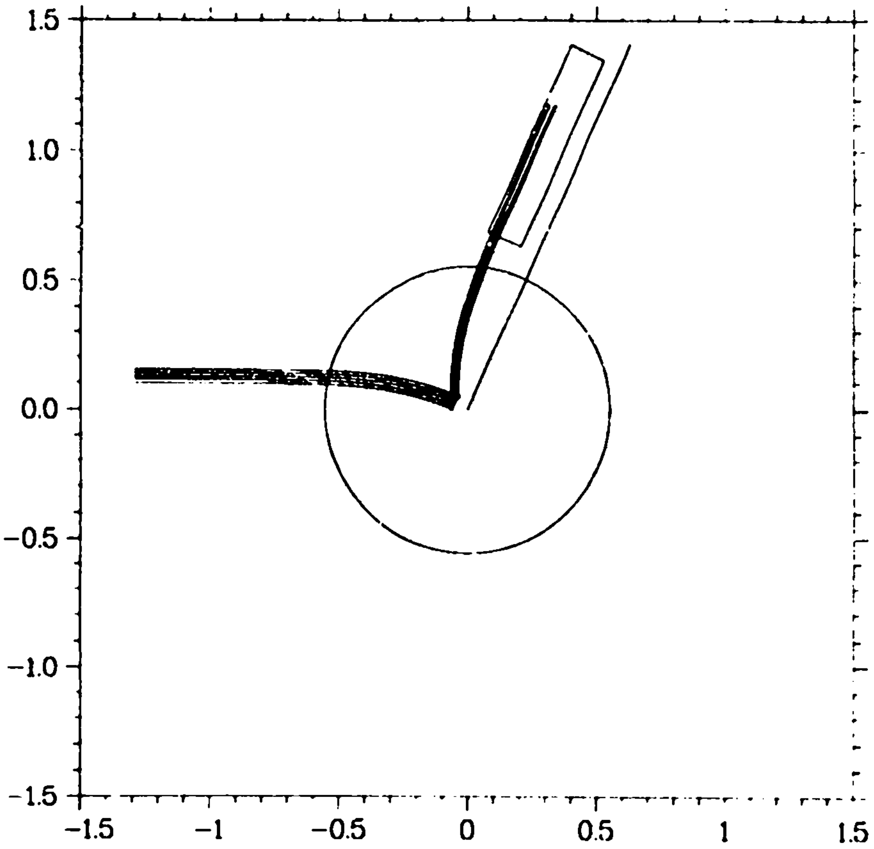

Figure 2.11: Scattering from the outermost ring of the target, near side only at 120°, for several scattering angles. The accepted rays are on one side of the acceptance.

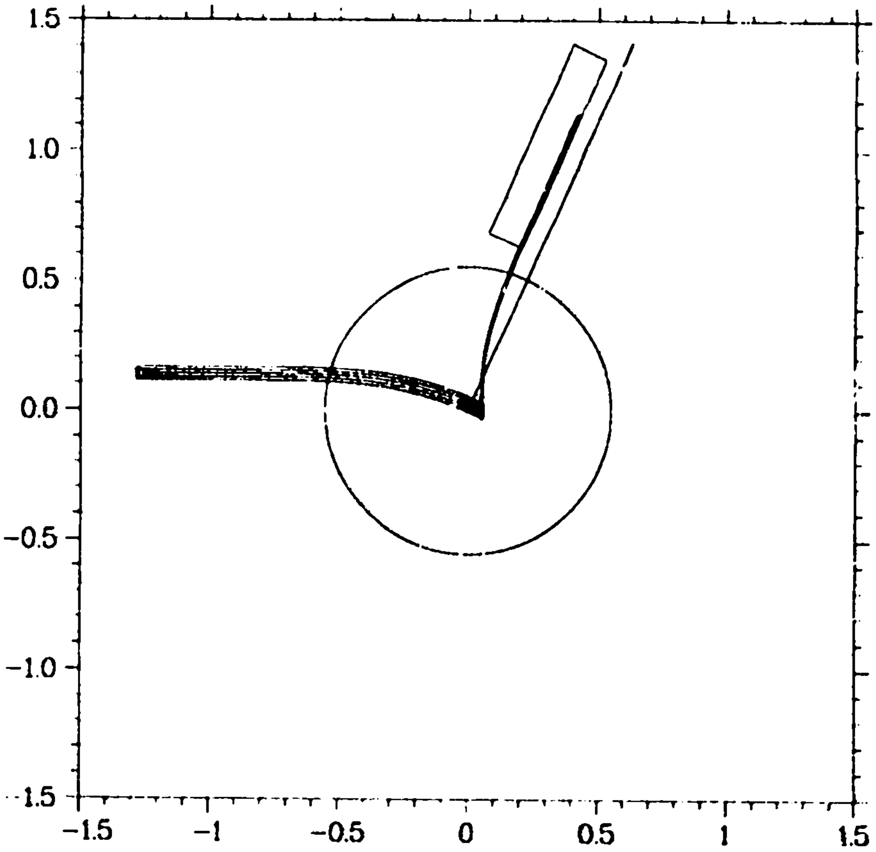

Figure 2.12: scattering from the outermost ring of the target, far side only at 120°, for several scattering angles. All of the accepted rays are to one side of the acceptance.

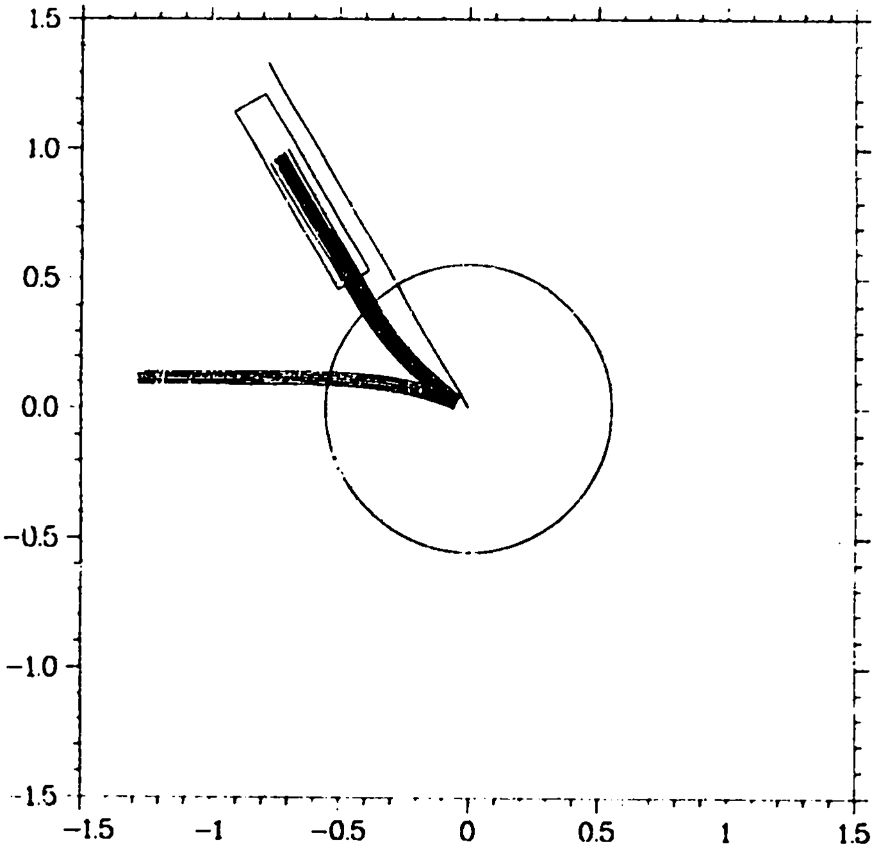

Figure 2.13: Scattering from the outermost ring of the target, near side only at 167°, for several scattering angles. The acceptance is good, the rays cover the center part of the acceptance.

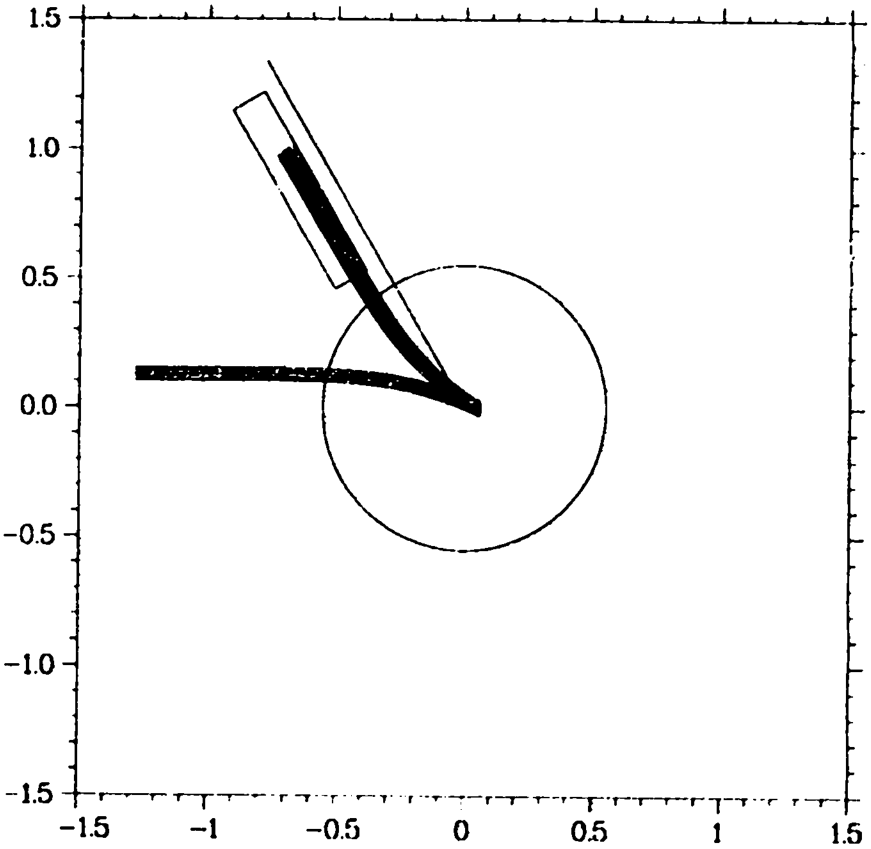

Figure 2.14: Scattering from the outermost ring of the target, far side only at 167°, for several scattering angles. The rays are spread out over half of the acceptance.

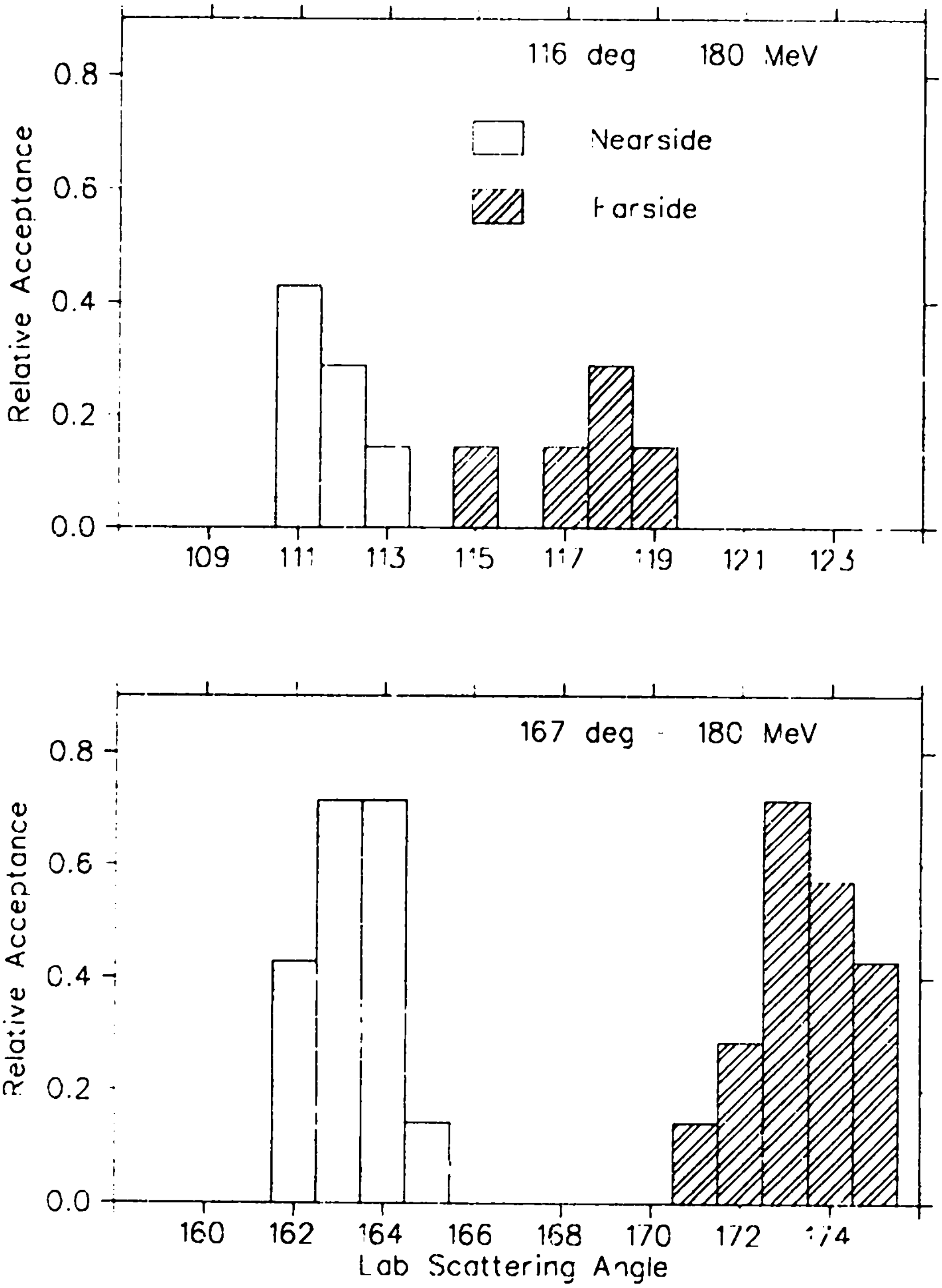

Figure 2.15: **Scattering from the nearside and farside walls, for two different setups. The scattering covers 10° in the top histogram, and 15° in the lower.**

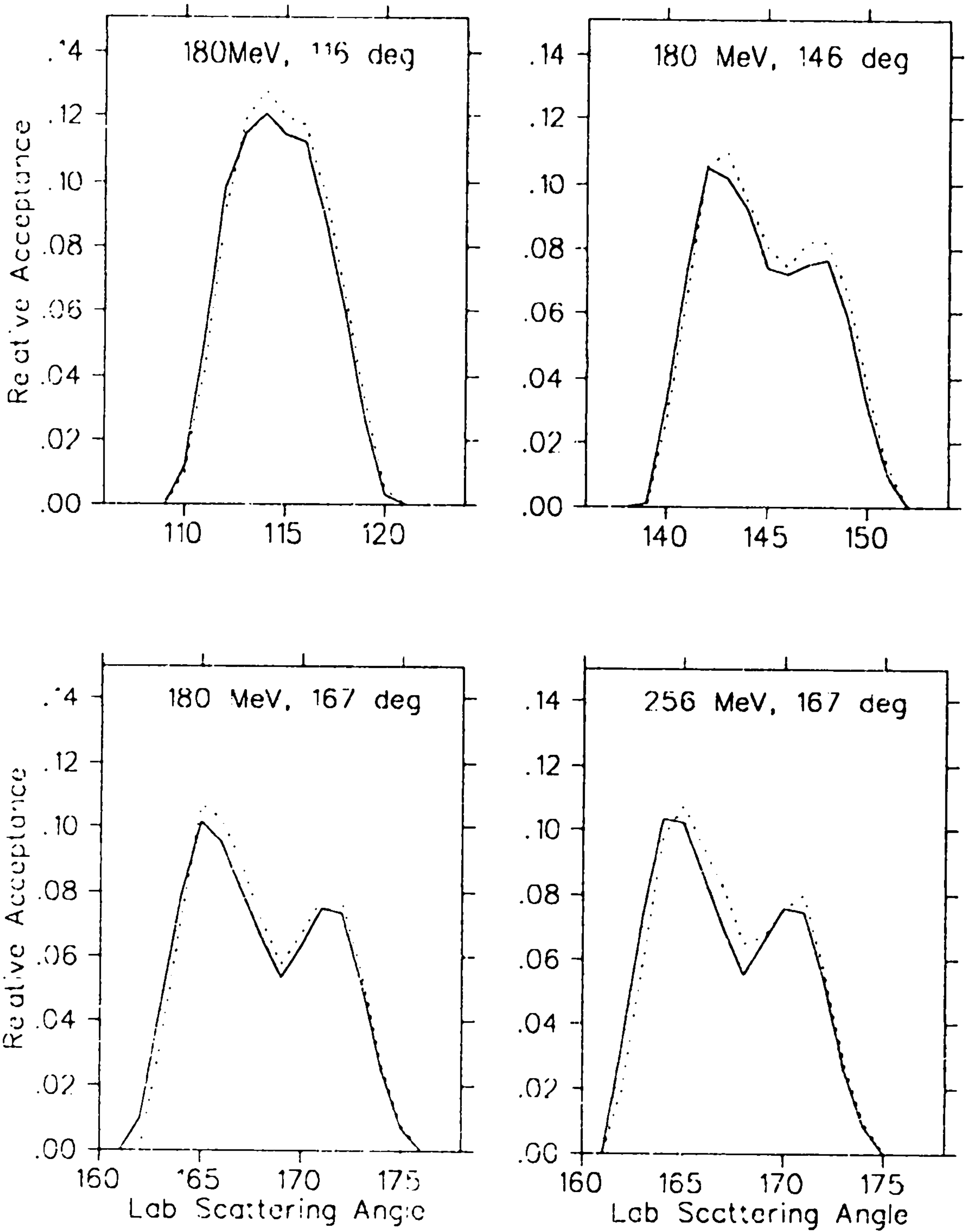

Figure 2.16: **Relative angular acceptance, output from the ray tracing program. The solid lines are the T results, the dotted lines the D results.**

Energy(MeV)	Angle(deg)	T/D	Ang. Accep.(deg)
180.0	114.0	0.97	10
	125.0	0.97	10
	135.0	0.98	12
	145.0	0.96	12
	155.0	0.97	13
	168.0	0.98	12
142.0	158.0	0.98	13
	162.0	0.99	14
220.0	168.0	0.99	13
256.0	168.0	1.00	13

Table 2.1: **Results of the ray tracing. The first column is the incident pion energy, the second the correct laboratory scattering angle. The ratio of T to D shown in the third column , is the acceptance correction. Cross sections will be divided by this number. The final column is the angular acceptance for that point.**

relative fraction of the beam that is scattered into the acceptance at a given setup from a given target. to be compared to another setup and target. The 'wings' on the sides correspond to those in the previous figure. This winged shape appears in all of the histograms related to the horizontal projection; they are due to scattering from the nearside and farside walls. as discussed in this section. The wings are very apparent in the replayed runs, because these runs include scattering from the aluminum target walls.

It is important to know how this shape changes with angle and energy. In particular, a comparison of two targets, T and D will show whether an acceptance correction will be needed when D yields are used for normalization (see Chap 3). The acceptance is about 3% higher for D at 120°: the difference decreases with angle. The reason for this is not clear; however we should note that the acceptance is a complicated function of the target shape, the kinematical broadening, and the angular acceptance.

The final angles quoted for each point will be taken from Fig. 2.16, using the center of the distribution to the nearest degree. Table 2.1 lists the relative acceptance for each angle and energy covered in the back-angle experiments, for T and D, the angular acceptance at each point, and the angle used to quote the final results. The cross sections will be corrected by dividing by the relative acceptance, listed in the column 'T/D'.

2.4.2 Backscatter

At certain scattering angles, it is possible for particles that continued on through the target to scatter outside the chamber and still make it back up the spectrometer; call these particles 'backscatter'. The backscatter is an extra angle-dependent background. Although the effect should be the same, for example, in π^+T and $\pi^{+3}He$, there is a difference in the π^+ and π^- backscatter that is proportional to the difference in the π^+ and π^-cross sections of whatever material is in the backscatter source. Figure 2.17 shows the path of a backscattered particle. The particle goes in along the beam path, goes on through the target and out of the scattering chamber, and then scatters. It has to scatter so that it has the correct angle and momentum to follow the path of a particle scattered from the target. Several angles and distances are shown in the figure; primes refer to the outgoing particles. Ψ and Ψ' are the incoming and outgoing bend angles. α and α' are equal to one half of these angles. R is the effective field radius, Z is the distance from the edge of the field to the backscatter point. The arrow heads in the figure are on actual particle tracks, showing the directions before and after the scatter. The experimental scattering target would sit at the magnet center.

The construction and the following argument are due to [AmUp].

From the figure we can write down two relations,

$$\frac{\sin(180-\alpha)}{R+Z} = \frac{\sin(\alpha)}{R+Z} = \frac{\sin(\beta)}{R+Z}$$

and

$$\frac{\sin(180-\alpha')}{R+Z} = \frac{\sin(\alpha')}{R+Z} = \frac{\sin(\beta')}{R+Z}$$

Figure 2.18 is a simplified drawing of the same situation. The chords and tangents from the upper part of the previous figure have been extended. From this figure, we can see that

$$\Psi_S = 2(\alpha+\alpha') - (\beta+\beta').$$

We can combine these to get

$$\theta_S = \pi - (\Psi+\Psi') + \arcsin\left(\frac{R}{R+Z}\sin(\Psi/2)\right) + \arcsin\left(\frac{R}{R+Z}\sin(\Psi'/2)\right), \quad (2.3)$$

using the previously derived result, $\theta_S = \pi - \Psi_S$.

A very important backscatter source is the large Plexiglass window that is used on the downstream side of the scattering chamber to protect the thin vacuum window from damage. This window is very close to the edge of the magnet, and so in the formula above $R \gg Z$. If we let $Z = 0$, and $\Psi \sim \Psi' \sim 30°$ we find $\theta_s \sim 150°$ for the region of prominent backscatter. Because of the inaccuracy in the scattering angle that will be discussed later, and the imprecise nature of the calculation (for instance $Z \neq 0$, the Plexiglass does not conform to the chamber shape, and so the value of Z varies over the cross section of the beam, and the

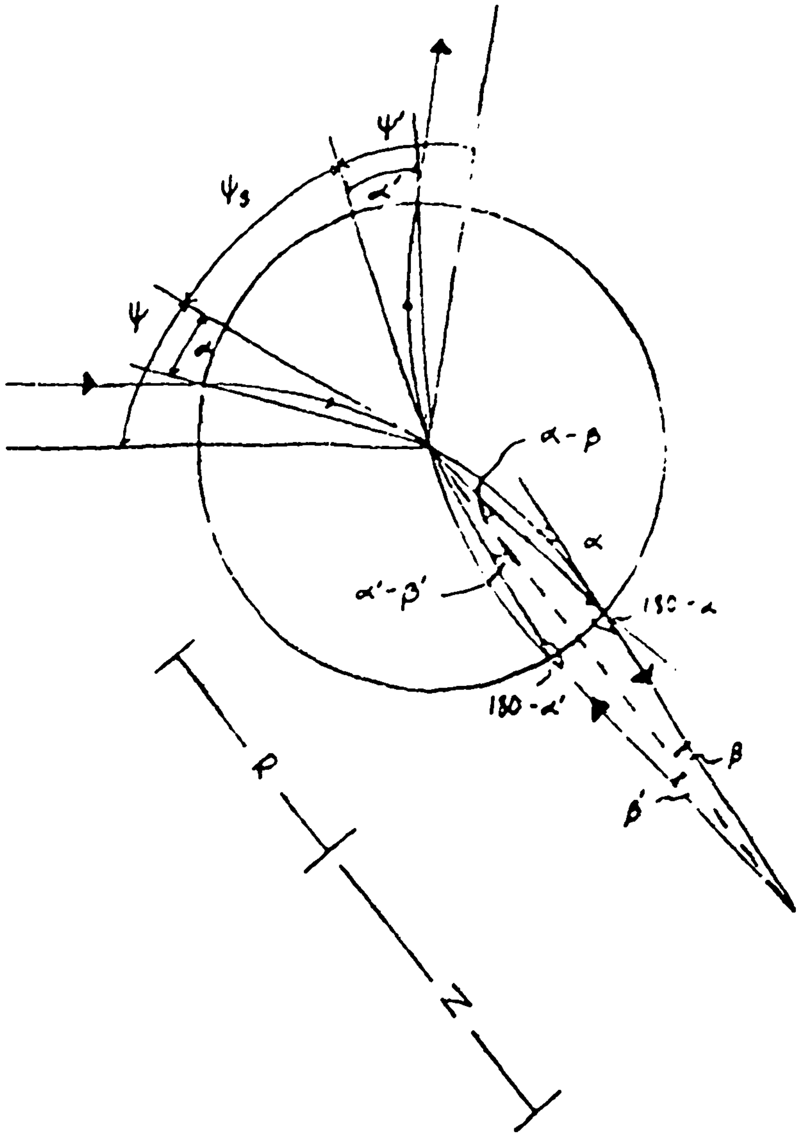

Figure 2.17: An overhead schematic of EURYDICE showing how the backscatter enters the spectrometer. Back-scattered particles must have the proper angle and momentum to follow the same radius as the particles scattered from the target.

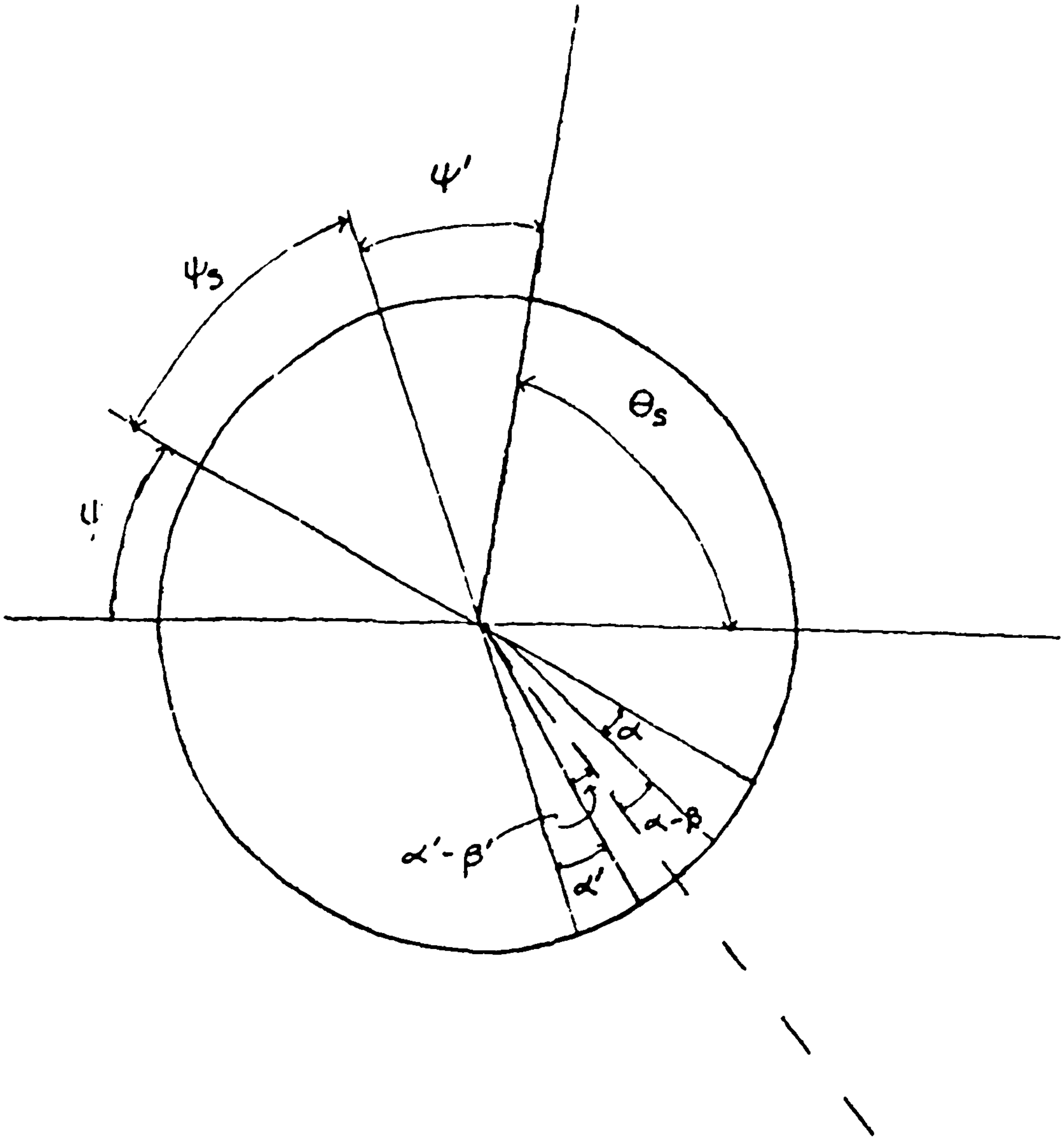

Figure 2.18: EURYDICE backscatter diagram, showing the important relationships between the derived angles.

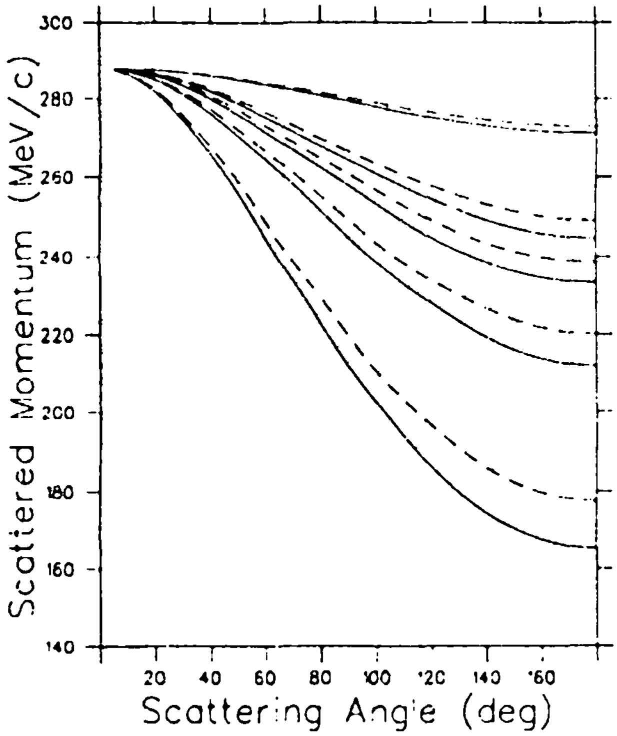

Figure 2.19: The momentum of scattered particles from various targets, from top: Carbon, ^{4}He, Tritium, Deuterium, Hydrogen. The channel is tuned for 180 MeV pions, which corresponds to ~ 287.5 MeV/c momentum for all particles. Towards back angles, there is a very wide divergence in the scattered momentum. Electrons (dashed lines) and pions (solid lines) have about the same scattering kinematics.

bending angles were only approximate), we can only say that backscatter could be a problem around 140° — 160°, and special care should be taken in this range to look for possible backscatter effects.

Up until now, geometry was assumed to be the only consideration for this problem. In fact, it must be shown that at 150° the materials in the back-scatter targets can provide scattered particles with momenta matching the momentum for which the spectrometer is tuned. From the previous two figures, we can see that the backscattering will have to take place close to 180°. Figure 2.19 shows the elastic scattering kinematics for several targets, for electrons and pions when the channel is tuned for 287.5 MeV/c (180 MeV pions). If the spectrometer is tuned for 150° scattering of 180 MeV pions (about 220 MeV/c for D, and about 240 MeV/c for T), then elastic scattering from carbon at back angles (around 280 MeV/c) produces particles that have too much momentum to make it onto the spectrometer's focal plane (the momentum acceptance of +/ − 7% would accept 216 — 262 MeV/c). However, inelastic carbon scattering should provide a fairly continuous spectrum, starting at 20 — 30 MeV in the carbon spectrum. If the backscatter target is a plastic or metal, then most of the constituents should be as heavy or heavier than carbon, and described by similar kinematics. Therefore, we can expect a smooth addition to the background, whose magnitude may depend on the beam polarity. The exception is Hydrogen, but the figure shows that there is not a reasonable overlap with Hydrogen elastic scattering and the various scattering targets at back angles. For the few runs where H is the target, this is not the case of course. Backscatter could be a problem here.

2.5 The Targets

The five identical target cells have been described in [Pil91]. Each is an aluminum cylinder with inside diameter 12.7 cm, inside height 18.6 cm, and wall thickness 0.18 cm. The cylinder was flanged at each end so that stainless steel end caps could be bolted to it. The targets were equipped with a screw hole in the center of each end cap, allowing them to be screwed together in a column, as they were in experiments 905 and 1032. In our case, we put a screw in one end to use in aligning the target on the turntable (see below). The targets were filled to around 3 MPa with T, ^{3}He, D and H. An empty target that had been used for background subtraction in previous experiments was not used in these. All of the targets except the T had not been emptied since the previous experiments, and so did not need filling. The T target was filled by the WX-5 group at LANL with approximately 18 gm (around 180 kCi) of gas. The target contents were evaluated by weighing, this process and the reduction of that data are described in Sec. 3.2

2.6 The Target Changer

A target changer was built at The George Washington University Physics Department for the back-angle experiments. The targets were placed on a turntable in the scattering chamber so that they could be changed in and out of the beam without removing the vacuum window. The turntable consisted of an aluminum disk with a groove around its edge. A plastic belt fit into the groove and fed through a similar groove on a small disk that was part of a gear-driven driver. The driving axis extended through a port in the scattering chamber to a handle that allowed manual adjustment of the target position. The turntable bottom was hollowed out to receive a slightly smaller brass disk that was screwed to the chamber's floor; a teflon pad sat on the brass disk, and the turntable sat on that. Turning the driving handle outside the scattering chamber turned the driving wheel, which moved the belt, which turned the turn table.

The plastic belt was a poor choice because it slipped too easily in the grooves in the plate and driving wheel. We had to make several scattering chamber entries to lubricate the brass disk with dry molybdenum, to polish the in-contact surfaces of the plates, and eventually to repair the driving mechanism when too much torque warped the driving shaft.

2.7 Safety Measures

Tritium is a radioactive isotope of H that decays to ^{3}He with the emission of a beta particle with average energy 6 keV, and a half-life of 12.6 years. Such a low-energy beta is primarily a threat only if the T is ingested. Only 5% of inhaled H or T is retained by the body; the most likely way to get an uptake is to breathe combustion products after a T fire, or to ingest tritiated water, which can also be produced in fires. Our targets were tested extensively, and it was very unlikely that they could be ruptured. The most likely possibility was a leak that vented T slowly to the atmosphere. This would be a minor safety hazard, but a significant regulatory violation. Therefore, extensive safety precautions were required both for transporting and using the T target. The air in the experimental area and the exhaust from the scattering chamber vacuum pumps were monitored constantly. Evacuation alarms were installed for the entire pion-experimental area, and canisters of breathing air and positive-pressure anti-contamination suits were on hand; in case of an emergency an experimenter could don the suit to investigate the experimental area, aid injured people, etc.

A detailed description of the safety measures can be found in the Standard Operating Procedure written for the experiment [Gre89].

2.8 Summary

This unorthodox use of the EPICS system worked reasonably well. The very large angular acceptance of the experiment, which was due to the combination of bending magnet and extended targets, means that the data has been smoothed somewhat over angles. The horizontal acceptance shape is explained by the use of an extended target — the 'wings' on the Y_{target} histograms are from the near and far edges of the target. Pions scattered from the gas volume illuminate the entire spectrometer entrance uniformly.

The muon rejector will not be used in this analysis because of its mis-setting, due to error and to incorrect magnetic field maps for EURYDICE. However, this will not be a serious lack, because the number of muons in the spectrum are negligible in the region of the pion elastic-scattering peak, and the muon peaks are located such that the tails of the pion peaks are unambiguously defined.

Chapter 3

Data Reduction

3.1 General Analysis Features

3.1.1 Yields and Cross Sections

The quantity measured at EPICS is called a *scattering yield*. This is the number of scattered events counted at a given angle and energy, scaled by a factor that is inversely proportional to the amount of incident beam and to the spectrometer efficiency. A beam monitor is a device that interacts with the proton beam or the pion beam, and produces a signal that is proportional to the current. Since this number is proportional to the number of particles that has passed, the yields are relative quantities, not absolute ones. If ϵ is the calculated efficiency for a run, and if n is the number of counts registered by the beam monitor, then the measured yield is

$$yield = \frac{number\ of\ events\ counted}{\epsilon \times n}. \tag{3.1}$$

A differential cross section is the number of particles scattered into a differential solid angle, divided by the incoming beam intensity and by the number of target particles per unit area. That is, it is the fraction of the incoming intensity scattered into the solid angle *per* target particle. Since we measure yields, we need a way to convert yields to cross sections. We do this by measuring the yield for a target with a known cross section. The yield and cross section for this standard target are called the normalization yield and normalization cross section. This gives us a factor *cross section/yield* that we can multiply our other yields by. So,

$$\frac{d\sigma}{d\Omega}(target) = yield(target)\left(\frac{d\sigma(normalization\ target)/d\Omega}{yield(normalization\ target)}\right)\left(\frac{D_N}{D_T}\right), \tag{3.2}$$

where D_N and D_T are the density of scattering centers in the normalization and experimental targets, respectively.

3.1.2 Ratios

The main purpose of the experiment was to determine the values of several *scattering ratios*. These are ratios of differential cross sections, designed to emphasize different parts of the π-nucleus interaction, (see Sec. 1.3). Their definitions are

$$\begin{aligned} r_1 &= d\sigma(\pi^+\mathrm{T})/d\sigma(\pi^{-3}\mathrm{He}) \ , \\ r_2 &= d\sigma(\pi^-\mathrm{T})/d\sigma(\pi^{+3}\mathrm{He}) \ , \\ \rho^+ &= d\sigma(\pi^+\mathrm{T})/d\sigma(\pi^{+3}\mathrm{He}) \ , \ \mathit{and} \\ \rho^- &= d\sigma(\pi^-\mathrm{T})/d\sigma(\pi^{-3}\mathrm{He}) \ . \end{aligned}$$

The first two or the second two in the above set can be multiplied to form the Superratio R,

$$R = r_1 \times r_2 = \rho^+ \times \rho^- \ .$$

There are several experimental advantages to measuring ratios. Consider ρ^+, for instance

$$\rho^+ = \frac{yield(\pi^+\mathrm{T})d\sigma(\pi^+\ NT)/yield(\pi^+\ NT)}{yield(\pi^{+3}\mathrm{He})d\sigma(\pi^+\ NT)/yield(\pi^+\ NT)}\frac{1}{gasfac},$$

where NT stands for normalization target, and $gasfac$ is the target-density ratio, which is discussed in Sec. 3.2. We use the same kinematics for the yields of π^+T and π^{+3}He because they have approximately the same masses, so their solid angles are the same, and no corrections are necessary. Furthermore, since we are using a π^+ beam for both targets, the normalization yield term is the same in the numerator and denominator, so it can be canceled, as can the normalization cross section. We are left with

$$\rho^+ = yield(\pi^+\mathrm{T})/yield(\pi^{+3}\mathrm{He})/gasfac,$$

and similarly

$$\rho^- = yield(\pi^-\mathrm{T})/yield(\pi^{-3}\mathrm{He})/gasfac.$$

r_1 and r_2 do not cancel so completely, because the beam polarity is not the same in the numerator and the denominator. However, if we assume that the D cross sections are the same for each polarity, then $d\sigma(\pi^+\mathrm{D})$ and $d\sigma(\pi^-\mathrm{D})$ can be cancelled against each other. If this is not the case, then the ratios must be corrected by a factor that is the ratio of the D +/− cross sections. Finally, there is a factor of

$$\rho D \equiv yield(\pi^+\mathrm{D})/yield(\pi^-\mathrm{D})$$

in r_1 and r_2 which must be measured separately (see Sec. 3.6.3).

The definitions become

$$\begin{aligned} r_1 &= \left(\frac{yield(\pi^+\mathrm{T})}{yield(\pi^{-3}\mathrm{He}}\right)\left(\frac{1}{\rho D}\right)\left(\frac{1}{gasfac}\right) \ \mathit{and} \\ r_2 &= \left(\frac{yield(\pi^-\mathrm{T})}{yield(\pi^{+3}\mathrm{He})}\right)\left(\frac{\rho D}{1}\right)\left(\frac{1}{gasfac}\right) . \end{aligned}$$

3.1.3 Normalizations

At EPICS, the two factors in the denominator of Eq. 3.1 , ϵ and n, are calculated by a program called SHT. n is the integrated current from a beam monitor. The ion chamber in the cave, which was discussed in Sec. 2.3 produces an ionization current which is carried over a cable and digitized in the counting house. The quoted accuracy of the digitizer is 0.1%; for a ratio such as R, which is composed of four yields, this would give an added error of $\sqrt{4} \times 0.1\% = 0.2\%$. The very best statistical errors are for some of the ρ^+ values, and are on the order of 2%. Adding 2% and 0.2% in quadrature gives a negligible change; This error will be disregarded from now on.

ϵ in Eq. 3.1 is also computed by SHT. Figure 3.1 shows how one factor in ϵ is derived. The outer boundary represents the θ_{check} and ϕ_{check} space (see Sec. 2.3.3); the concentric circles represent the intersection of the plane with the muon-decay cone. The central square is $\theta_{check} \cap \varphi_{check}$. This is the region of acceptable events. The area with the vertical striping is $\theta_{check} \cap \overline{\phi_{check}}$. This represents all of the particles that passed θ_{check} but not ϕ_{check} . The area with diagonal hatching is the 'muon background' area; that is, the muon density in this area is assumed to be representative of the entire plane. The background area is $\frac{1}{2}$ the area under the vertical hatching. The efficiency in the θ_{check} direction is the number of 'good' pion events divided by the number of pions that passed θ_{check}. This last is the number of events in the vertically-hatched region - $3\times$ the background region - 3 times to include the region under the center. A similar calculation determines the ϕ_{check} efficiency, and the two are multiplied together to get the efficiency,

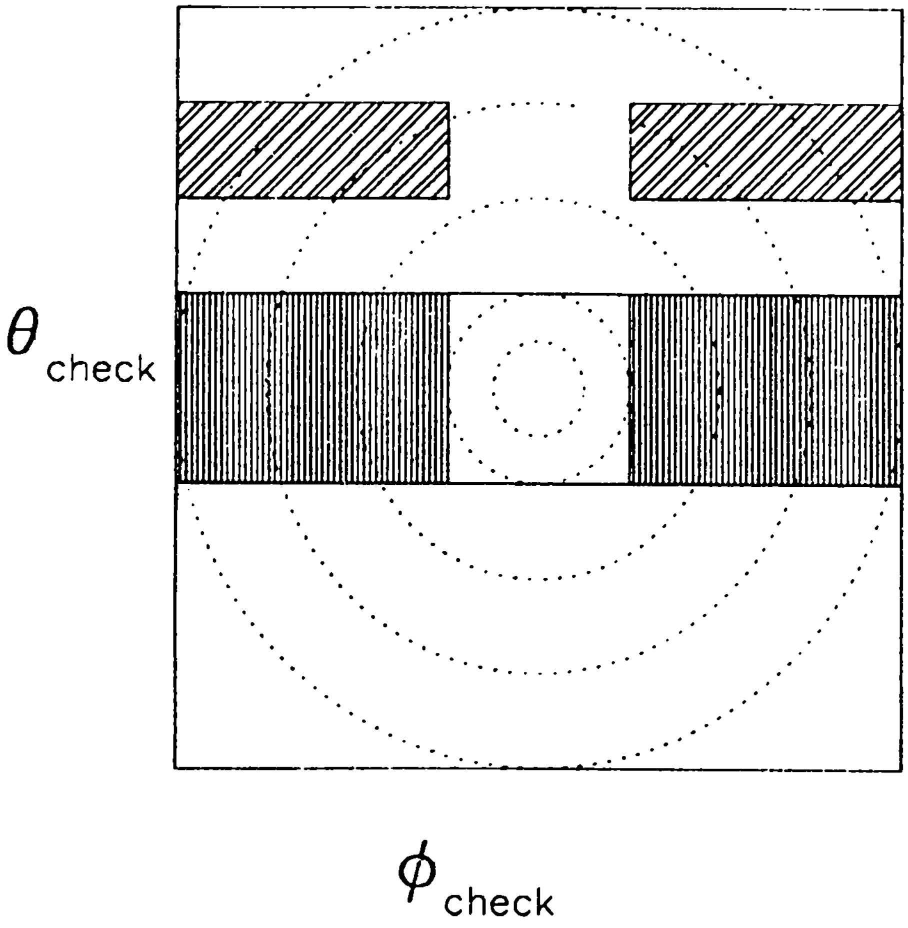

Figure 3.1: Figure to derive the spectrometer efficiency in the ϕ_{check}direction. The circles represent the muon decay cone. The vertical hatching is the region good θ_{check} *and* $\overline{\phi_{check}}$. The diagonal hatching is the 'background region', derived from a specially defined test. The central square covers ±10 mrad.

$$\begin{aligned}\epsilon' &= \left(\frac{\theta_{check} \cap \phi_{check}}{(\theta_{check} \cap \varphi_{check}) + (\theta_{check} \cap \overline{\phi_{check}} - 3 \times \theta_{check}\ background}\right) \\ &\times \left(\frac{\varphi_{check} \cap \theta_{check}}{(\varphi_{check} \cap \theta_{check}) + (\phi_{check} \cap \overline{\theta_{check}} - 3 \times \varphi_{check} background}\right).\end{aligned}$$

Finally, this product is multiplied by the calculated pion survival fraction, since scattered pions with different energies have different flight times up the spectrometer; hence the survival fraction depends on the scattering energy. The final product is ϵ.

SHT produces a number called a norm which is the inverse of $\epsilon \times n$, so the number of counts is multiplied by the norm to get the yield. For this analysis, two beam monitors, the ion chamber and the beam toroid were used; the norms calculated with each are designated *norm1* and *norm2*, respectively. As has been discussed, *norm2* is mostly useful as a check; *norm1* is used for the quoted results.

3.2 Gas Factor

In order to calculate the yields, we need to get a value for *gasfac*, the ratio of densities of scattering centers used for the cross sections and yields. In ρ^+ , for instance, we will need to know

$$gasfac = \frac{\#of\ atoms\ in\ the\ \mathrm{T}\ target\ /unit\ volume}{\#of\ atoms\ in\ ^3\mathrm{He}\ target\ /unit\ volume}, \tag{3.3}$$

that is, the ratio of scattering centers seen by the beam *per* unit area. In this case, we know the weights of the gas volumes very well, so we would like to calculate *gasfac* in terms of these weights. Call w the weight of the gas in the canister. N the number of atoms (that is the number of scattering centers) *per* unit volume. N_A Avagadro's number, the number of molecules in a mole of gas, m the mass of gas in a particular target and m_m the mass of a mole of the gas. Then we can write

$$N = \frac{m \times N_A \times \#atoms/molecule}{m_m \times volume}\ and$$

$$w = mg,$$

where *volume* is the volume of the gas in the container. The number of atoms/molecule is 1 for ^{3}He and 2 for the isotopes of Hydrogen, H, D and T. Inserting this in eq. 3.3 gives

$$gasfac = \frac{2 \times m(\mathrm{T})/m_m(\mathrm{T})/volume(^3\mathrm{He})}{m(^3\mathrm{He})/m_m(^3\mathrm{He})/volume(\mathrm{T})}. \tag{3.4}$$

Similar calculations allow us to get *gasfac* for the various targets with respect to the D target, in order to calculate the cross sections. The accuracy of *gasfac* depends on the accuracy of the weight and volume measurements of the targets.

The targets were weighed using a 50-kg Voland balance, which has a nominal accuracy of better than 0.1gm *per* weighing; each target was weighed several times, and the results averaged. The inside volumes of the targets were measured by the WX-5 group at LANL to within 0.8 cm^3. Previous measurements of these targets at the operating pressure of approximately 3 MPa showed a change in the volume of less than 0.05% [Ber].

Using the volumes of the T and ^{3}He target canisters, we can estimate the fractional change in *gasfac* due to this expansion:

$$\Delta = \left(\frac{2533.7(1+0.0005)}{2525.7}\right) / \left(\frac{2533.7}{2525.7}\right) = 1.0005 \Rightarrow .05\%\ change$$

in order of magnitude; it should be significantly less in fact because the expansions will both be in the same direction, and of approximately the same size. In light of the final *gasfac* error of ~ 0.5% (see below), this effect is ignored.

During earlier experiments [Pil91] , a mass spectrometer was available to evaluate the isotopic purity of the targets, but that was not possible during these experiments. In general, the purity of the targets is expected to better than 99.9% [Mal], that is impurities introduce a 0.14% error (two 0.1% errors in quadrature), at maximum, into the gas ratio, *gasfac*. This number is included in a 0.1% catch-all addition to the *gasfac* error (see below). The T target was assumed to be 100% on the day it was filled, approximately one week before the experiment began.

We can also consider the effect of varying air buoyancy on the weight measurements. We should add the weight of the air that was displaced by the target volume back onto the target weight, but then we must subtract the weight of air that was displaced by the counter weights. These weights are stainless steel, and the volume of air they represent is the weight of the target divided by 7.9 gm/cc, the density of the steel.

The formula for the corrected weight of a canister is

$$W = W_{cell} - D\left(gV_e - \frac{W_{cell}}{D_{ss}}\right) \tag{3.5}$$

where V_e is the cell's external volume, and D_{ss} is the density of stainless steel. D is the density of the air; the air density was corrected according to the local temperature and pressure when the weighing was done.

We are actually interested in the difference in two weighings, namely the full and empty target,

$$W_{gas} = W_{full} - W_{empty}.$$

This gives the weight of the gas in the full target. The 'empty' targets were either pumped down to vacuum, or filled with ^{4}He at atmospheric pressure.

	Tritium	Helium-3	Deuterium
Spring '90	19.00(.11)	9.43(.06)	12.62(.08)
Summer '89	18.99(.11)		
Summer '89	18.91(.11)		
Summer '88		9.45(.02)	12.56(.03)
June '85		9.47	12.56
July '85		9.43	12.56

Table 3.1: Gas weights for the various targets. The two entries for Summer '89 refer to after and before the experiment, respectively. The measurements from 1988 and 1985 are from previous experiments [Ber]. The variations between experiments are of the order of 0.5%, which is an indication of the systematic errors involved.

	T^3He	TD	^3HeD
gasfac	2.012	1.000	.500
error	.014	.007	.004

Table 3.2: Values of *gasfac* and their errors for the current experiment.

Because we are looking at the difference in two large, nearly equal numbers, for instance for one T weighing the full target weighed 8002 gm. and the empty weighed 7983 gm. the accuracy of the various measurements is crucial.

Using the highest density of air present on any weighing day for D in Eq. 3.5, the buoyancy correction for the ^{3}He target, was 0.05 gm. or about $0.05/9.0 = 0.6\%$. We are interested in the ratio of two gas weights, and since the error in the buoyancy correction, is in the same direction for numerator and denominator, we should quote a combined error of $(1/\sqrt{2})(0.6) = 0.4\%$ for the ratios, due to this effect. Other effects such as the error in the target weighing, the impurities in the gasses, and the volume differences in the targets contribute on the order of 0.1%. so an overall error of 0.5% was used for *gasfac*. Table 3.1 shows the gas weights with errors that have been measured in this experiment, and the weights from previous experiments in the cases where the targets were not emptied in between. Table 3.2 shows the final values for *gasfac*, for each of the different target combinations, T/^{3}He , T/D, *etc.* that were used in this analysis, calculated using Eq. 3.4, and the accompanying errors. The systematic error of ~ 0.5% shown by the variation in weighings over several experiments (see Table 3.1) is not included in the quoted errors.

3.2.1 Decay Correction

There is a final correction to the ratios due to the decay of the T target. The amount of T left at a time t, measured in weeks, given a half life of 637.6 weeks, is:

$$N = N_0 exp(-0.693t/637.6)$$

where N_0 is the original amount, at $t = 0$ and 0.693 is the natural logarithm of $\frac{1}{2}$; call the exponential factor $x = x(t)$. If Y_m is the yield that is measured during a run, and if Y_T and $Y_{^3He}$ are the yields we would expect if the target were full of T and ^{3}He respectively, at the target pressure, then we can write

$$Y_m = Y_T\, x + Y_{^3He}\,(1-x)$$

or

$$Y_T = \left(Y_m - Y_{^3He}\,(1-x)\right)\left(\frac{1}{x}\right).$$

Now, we have measured the ^{3}He yield for the ^{3}He target, call the result $Y'_{^3He}$. To get the yield we would have had at the higher areal density of the T target, we must scale by the relative target densities, that is we replace $Y_{^3He}$ with $gasfac \times Y'_{^3He}$ to get

$$Y_T = \left(Y_m - (gasfac)Y'_{^3He}\,(1-x)\right)\left(\frac{1}{x}\right).$$

In some cases extra π^+ runs were done at a later time, and those runs will have a different correction. For instance, if two sets of runs were done for π^+T, one at one week after the target was filled, and one at four weeks, then if the areas of the elastic peaks of the two sets are A_1 and A_4, and f_1 and f_4 are $A_1/(A_1+A_4)$ and $A_4/(A_1+A_4)$ respectively, the fractions of counts in the first week and fourth week sets, and if we denote x at those times as x_1 and x_4, then we have

$$Y_m = Y_T\,(x_1 f_1 + x_4 f_4) + (gasfac)Y'_3((1-x_1)f_1 + (1-x_4)f_4).$$

This correction is included in all final results. The correction for R is the largest because there are four factors contributing. It is usually les that 0.5%, but goes as high as 1.2% for the 220 MeV point.

3.3 Spectrometer Calibration

All of the EPICS chamber and target quantities were calibrated at 120°, 180 MeV (Sec. 2.3.3). The polynomials do not include information about the target thickness or about the way varying the EURYDICE field affects the paths of the scattered pions. Some quantities depend strongly on these factors, such as missing mass, Y_{front} and Y_{target}, as was discussed in Sec. 2.4.1. These quantities should maintain a strong relationship with the shapes as seen at the

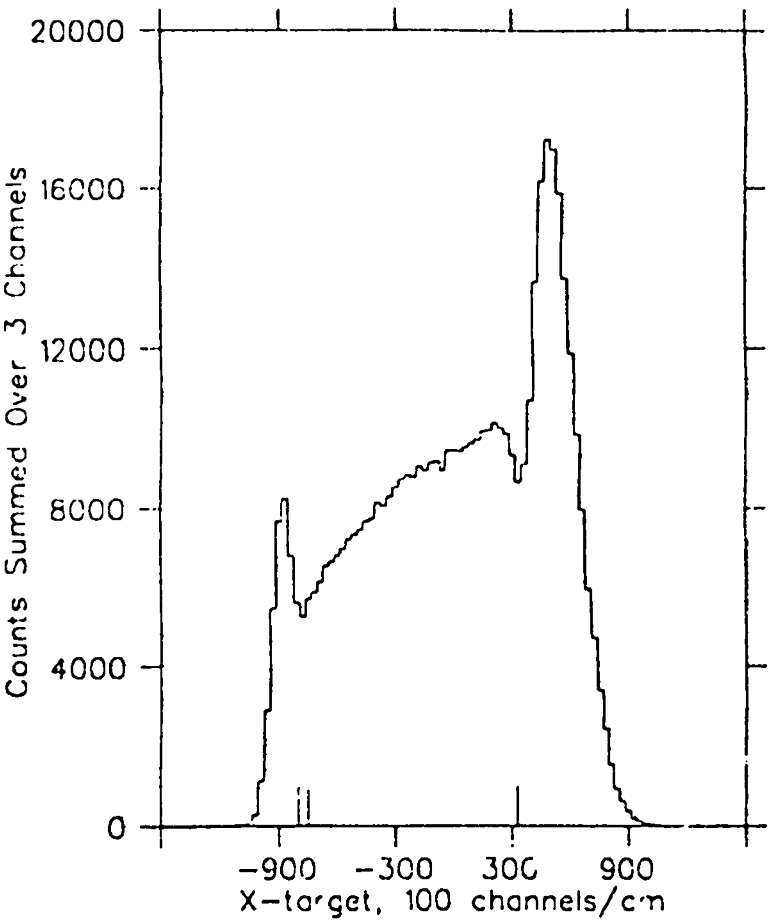

Figure 3.2: X_{target} at 116°. The two outermost marks show the calculated position of the end caps. The inner mark shows the position used for the cut during replay.

calibration kinematics 120°, 180 MeV, but there could be some distortion, so that it is not proper to use their values as an absolute spatial or energy reference. One exceptions is X_{target} . The x axis is perpendicular to the EURYDICE bending plane, and so X_{target} should be relatively unaffected by angle and energy changes that require a EURYDICE field change; we expect some loss of resolution in X_{target} due to the thick target effects however, (see Sec. 2.4.1). Fig. 3.2 shows X_{target} for 116°. The two outermost marks show the *predicted* location of the target end caps; the overlap is excellent. The end-cap locations were predicted equally well at all angles and energies. It looks like the calculated mark for the upper end cap, which is the farthest on the left in the figure, is somewhat wide, and so in practice this cut was tightened a little, to the inside mark on the left. A firm X_{target} cut at these marks was used during all of the replay to eliminate events from scattering in the end caps.

The shape of Y_{target} depends on the scattering angle (and so on the EURYDICE field), as Fig. 3.3 shows. The width of Y_{target} decreases as we progress backwards in scattering angle. This is the same effect that was seen in Sec. 2.4.1, where the ray tracing was discussed. Because Y_{target} is a calculated quantity, it might seem reasonable to use the uncalculated front-chamber quantities to

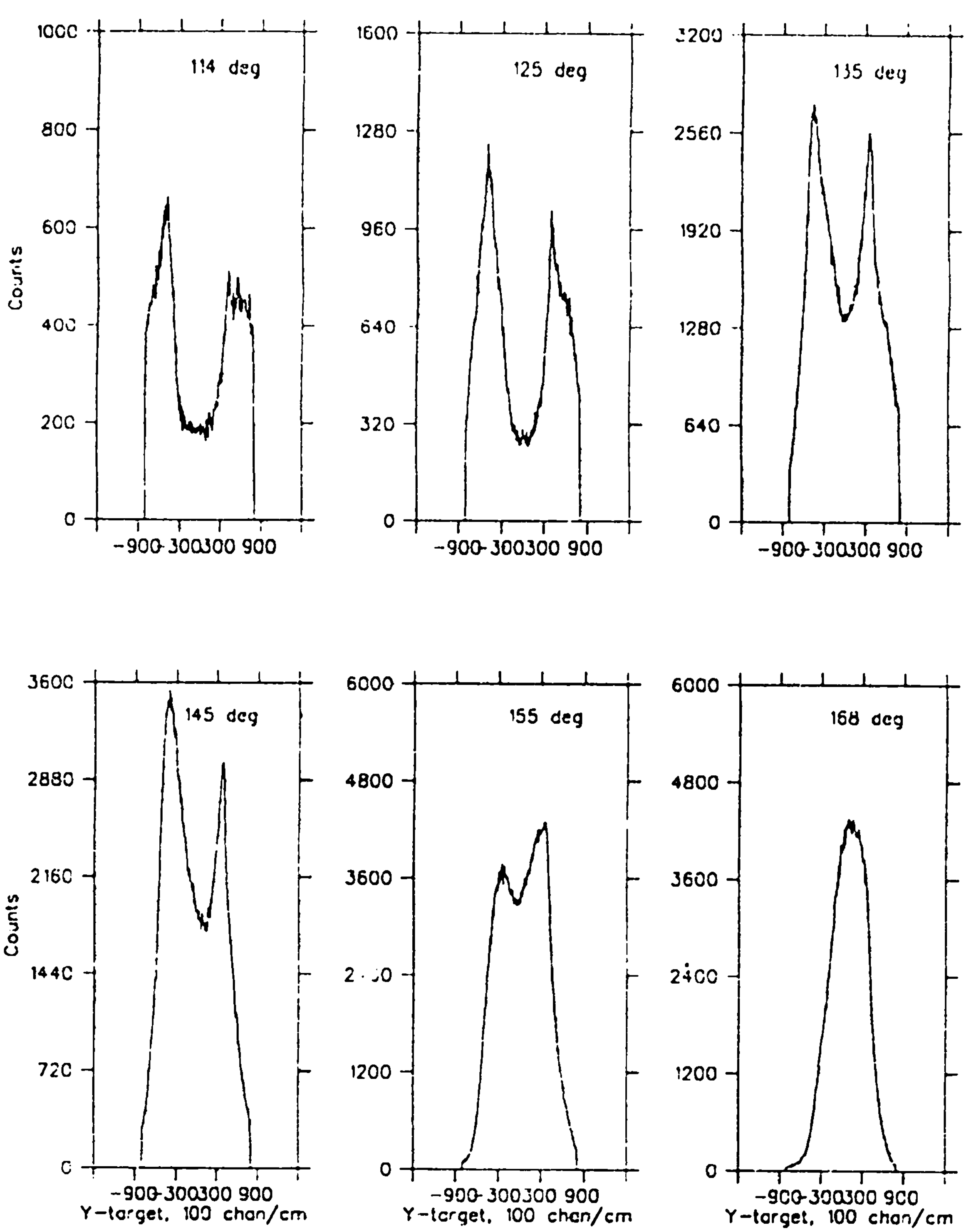

Figure 3.3: Y_{target} at 180 MeV becomes narrower and the 'wings' become less pronounced as the scattering angle increases. The centroid of the distribution moves right slightly.

determine the proper Y-direction cuts, since the calculated quantities are only calibrated for the most forward angle in the experiment. However, the ray tracing presented in Sec. 2.4.1 was done after the analysis of the yields, in order to make sure that systematics were understood. Nevertheless, Y_{target} is a reasonable representation of the actual ray profile at the spectrometer entrance, as shown in Sec. 2.4.1; the ray tracing therefore validates the use of Y_{target} cuts during the data reduction.

Most of Y_{target} is due to scattering in the aluminum target walls, and it is desirable to remove as much of this as possible. Since all of the elastic-peak-energy scattering comes from the gas or from a narrow kinematic band in the background corresponding to the same energy, we can use a cut around this peak to define the gas volume. Figure 3.4 shows Y_{target} for T targets at 116° and 167° with this gas volume cut. Overlaid with the histogram for each angle is the corresponding histogram for the background runs with the same gas volume cut. Because there is no elastic scattering in this kinematical region for the background target, the lower histograms are depleted in the middle, which clearly shows the gas volume. For each point, a series of Y_{target} cuts were made to define the gas volume. The cuts went from wider to narrower, but remained symmetric around the center of the gas volume, defined as the deficit shown by the overlaid histograms. Thus we maximize the ratio of counts from scattering in the gas to counts from scattering in the target walls.

θ_{target} and ϕ_{target} are rarely re-calibrated for experiments with bending magnets at the target position, and they were not for this experiment. For experiments with thin targets and no bending magnet at the target position, ϕ_{target} gives a reliable measure of the variation in scattering angle over the front of the spectrometer. The ϕ_{target} histogram can be binned in three bins, encompassing the central one degree, and one degree greater and less than the central angle. Thus, the angular resolution can be increased by factor of three. We have seen in section 2.4.1 that the angular acceptance was greatly increased by the thick target and the extra bending magnet, and that each angle was spread over the entire spectrometer entrance. Therefore, the extra angular binning was not possible. Cuts on θ_{target} and ϕ_{target} were not used for any of the analysis.

θ_{check} and ϕ_{check} are not affected by EURYDICE as they measure the *difference* in trajectory angle between the front and rear chambers. Since the muon rejector was not used, these histograms provided the only way of removing muons in the spectra. As discussed in Sec. 2.3.4, the muon-to-pion ratio was negligible at most angles, and the muon and pion peaks do not overlap, so the straight-line background drawing was not affected by the lack of the muon rejector (see Sec. 3.6).

The particle identification (PID) was done in the regular way, with a two dimensional plot of average pulse height in scintillators S_2 and S_3, which follow the rear wire chambers, *vs.* the time of flight between these two.

A rather tight box was used, although a check showed that a box which included some 'stragglers' did not affect the missing-mass shape.

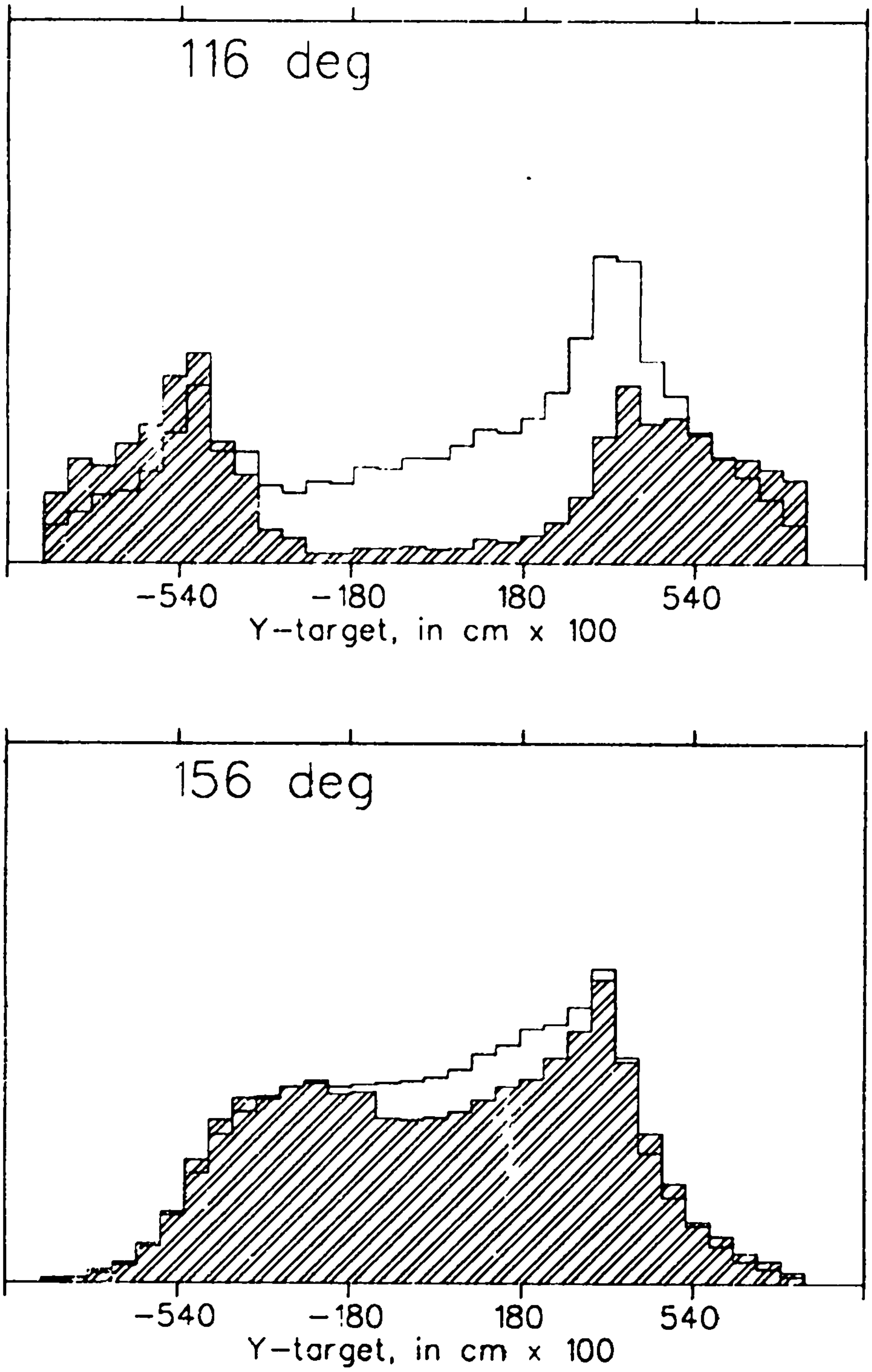

Figure 3.4: Y_{target} for T and D, top and bottom respectively are 116° and 156°, lab. scattering angle.

The spectrometer polynomials were recalibrated for the replay, using calibration data taken during the experiment. This improved the shape of the various histograms somewhat, but the changes were not major. We did all of the calibration runs at 120°. This means that there was no way to include possible angle dependence due to the variation of the EURYDICE field with angle. These effects should cancel in the scattering ratios as numerator and denominator are measured with the same kinematical settings. The difference in acceptance between T and D kinematics was investigated in Sec. 2.4.1.

The ray tracing analysis from Chap. 2 showed a slight acceptance correction between T and ^{3}He kinematics, which will cancel in all of the ratios, but which should be included for the cross sections. Overlays of the Y_{target} histograms at each angle for the different kinematics showed little or no variation between T and D ; identical cuts on Y_{target} were used to define the gas volume for all runs at each point, including the normalization (D) and background (D with T kinematics) runs.

Figure 3.5 shows an 'acceptance scan' done with the H target at the beginning of the experiment, at 120°, 180 MeV. The spectrometer tune was changed so that elastically-scattered particles were focused on different parts of the focal plane. For the same incoming pion, a change in momentum corresponds to a change in missing mass. Measuring the yield at different momenta gives a correction factor to use for the various locations in missing mass. For these experiments, all peaks were on the center of the focal plane, and so the corrections are not needed. The scan is fairly flat in the region under the elastic peaks (usually between -2.0 MeV and +3.0 MeV), with variation of about 10%. This variation is not important for the ratios, as the yield for numerator and denominator is always taken for the same bin in missing mass therefore the acceptance variation is the same in numerator and denominator, and cancels. For the cross sections, the variation will affect the target and normalization-target yields differently for those parts of the peaks that do not exactly overlay each other. This overlap is less than 10% of the peak areas, and as the acceptance variation on average is less than 10%, quoting an uncertainty of 10% × 10% = 1% accounts for this possibility conservatively.

The steep drops on the edges mean that features in this region are often indistinguishable due to lack of counts.

3.4 Muon Rejector

The muon rejector is discussed in Sec. 2.3.4. It was not used for the reasons cited there. However, one set of analysis was done for all of the points, using background subtractions, see Sec. 3.6.1 comparing results with and without the muon rejector. With two exceptions, all results agreed within one σ. The exceptional case showed a variation of several σ, which has been attributed to muon-rejector misuse, see Sec. 2.3.4. Therefore, the muon rejector is not used

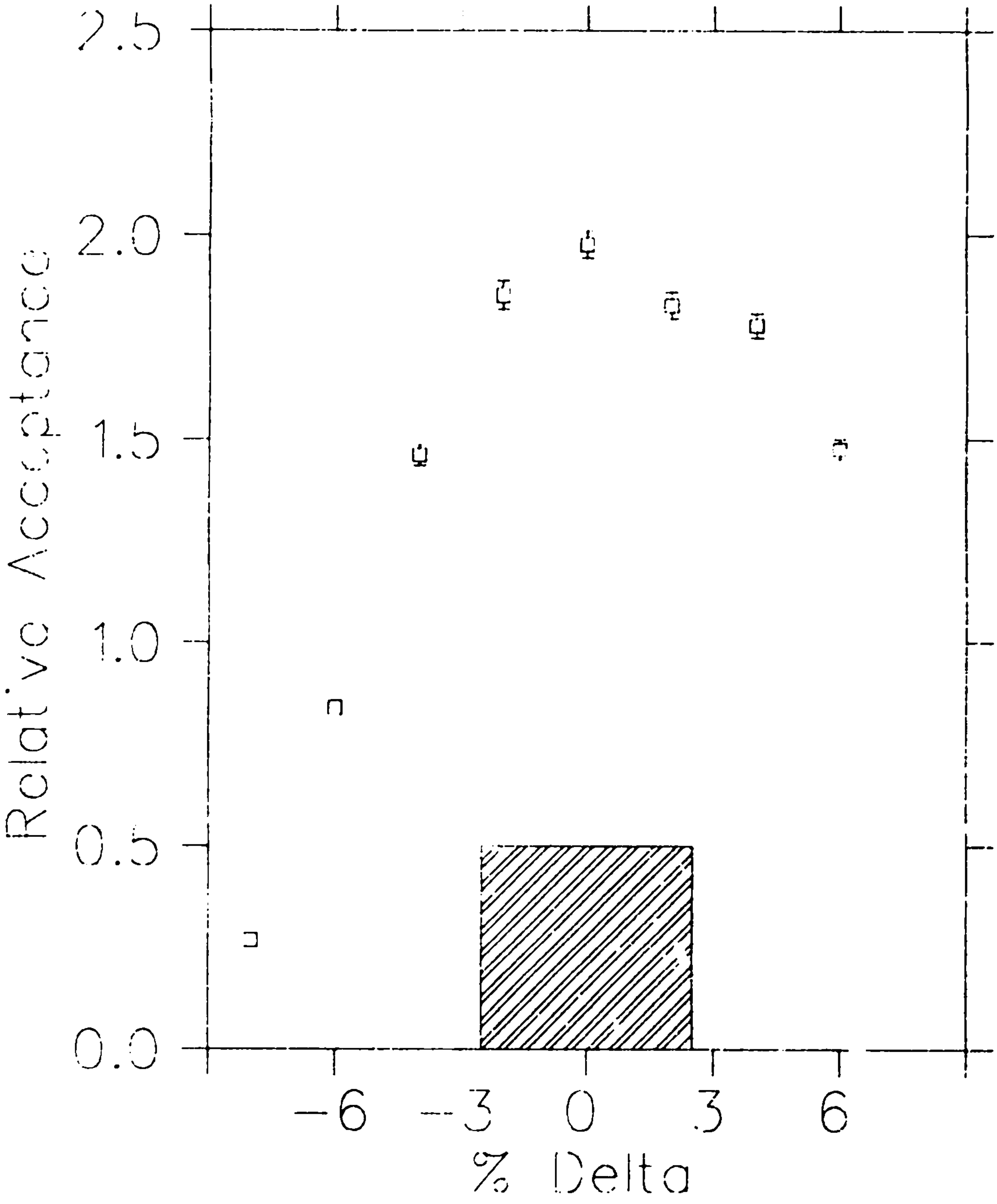

Figure 3.5: The acceptance scan for this experiment, using the Hydrogen target. The box shows the region from -4.0 to 4.0 MeV, which covers all of the elastic peaks.

Angles and Energies						
142 MeV				158°	162°	169°
180 MeV	114°	125°	135°	145°	155°	168°
220 MeV						168°
256 MeV						168°

Table 3.3: **The points covered by the current experiments.**

for any quoted results.

3.5 Data

3.5.1 What Was Measured

Experiment 1155 measured an angular distribution from 116° to 167° at the Δ_{33} resonance pion energy of 180 MeV. Experiment 1064 measured an excitation function from 142 MeV to 256 MeV at the most backward angle possible for each energy. Two extra points were measured at 142 MeV, at very large angles as a consistency check. The largest-angle point at this energy will not be reported here because of some remaining ambiguities in the data reduction. The angles and energies covered are given in Table 3.3.

Several runs were taken at each point. For the main part of the experiment, there were three targets on the turntable: T, ^{3}He, and D. Each target was used at T kinematics, and the D target was also used with D kinematics for the normalization yields. Henceforth, we shall refer to D runs cases with D-elastic-scattering kinematics as D, these are the normalization runs, and to D runs with T-elastic-scattering kinematics as D/T, these are the background runs. There was some disagreement over whether it would be better to extract the yields with some sort of line shape to represent the backgrounds, or whether it would be better to use the D with T kinematics for background subtraction. The result was that in some cases there is a paucity of background counts, especially for the π^-D runs, that makes background subtraction nearly impossible. Eventually, both methods were used; the results are discussed below.

Since there was not room for the H target on the turntable for the main body of runs, we could not take H runs with D kinematics, to do background subtraction with the normalization peaks. At the end of the experiment, we removed the T and ^{3}He targets, using just D and H. We repeated several angles and energies to get D normalization data with backgrounds to subtract, but were unable to cover the entire set of points because of time constraints. The points that were covered this way were all at 180 MeV, at 114°, 135°, 145° and 168°.

3.5.2 Quality of the Data

The overall quality of the data is good, with the exception of the background statistics, which were mentioned above. The usual goal was to get at least 10,000 counts in the elastic scattering peaks in order to get a 3% statistical error. This was considered a stricter requirement for the angular distribution, where we wanted smaller error bars in order to clearly differentiate among the three Superratio curves calculated by Gibbs and Gibson for the three values of δ_e (see Sec. 1.7), than for the excitation function. Within a set of runs at the same kinematics, all of the peaks should overlap very well. For instance, for a given point, say 120° scattering at 180 MeV, the π^+T, π^{+3}He, π^-T and π^{-3}He peaks should have excellent overlap, as should π^+D and π^-D . However, the latter set need not line up well with the former set, since the kinematics are different for T and D elastic scattering. The eye can do a very good job of comparison when the runs are overlaid on screen or paper. All runs were plotted against each other to check for both position of the peak's center and the overall shape of the peak. The only questionable peak was the 146°, 180 MeV one, shown in Fig. 3.6(The vertical line is to aid in comparing the peaks.) The upper peak is shifted somewhat to the left. The shape of the upper peak seems distorted on the right, perhaps as if a magnet drift had shifted part of the spectrum. This shape difference is especially bothersome at the base of the peak in the region between the peak and the breakup. A clear idea of what is going on here is necessary for drawing the straight-line backgrounds discussed in Sec. 3.6.

At 167° 180 MeV, we had spectrometer problems. During these runs, one of the spectrometer turbo pumps was failing, allowing the vacuum to rise slightly. When this happened the system automatically dropped a gate valve that separated the spectrometer from the scattering chamber. In some cases data taking continued for some time with the scattered particles traversing this valve, which resulted in a large energy loss and a resultant loss of counts in the peak. Secondary scattering from the valve is also possible, which results in unpredictable effects on the spectral shape. This made it difficult to analyze this point, both because the irregular shape of the background made it hard to select a background representation that looked good, and because the D runs done for background did not have the same time with the valve closed as some of the other runs, thus the subtraction was not correct. There were enough foreground runs that the problem does not seem to have affected the results; these runs were analyzed in the standard ways (see below). The D normalization run for $\pi^-$is suspicious: Fig. 3.7 shows this run. The energy loss in the valve is approximately 15 MeV, and no secondary peak is obvious at this energy in missing mass. However, the region between the breakup and the peak is filled in, especially in the upper plot (π^+D). Extra counts in this region could come from scatters with energy to the left of the peak; these would be background events that lost energy in the valve. The areas to the left of the peaks are not a good match either. Finally, the lower peak is wider than the upper one. It is difficult to say whether any or

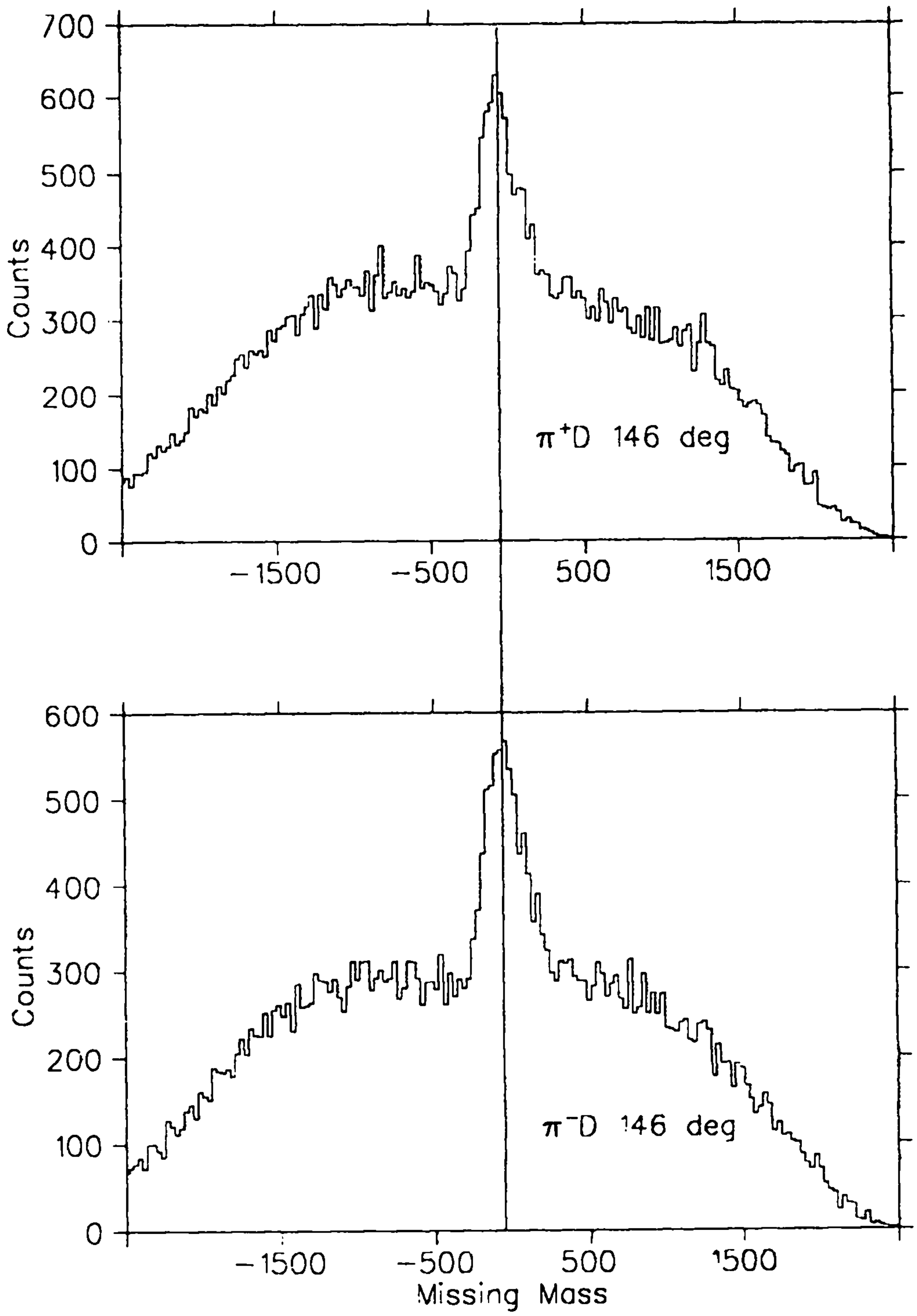

Figure 3.6: The D normalization runs at 146°, 180 MeV. 100 = 1 MeV. The vertical line is drawn to aid in comparing the peak location and shape. The areas to the right of the peak do not have the same shape.

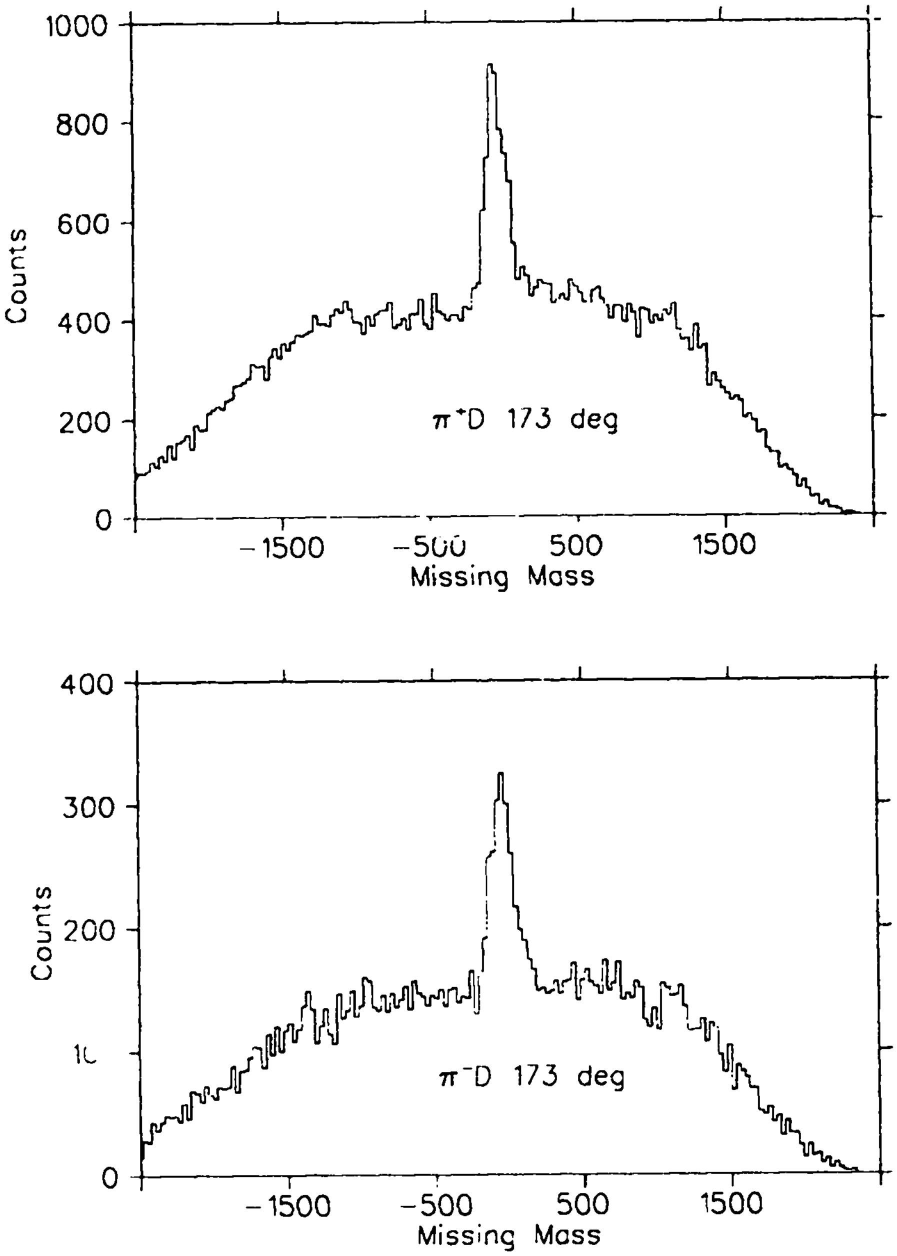

Figure 3.7: The D normalization run at 167°, 180 MeV.

all of these effects are due to the valve difficulties Statistics on the lower run are much poorer than on the upper, which makes comparisons difficult. These runs did prove very difficult to analyze (see Sec. 3.6), primarily because it was hard to tell where the peaks began and ended.

Finally, as discussed earlier, the low statistics of some of the π^-D background runs made background subtraction very hard. Comparison of the different methods, which are discussed below, showed some significant differences for the worst points.

3.5.3 Statistical Variations

Even in cases where there are good statistics, statistical fluctuations can introduce errors in a subtle way. The farthest back points, $\theta_{scatt} > 130°$, have a very large number of counts in the supra-elastic region (we shall refer to the region in missing mass to the left of the peak, where missing mass is lower and the scattered particles have higher energy, as the supra-elastic region), and even those more forward-angled runs, where the backgrounds are relatively small, have many counts, and a smooth-appearing spectrum. With this idea in mind, it might appear that the way to choose a scaling range is so that systematic effects will be minimized. For instance, one method tried was to scale the runs over a few-MeV range close to the peaks. The idea was to emphasize that part of the background that was close to the area of interest and to lessen the effects of any general shape difference in the backgrounds that might have some cumulative effect if the scaling range were large. This idea was especially attractive, because at this energy, around 15 - 20 MeV excitation in the surrounding background-producing materials, we do not expect sharp peaks or structures. However, we must keep in mind that the counts in any scaling range have an uncertainty of $\sqrt{\# \, counts}$. For instance, if we use a scaling range of -10 MeV to -5 MeV, which covers 50 bins in our missing mass histograms, and if we have an average of 100 counts *per* channel, which is near the median number for this experiment, then we have an uncertainty in the sum over these channels of

$$\sqrt{100 \times 50} = 71 = 1.4\% \; of \; 5000,$$

and an uncertainty in the scaling factor between two runs of this count number of

$$\sqrt{.014^2 + .014^2} = 2.0\%.$$

Of course, this is just standard uncertainty propagation, and indeed this uncertainty must be included as the ratio is used to scale the peak area. This is the method that is used in the subtraction analysis (see sec. 3.6.1). Two percent is already a serious uncertainty to have to add on to the ratios, but there is a more serious matter of principle involved. Figure 3.8 is an example of randomly generated flat spectra, with 150000 total counts. Also in the figure is a plot of the ratio of the two spectra taken over several energy bins. Each bin is 5 MeV wide.

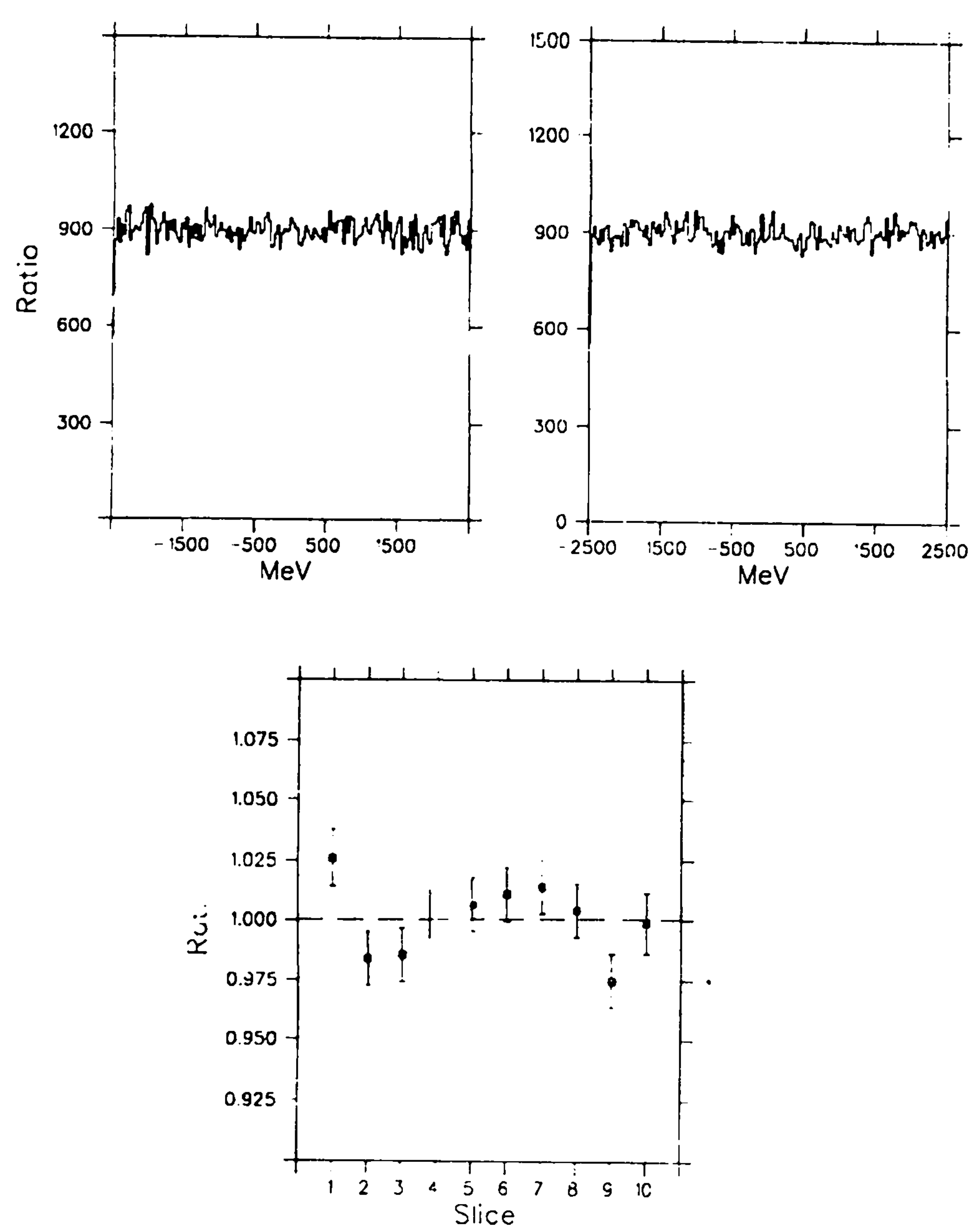

Figure 3.8: Top: two 'flat' spectra, randomly generated with 150,000 counts each. Bottom, ratios of the two spectra, taken at 50 channel intervals (five MeV in missing mass). One sigma statistical error bars are shown.

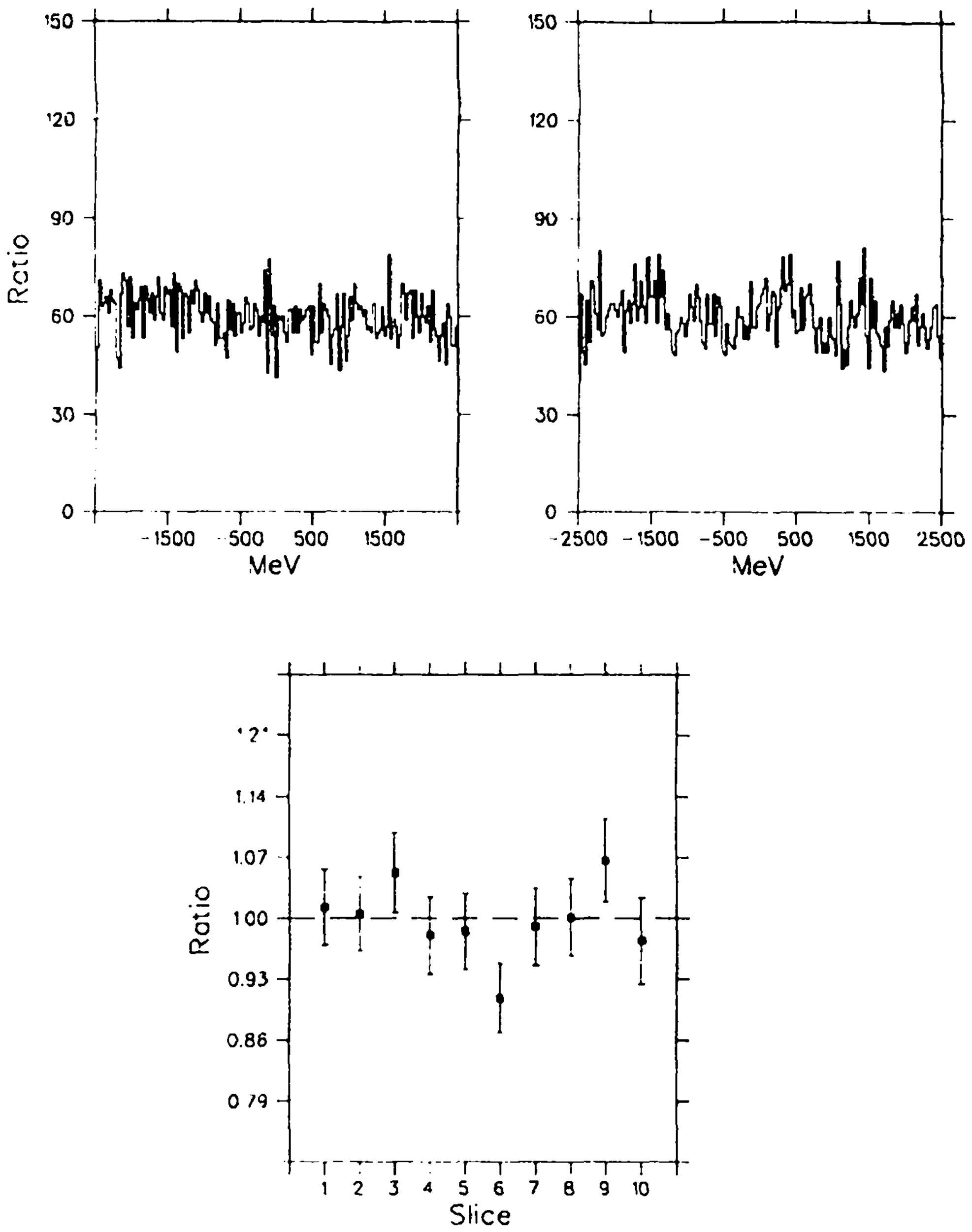

Figure 3.9: **Same as Fig. 3.8 except there are 10,000 counts instead of 150,000.**

and each is next to the other; *e.g.* the first range is from -24 MeV to -19 MeV, the second is for -19 MeV to -14 MeV, *etc.* The errors are one sigma statistical error bars, as discussed above. Ideally, the ratio would be 1.0. Five of the ten values are within one sigma of 1.0, which is reasonably close to the expected 2/3 value , considering the small number of trials. The difference between the ratios of the first and second points is particularly striking, and serves to illustrate the point. The difference is 4%. Now while this is not statistically invalid, it is almost as big as the statistical error in ρ^+ , for many of the experimental points. Figure 3.9 is an example of the same exercise, but with only 10,000 counts in the total spectra. This is a small number, but it is well above the total number of background counts for many points. In this case, a similar reasonable number of ratios have ranges within one sigma of 1.0 (seven of them), but the greatest discrepancy, between points nine and ten, is 12%! Of course, such a result is totally unacceptable. So, in addition to the statistical considerations, these 'errors of chance' dictate that we use the largest possible scaling ranges in all cases.

3.6 Methods of Data Reduction

Two methods of data reduction were considered. As discussed earlier, scaling a background run to the foreground in the supra-elastic region has some problems, but it will work if we accept large statistical errors. Another method is to approximate the background somehow, and subtract this approximation from the foreground. A straight line is usually a reasonable approximation; The data were analyzed by both methods where possible (excepting only those D runs that have no backgrounds to subtract). I discuss the methods and the results and accuracy in the following two sections. The D normalization data presented special problems; it is considered separately.

3.6.1 Scaling

The supra-elastic region cannot be reached by scattering from the target gas, so this region is filled by background scattering, primarily from the aluminum canister walls. In the ideal case, we expect the supra-elastic region to have exactly the same shape for π^+T, π^{+3}He and π^+ D/T , and for π^-T, π^{-3}He and π^-D/T . This assumes that all of the targets are identical and that they are placed in exactly the same orientation for their respective runs. Multiple scattering and energy loss differences should be minimal between T and ^{3}He and D. One possible difference that cannot be measured is the scattering from the fill valves on each target. We made an effort to align all of these valves in the same way, but the inflexibility of the capilary tubes that connected the valves to the target canisters meant that there was some variation. If we assume that all of these variations can be ignored, then the T, ^{3}He and D spectra for each polarity should match, and we can use this region to scale the histograms for background subtraction. In Sec. 3.5.3, we saw that there can be quite a variation in a supposedly flat region; we cannot scale the runs to each other over a small region in missing mass, because this introduces a large uncertainty; we need to use as large a scaling area as possible. For the right side of the scaling area, we should go as near as possible to the scattering peak. The peak gets narrower as the scattering angle increases, because $dE/d\theta$ decreases with angle, where E is the kinetic energy of the scattered particle. Therefore, the solid angle subtended by the spectrometer encompases a narrower energy range as the scattering angle increases, and the peak is narrower in missing mass. That means that we can use a wider and wider scaling area as the scattering angle increases. For example, in the angular distribution analysis, scaling ranges of -22 MeV — -4.5 MeV for 114°, and -22 MeV — -2.5 MeV for 167° were used.

The main problem with with this method was the lack of π^- background counts for some of the points. In particular, 146° and 156° have very poor π^- background statistics. Where the background statistics are good, the scaling method and the straight line background method, which is discussed below (Sec. 3.6.2), gave the same results, within error bars. Figure 3.10 shows how this kind of background scaling works out for a case where there are pretty good background statistics, and where there are not. The background is scaled to the foreground over the area that is marked on the histograms, and then subtracted. The good result, on the left, has some bumps in the supra-elastic region that may or may not be the result of actual differences in the supra-elastic shape. Nevertheless, the good statistics make for a smooth, well defined supra-elastic shape, and visual inspection shows that there are no gross shape differences over the runs. In this case, we can confidently scale the background to the foreground for subtraction, quoting only statistical errors for the scaling procedure. On the right is a subtraction done with runs with poorer statistics. The low number of background counts requires a very large scaling factor. This multiplies the random variations in the background, and so after the subtraction the result is so ragged that visual inspection gives no assurance that the shapes are the same, and that the technique is valid. Of course, such a large scaling factor would necessitate quoting a very large statistical error, but the quality of data makes us unable to tell if a systematic error is indicated.

3.6.2 Straight-Line Backgrounds

Figure 3.11 shows the π^+ D/T backgrounds in the elastic-peak region for two different points. The first, at 114° has rather poor statistics, and the second, at 135° is typical of most of the experimental points. Considering that an uncertainty equal to the square root of the number of counts should be assumed for each channel, even the low-statistics run can reasonably be approximated by a straight line.

An analysis routine was written to subtract straight line background approximations from standard LAMPF histograms. Two runs are analyzed at a time. For each run two points are input to draw the line through. The area defined by the line is subtracted from the missing mass, and yields and ratios between the two runs are taken over a set of ranges in missing mass. Figure 3.12 is an example of this program's output. In the upper left is the π^+T histogram for 155°, with the specified line background overlaid on it. Below this is the result of subtracting the line from the histogram. The area above the line is defined to be the elastic peak. Notice that the line intersects the base of the peak on the left, and the lowest point between the peak and the breakup on the right. The same results are shown on the right, for π^{+3}He. Because the kinematics are the same, we expect the peak shapes to be the same; this is an important aid in drawing the line. Figure 3.13 shows the way ρ^+ varies for various widths of the peaks used. The first three values draw the left edge at the left side of the peak, and take the right side to be first near the peak's middle, then halfway to the

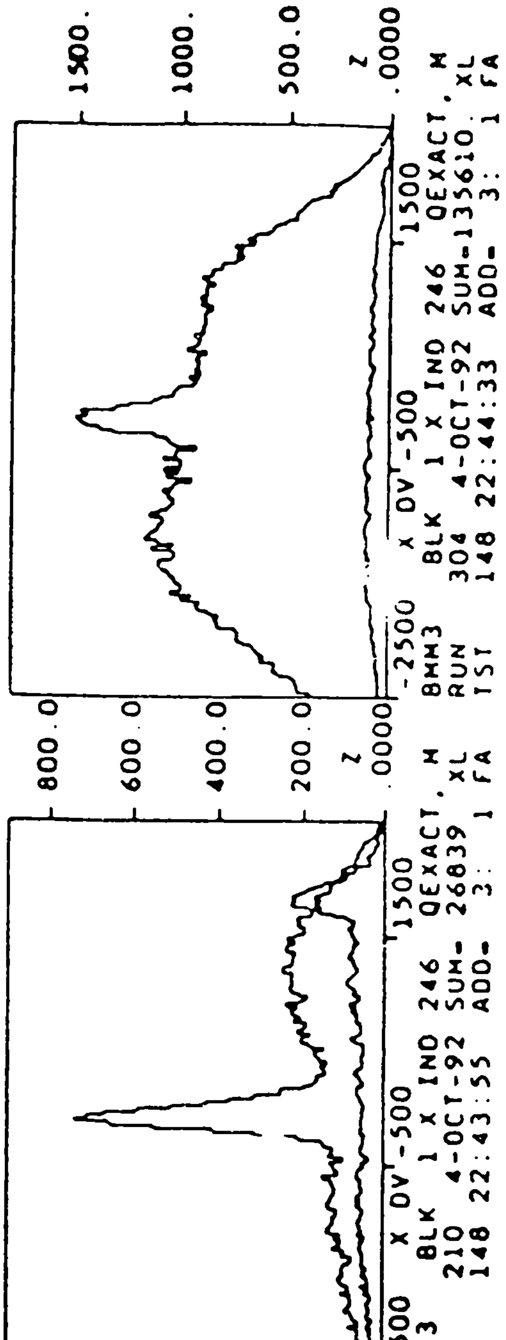

Figure 3.10: *left:* A good looking background subtraction, at 116° *right:* A poor result, from 146°. The output is from the LAMPF histogram system.

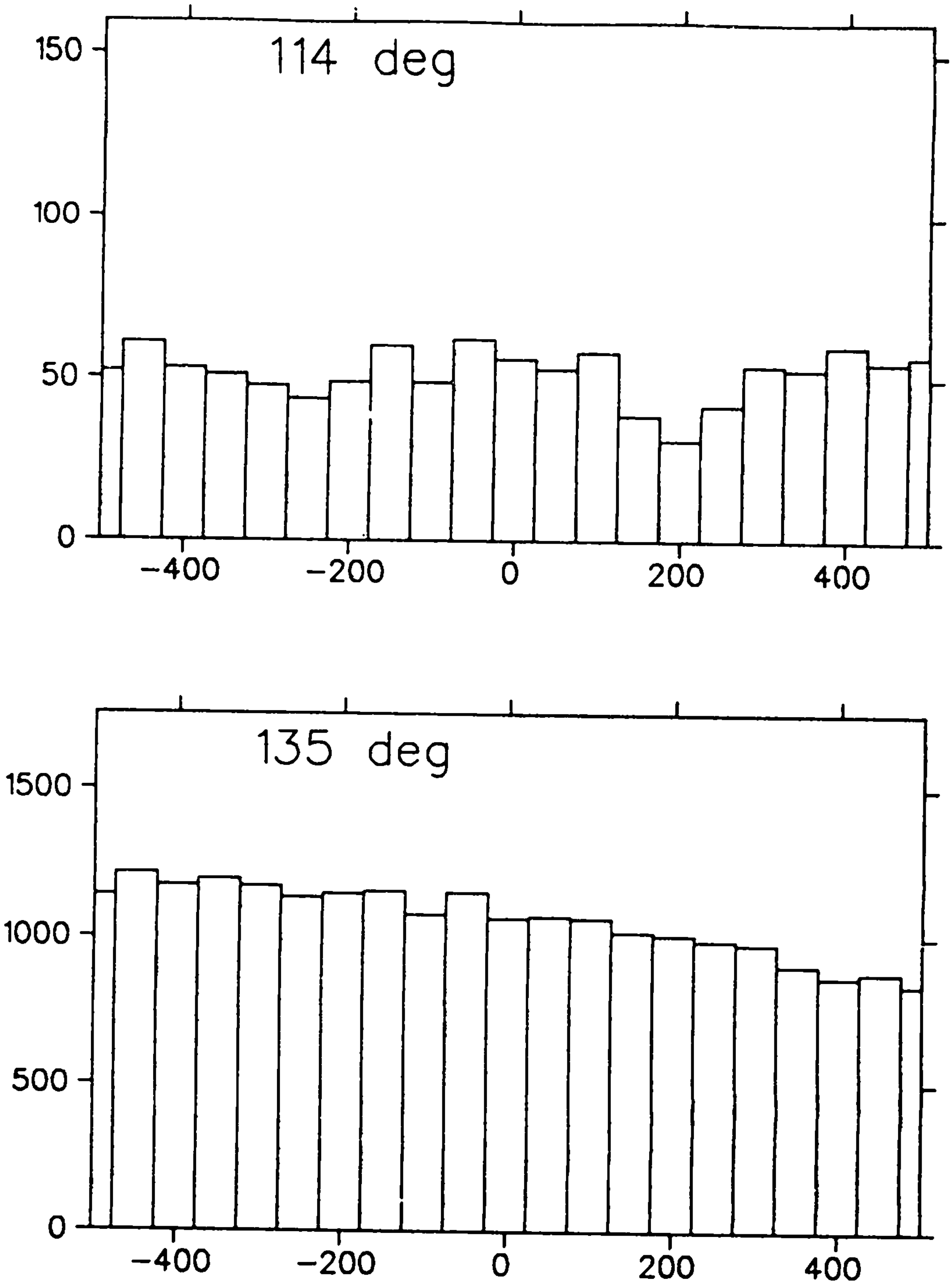

Figure 3.11: **Background under the peaks at 114° and 135°**

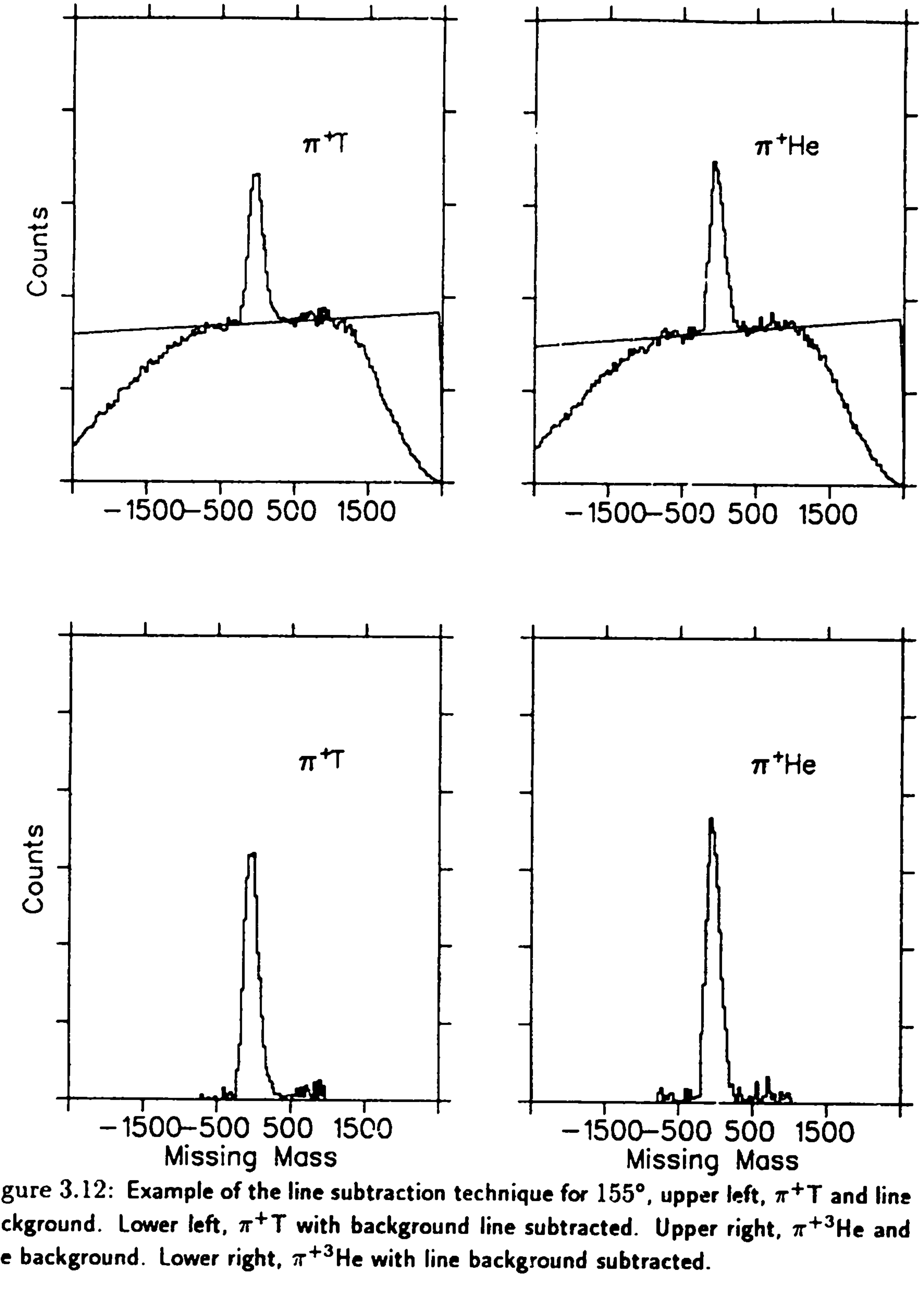

Figure 3.12: Example of the line subtraction technique for 155°, upper left, π^+T and line background. Lower left, π^+T with background line subtracted. Upper right, π^{+3}He and line background. Lower right, π^{+3}He with line background subtracted.

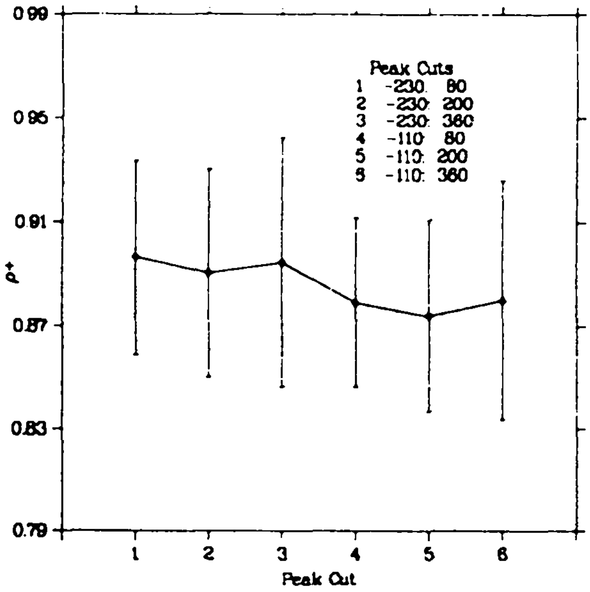

Figure 3.13: Variation of ρ^+ at 155° with width of peak used for the ratio. See discussion in the text.

edge, and then at the end of the straggling tail. The second three points repeat these values of the right side of the peak, but use a value for the left side of the peak that is inside the true edge, nearer to the peak's center. Since the T and ^{3}He kinematics are the same, we expect that the width of the peak used will not be important in the ratios, as long as it is the same for each case. However, if the background line is misdrawn for one of the histograms, the value of the ratio will not be consistent over different regions of the peaks; this is another test of how good the line selected matches the background.

As mentioned earlier, the program allows two histograms to be analyzed simultaneously, *e.g.* π^+T and π^{+3}He. Since the π^+ background is the same for each of these histograms (assuming the canisters are the same), comparing the final line to the background at the left of the peak (the supra-elastic region) for the two histograms helps highlight discrepancies. Likewise, it can be useful to analyze the opposite polarity sets together *e.g.* π^+T and π^{-3}He, because under charge symmetry these cross sections should be the same, both in the elastic and the break-up regions. This provides other criteria for comparison between the two lines that are chosen as backgrounds. Ideally, both of these methods should give the same results, and this is another check on the accuracy of the results. Most of the data were analyzed both ways, first the same-polarity pairs, and then the opposite-polarity symmetric pairs.

Computing the error for this method was straightforward. If we imagine a spectrum with a single peak sitting on top of a perfectly flat background (that is, the shape is flat, and the actual spectrum is flat within statistics), then we can use the flat regions that are *not* under the peak to get a very good position for the background line. In this case, we would not have to add any error to represent the uncertainty in the line. If the number of counts in the peak was A, and the number of counts in the background *under* the peak was B, then the statistical error would be $\sqrt{A+B}$. In the opposite extreme, we can imagine that there is *no* flat region at the edges of the peak. This is equivalent to an experiment where the available region in missing mass is only as wide as the peak. Then we would use the standard formula for a single-channel experiment, which is $\sigma = \sqrt{A+2B}$. The proper error is somewhere between these two. For all the runs, there is enough background to make a good estimate of the proper line slope and intersection points. However it is certainly not perfect, and $\sqrt{A+B}$ is too small an error to quote. $\sigma = \sqrt{A+\frac{3}{2}B}$ was chosen as a compromise between the two extremes. A is the area in the peak between whatever limits are used to calculate the yield, (this is the full width of the peak in the case of the cross sections, and in *most* of the ratio calculations as well, excepting those cases where including the tail regions caused large discrepancies in the ratios), and B is the area between these same limits under the line that is drawn by the program.

The Y_{target} cut chosen for this process is the one that provides the best reference points for drawing the line, and is in the set of reasonable Y_{target} cuts found by varying the gas volume cut during the scaling-analysis effort. The shape change in Y_{target} shown in Fig. 3.5 caused a sharp slope change near the peak for some Y_{target} cuts, and so these particular cuts were not used. Figure 3.14 shows how the two methods compare. The filled squares are the final results for r_1 , computed by the line-background method. The open squares are from the scale and subtract.

The straight-line-background method was used for the reported results, in order to eliminate the problems of muon peaks and statistical uncertainties discussed for the scaling method.

3.6.3 Deuterium ratios

Now consider the expected values of ρD , using the ion chamber for the norm (*norm*1). At a given energy, the beams have a certain particle content, both pions and other particles, and this content is not the same for the two polarities; for example, say that the only contaminant is protons, which will only be in the π^+ beam. Then the ion-chamber current will be proportional to the number of pions and protons that it sees. Since the number of protons is a constant fraction of the pion beam for a given energy and proton-beam steering, this current is proportional to the total number of pions as well. Likewise, the chamber current for the π^-beam is proportional to the number of pions, but because the contamination is different, the proportionality constant is not the same for the two polarities.

$\rho D \equiv d\sigma(\pi^+\mathrm{D})/d\sigma(\pi^-\mathrm{D})$ is the ratio of $\pi^\pm$ scattering yields from D. Each yield is proportional to the cross section, and if we assume that πD scattering is charge symmetric, then the cross sections are equal and cancel in the ratio. This leaves a ratio of beam currents. However, over the angular distribution, the same incident beam is used at each point, and therefore ρD is expected to be constant with angle.

There are some mistakes that could change this. For example, if the target is misplaced for one of the D runs. There are usually fewer D runs than other runs, and so this is proportionally a larger mistake. This kind of error, however, is related *only to D* . Since it is not likely that errors of this type with the T and ^{3}He runs will be correlated with those of the D runs, there is no reason to preserve this wrong value of ρD . Instead, it is better to average the values of ρD over the angular distribution. Figure 3.15 is a plot of ρD over the entire angular distribution. At each point the ratio was calculated several ways. A straight line background subtraction was done. If there were H with D kinematics data for subtraction, this was done, and straight-line backgrounds were drawn for these latter sets as well. In several cases, extra line-background efforts were made to check consistency. Several tries at drawing the line backgrounds train the eye, and the results become more reproducible with practice. The final set of line-background results was averaged over each point in the angular distribution, leaving out the 146° and 167° points, for the reasons listed in Sec. 3.5. Properly including these two would have required the addition of a large systematic error

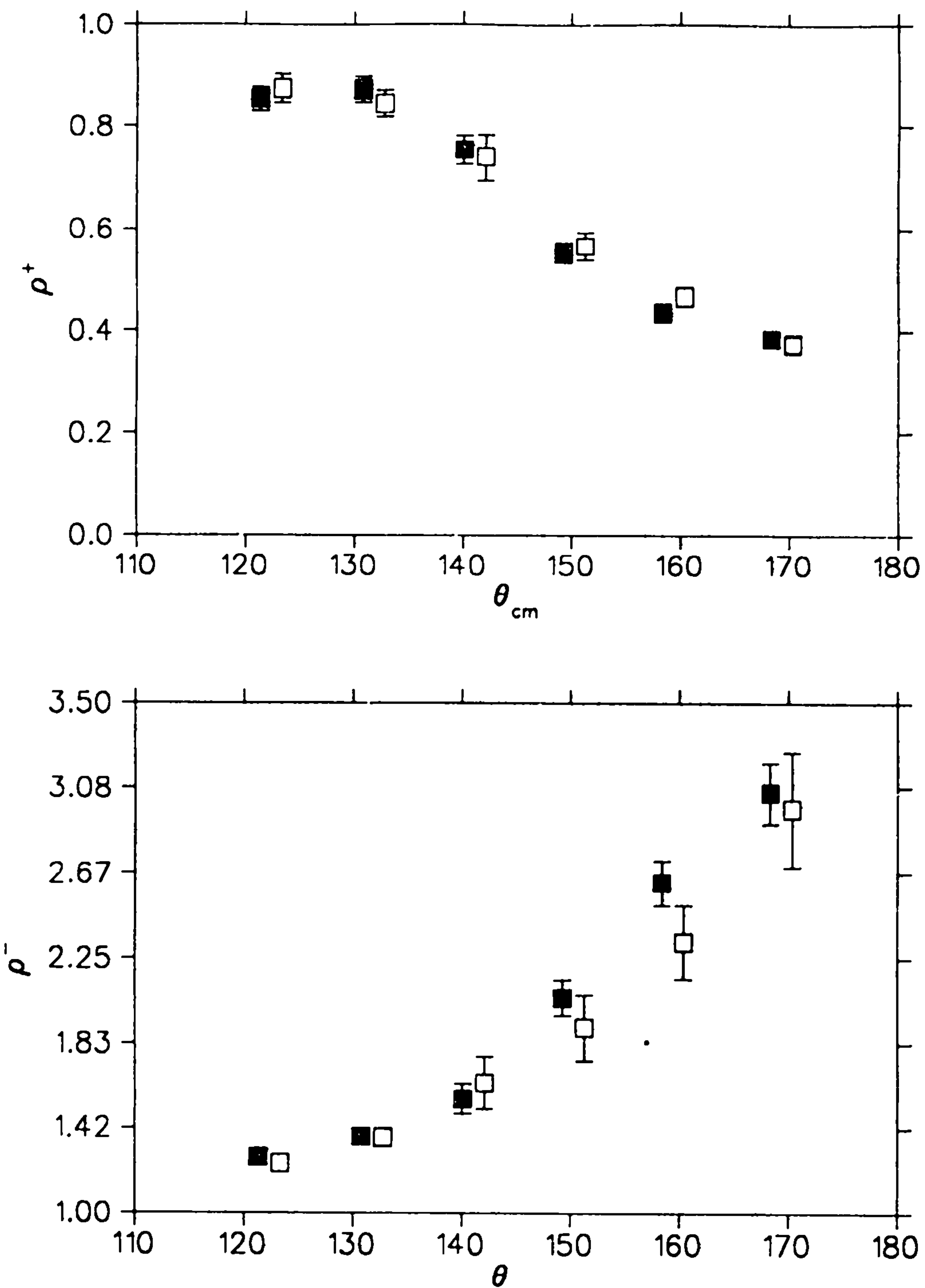

Figure 3.14: Comparison of the scaling and line-background methods, to calculate r_1. The filled squares are from the line-background method, the open squares, from the scale and subtract. Errors from the scale-and-subtract method will be at least as great as from the line-background method.

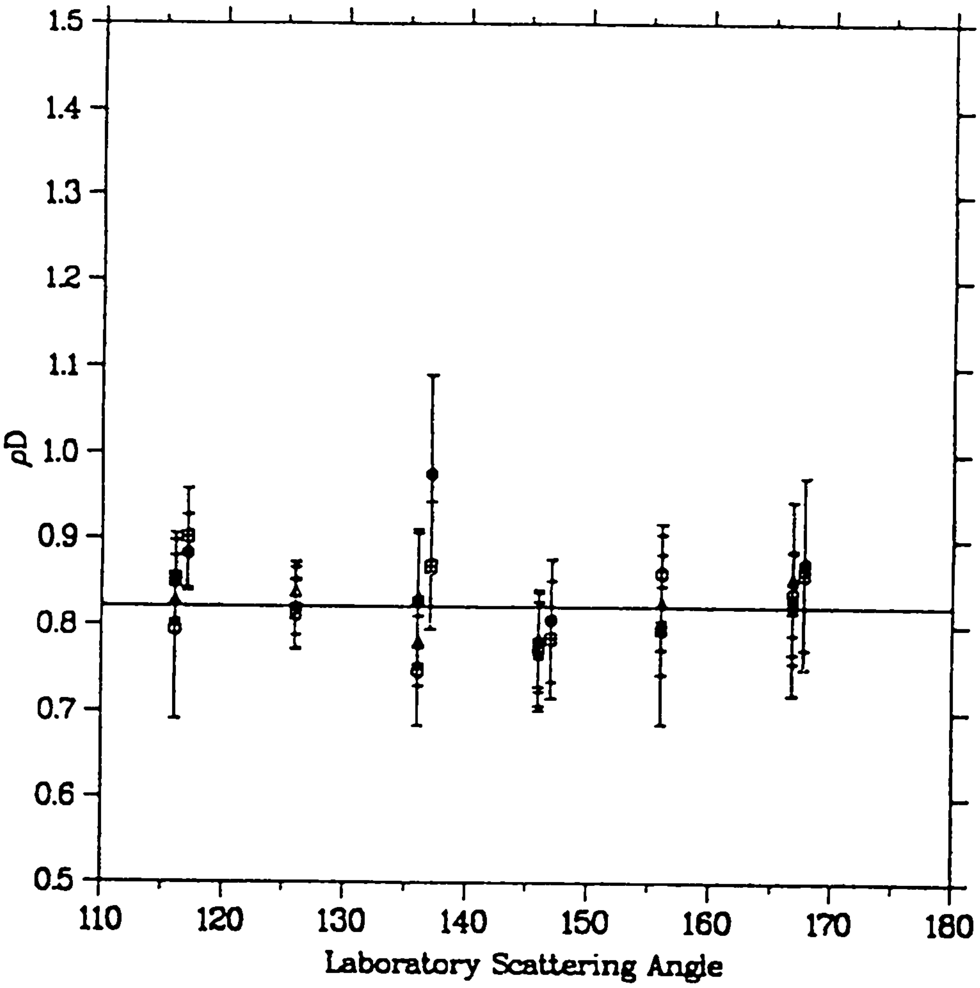

Figure 3.15: ρD calculated several different ways, with statistical errors.

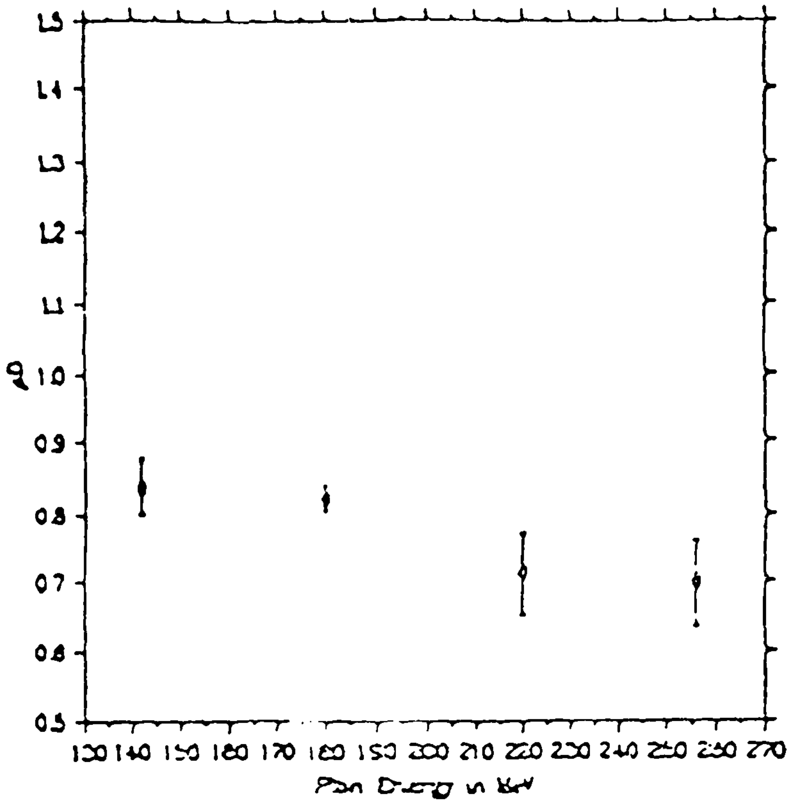

Figure 3.16: ρD at back angles, from this experiment. The errors are statistical; the ion chamber (*norm1*) was used for normalization.

to account for the inconsistencies in their analysis, and they would have had little effect on the weighted average. The effects of these two points are opposite, and so their inclusion would mostly cancel in the average anyway. Figure 3.16 shows ρD at back angles using *norm*1.

The back-angle points at each energy were not averaged, because we expect that ρD will vary with energy, as the fractional pion content in the beam need not be constant with energy.

The other beam monitor was the toroid that monitored the proton beam. Since this monitor always sees the same current regardless of the channel polarity, assuming that the beam is steered consistently, and since we are only looking at scattered pions because particle identification eliminates protons while the relative size of the muon and electron cross sections at these angles means that they do not contribute to the scattering yields, then if the π^+D and π^-D cross sections are equal, ρD calculated with this monitor is really just the π^+ to π^-production ratio for the ^{12}C target in the main beam. Figure 3.17 shows the values of ρD , using the toroid for normalization, at the various points on the excitation function. The same ratio from two other sources are also shown [LAM84] [Gre92]. All of these results are fairly consistent within the error bars shown, which are statistical for this experiment, and include some systematic corrections for the other measurements. Table 3.4 gives these pion production ratios for the current experiment. The value shown for 180 in both Fig. 3.17 and Table 3.4 is the average value from the angular distribution.

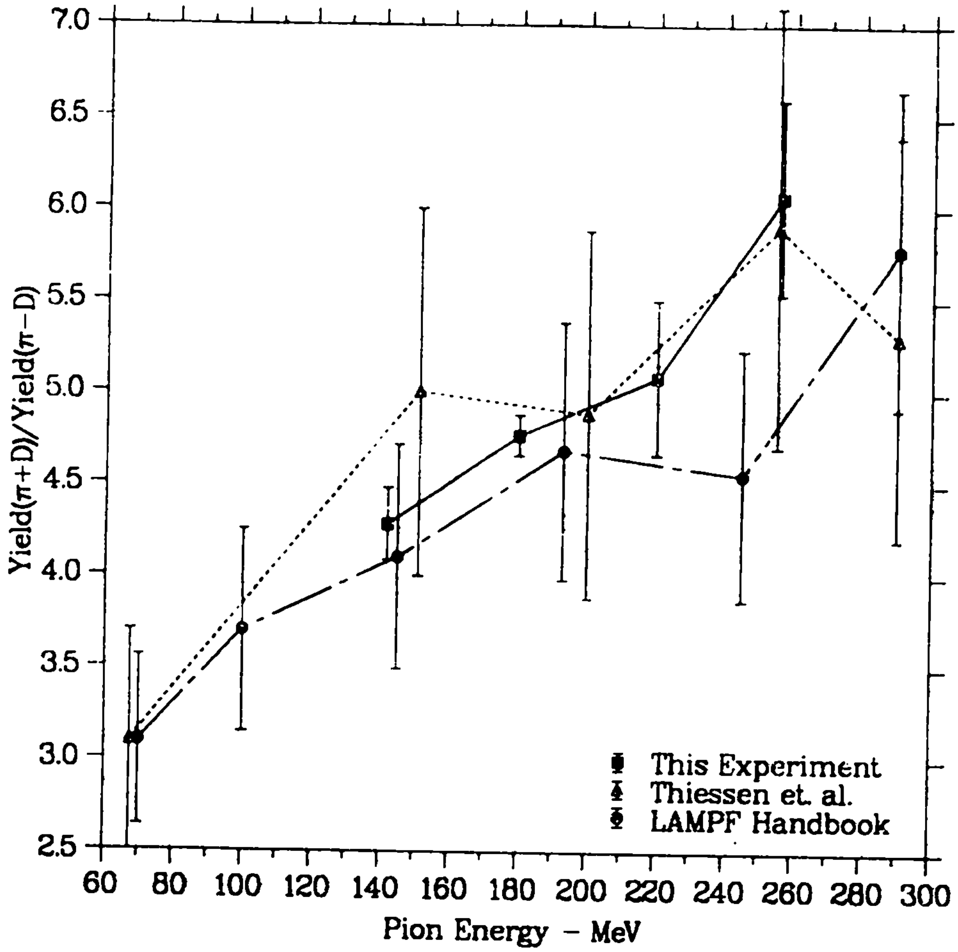

Figure 3.17: EPICS π production ratios. The current experiment is compared with data from the LAMPF Handbook[LAM84] and [Gre92]. Ratios for this experiment are not corrected for any asymmetry in the $\pi \pm D$ cross sections. The errors for this experiment are statistical; some systematic errors are included in the other sets.

$energy(MeV)$	142	180	220	256
π^+/π^-	4.3	4.76	5.1	6.1
$error$	0.2	0.12	0.4	0.5

Table 3.4: Pion production ratios from this experiment.

θ_{lab}	116.0°	126.0°	136.0°	146.2°	156.0°	167.0°
$d\sigma/d\Omega(mb/sr)$	0.523	0.479	0.417	0.369	0.385	0.408
error	0.019	0.019	0.017	0.017	0.017	0.017

Table 3.5: Normalization cross sections extrapolated by interpolation of the data in [Ott85], at 180 MeV.

3.7 Cross Sections

The cross sections require more work than the ratios because it is necessary to use normalization yields and cross sections. Values from Otterman *et. al.* [Ott85] are used here; the cross sections could be normalized to any other set by simply multiplying the quoted cross section by the preferred normalization cross section, and dividing by Otterman's value. The πD cross sections are assumed charge symmetric, that is $\sigma(\pi^+D) = \sigma(\pi^-D)$. Figure 3.18 shows this D data at the energies used. Note that these energies do not exactly overlap with our experimental energies, varying by 1 - 3 MeV.

The cross sections in this region are fairly flat (see Fig. 3.18), linear interpolation was used to get the values used here. A more serious error is that the normalization cross sections are not taken at exactly the same energies as our data; usually they are 1 - 3 MeV lower. Otterman *et. al.* compare their data to older data at similar energies. The older data have large error bars, but the change in differential cross sections due to energy shifts of 1 MeV — 3 MeV are generally less than 5%, distributed on both sides of Otterman's data. Finally, in the cases where the normalization data does not extend to as large an angle as the experimental points, the value of the largest-angle normalization point available is used. All of the normalization data goes to angles within 5° of the experimental data, and considering the flatness of the D data in this region, this introduces only a small uncertainty. A systematic error should be included because of these two approximations. An inspection of the figure shows that an error greater than 5% is unlikely, and so 5% is a conservative systematic error.

Table 3.5 and Table 3.6 show normalization values that were used. Values in the table give the larger error of the two points on either side of the interpolated point. Systematic errors are not included.

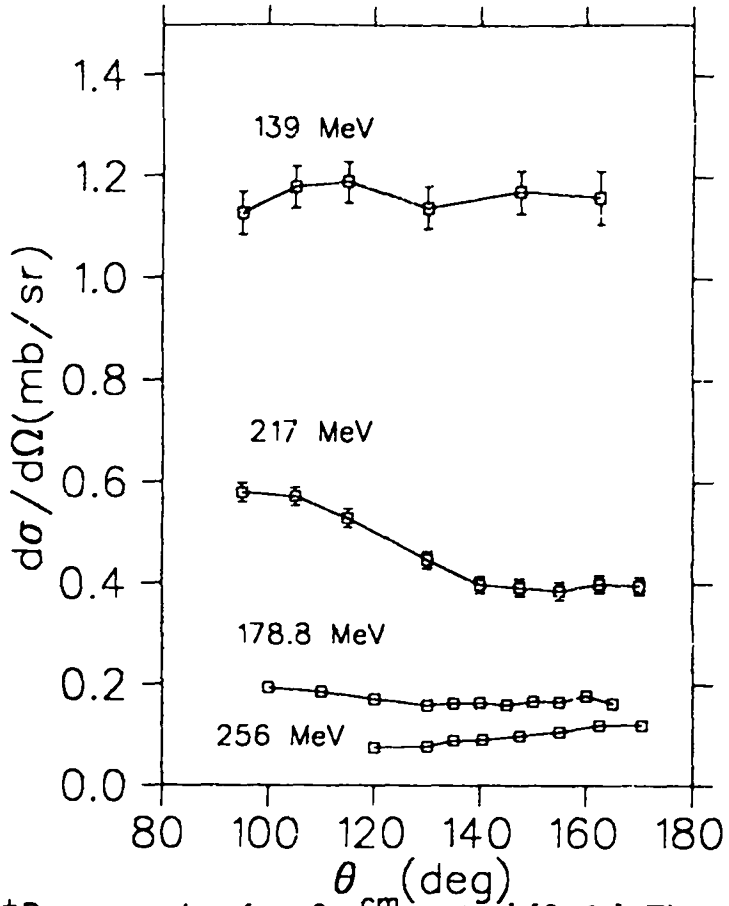

Figure 3.18: π^+D cross sections from Otterman *et. al.* [Ott85]. The normalization cross section values were extracted by linear interpolation. The value from the largest-angle value was used for data points beyond the region of the normalization data.

Energy(MeV)	142	220	256
Lab Angle	162.5	172	173
Cross Sec.(mb/sr)	1.16	0.164	0.12
Error	0.05	0.007	0.007

Table 3.6: Cross sections extrapolated by interpolation of the data in [Ott85], to back angles for the various energies.

3.8 Systematic Errors

There are two important possible sources of systematic error in the cross section measurements and analysis. The target alignment method was by eye, but it was the same for each target, and so, it is likely that on the average all of the targets would be mis-set by the same amount. So, while the target profile as seen by the beam has changed, it has changed both for the experimental and normalization targets. These appear in the numerator and denominator, respectively, and so the change should be symmetric, and should cancel. It is possible that a different shift of experimenters, coming to work in the middle of data taking for a single point, will set the targets systematically different. In this case, the first group of runs will be different from the second group, all at the same experimental point. However, these misalignments are slight, and the major change is in how much of the aluminum wall intersects the incoming beam. The amount of gas in the beam changes only slightly, and since a good deal of the background is eliminated by the Y_{target} cuts, the overall effect should be slight. The most significant systematic error is associated with drawing the straight-line backgrounds. This is a straightforward procedure for the T and ^{3}He runs, but for D it is difficult because the right side of the elastic peak overlaps the break-up region, as the D binding energy is only 2.225 MeV. While a consistent mistake should cancel in ρD since the numerator and denominator have the same shapes, this is not the case for the cross sections. Several trials with moving the background line within reasonable limits suggest that this problem may introduce a 2% - 3% uncertainty into the values of the D yields. Interpolating the normalization cross sections and extending them to larger angles requires a 5% systematic error, as discussed in the previous section. Also discussed there was the deviation of our experimental energies from the normalization data energies. A 3% uncertainty might be included for this as well. Adding (in quadrature) the 2% - 3% mentioned in this paragraph due to background drawing and including as well the 1% error due to the acceptance variation (see Sec. 3.3) gives a total systematic error near 7%.

Systematic errors in the ratios are less of a problem. Since the peaks in the numerator and denominator have the same shapes, it is not necessary to take the entire peak for comparison. Using several peak-slice widths and observing no variations in the ratio is a good check on inconsistencies with the line drawing. A systematic error in the relative ± beam normalizations will show up in r_1 and r_2 but in ρ^+ , ρ^- , and R, this cancels, because there are cancelling polarity values in the numerator and denominator. Likewise, an error in the average value of ρD will affect r_1 and r_2 , but not the others.

Finally, an error in *gasfac* affects all quantities. However, an 0.5% uncertainty has been associated with *gasfac* and included in the quoted errors, so no additional error due to the gas analysis is needed.

Finally, the reported asymmetry in the D cross sections of $\sim -1.5\%$ is not important for the cross sections, which have relatively large errors, and does not affect ρ^+ , ρ^- , and R since they do not require the D values. r_1 and r_2 are affected through the inclusion of ρD ; since ρD is included in the denominator of r_1 and the numerator or r_2 the asymmetry is most noticeable in the *difference* between r_1 and r_2 . r_1 and r_2 will be plotted with and without the πD asymmetry included in ρD in Chap. 4.

3.9 Summary

The final method chosen for the yield analysis is the extrapolated straight-line background. Statistical errors for the yields are $\sqrt{A + \frac{3}{2}B}$, where A and B are the areas in the peak and under the peak respectively, at whatever peak-width was used.

The quoted errors are purely statistical for all of the ratios. For the cross sections, a 7% systematic uncertainty was suggested, in addition to the quoted errors, which include statistical errors and the quoted errors for the normalization cross sections.

Throughout, the πD interaction was assumed charge symmetric.

Chapter 4

Results

4.1 Ratios

The various scattering ratios are plotted and tabulated in this section. Numbers from the three earlier experiments, #546 [Nef90], #905 [Pil91] and #1032 [Pil92],[Ber91] are included. Statistical uncertainties are given, as discussed in Chap. 3. Each ratio table contains a listing of the laboratory scattering angle, the center of mass scattering angle, the momentum transfer in fm^{-2}, the ratios, and the experiment number. All angles are in degrees. The new data from the back-angle experiments are shown as filled squares, the old experiments and the new NSF-dip data are various open symbols.

The charge-symmetric ratios r_1 and r_2 are compared with each other assuming $\sigma(\pi^+D) = \sigma(\pi^-D)$ and again assuming an asymmetry of -1.5% . The R calculation of Gibbs and Gibson, discussed in Sec. 1.7 is overlaid with the old and new data.

4.1.1 The Ratios ρ^+ and ρ^-

It was mentioned in Sec. 1.6.4 that ρ^+ and ρ^- strongly reflect the ratios of the on-resonance, π-nucleon spin-flip amplitudes in the NSF dip region. At 180°, only NSF scattering is possible. In this case, ρ^+ becomes

$$\rho^+ \sim \left| \frac{F_{pT}\ f(\pi^+ p) + 2F_{nT}\ f(\pi^+ n)}{2F_{p^3He}\ f(\pi^+ p) + F_{n^3He}\ f(\pi^+ n)} \right|^2 . \tag{4.1}$$

Assuming that $f(\pi^+ p) \sim 3f(\pi^+ n)$, which is not necessarily a good approximation because at large angles kinematics dictates that all single scattering will be from nucleons with non-zero Fermi momentum, we would expect $\rho^+ = (0.7)^2 \sim 0.5$, if the form factors cancel. Similarly, we expect a value of 2.0 for ρ^-. The measured values are 0.38 and 3.06 for 180 MeV (Fig. 4.1). A + sign on the figure shows these simple predictions.

Increasing or decreasing the pion energy, or increasing the nucleon momentum all correspond to changes in the center-of-mass energy of the π-nucleon system, moving the reaction away from the resonance energy and changing the factor of three between the amplitudes. In Eq. 4.1 we can use $f(\pi^+ p) = 2 \times f(\pi^- p)$ instead of three times, etc. to see how this affects the ratios: the result is an *increase* in ρ^+. Thus moving the reaction away from the resonance energy takes the predicted single-scattering result further from the measured value. Similarly, ρ^- will *decrease* by this estimate, also moving further from the data.

At 220 MeV and 256 MeV, the single back-angle ρ^+ and ρ^- values are consistent with the trends seen at 180 MeV, that is ρ^+ falls and ρ^- rises at back angles to a greater extent than predicted by the simple, single-scattering model (Fig. 4.1). This is not the case at 142 MeV, where the back angle values are 0.8 and 1.3 for ρ^+ and ρ^-, respectively. For this energy, the measured values have a *lesser* fall and rise, respectively, than predicted by the simple model.

In Sec. 1.6.4 it was shown that ρ^+ and ρ^- could be predicted fairly well using a single-scattering impulse approximation and the VPI-phase-shift amplitudes to describe the π-nucleon interaction, in the forward hemisphere. The inputs to the amplitudes are the incoming pion energy and the momentum transfer. Plotting ρ^+ and ρ^- as functions of q^2 shows that the 142 MeV data is consistent with the data for other energies (Fig. 4.2); this emphasizes the π-nucleon scattering amplitudes, not the π-nucleus kinematics as plotting the scattering angle does.

In the forward hemisphere, the NSF dip does not occur at a constant value of q^2, but rather at the value corresponding to 90° in the π-nucleon center-of mass, reflecting the cosine dependence of the NSF p-wave interaction. Figure 4.2 shows that the NSF dip moves to higher values of momentum transfer as the pion kinetic energy increases. In fact the dip shifts as a function of the π-nucleon center-of-mass total energy (this was tested using the Simple Model and changing the center-of-mass energy in the VPI phase-shift analysis), and so it will shift if the nucleon momentum is made non-zero while the pion energy is kept fixed. As was seen in Sec. 1.6.2, to have single scattering at higher momentum transfers, it is

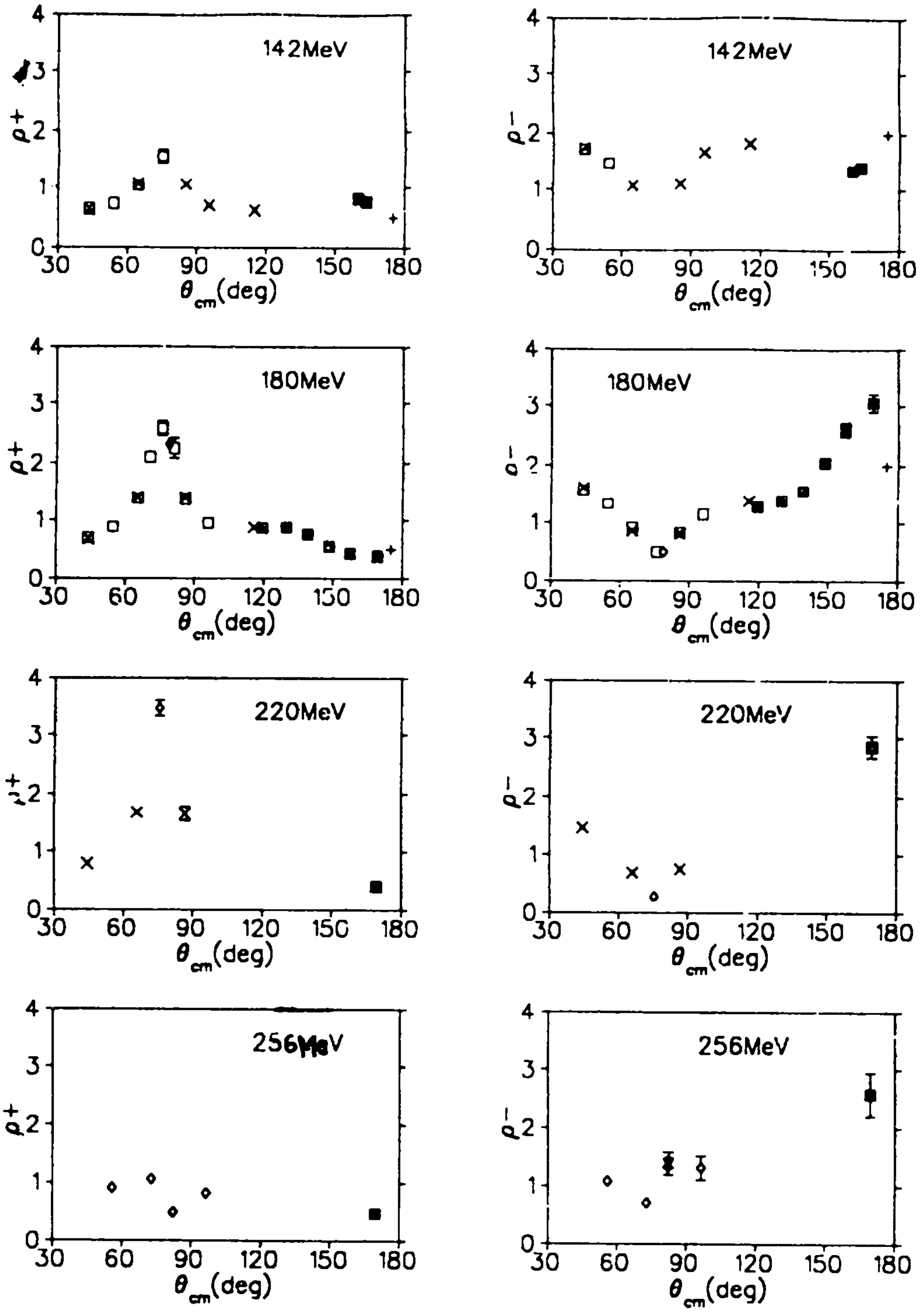

Figure 4.1: ρ^+ and ρ^- from all the experiments. □ Exp. 546 [Nef90], × Exp. 905 [Pil91], ◇ Exp 1032 [Pil92] and [Ber91], filled square, current experiments. The + shows the simple prediction discussed in the text. Except for 142 MeV, all of the back-angle data is consistent with the same back-angle shape as 180 MeV.

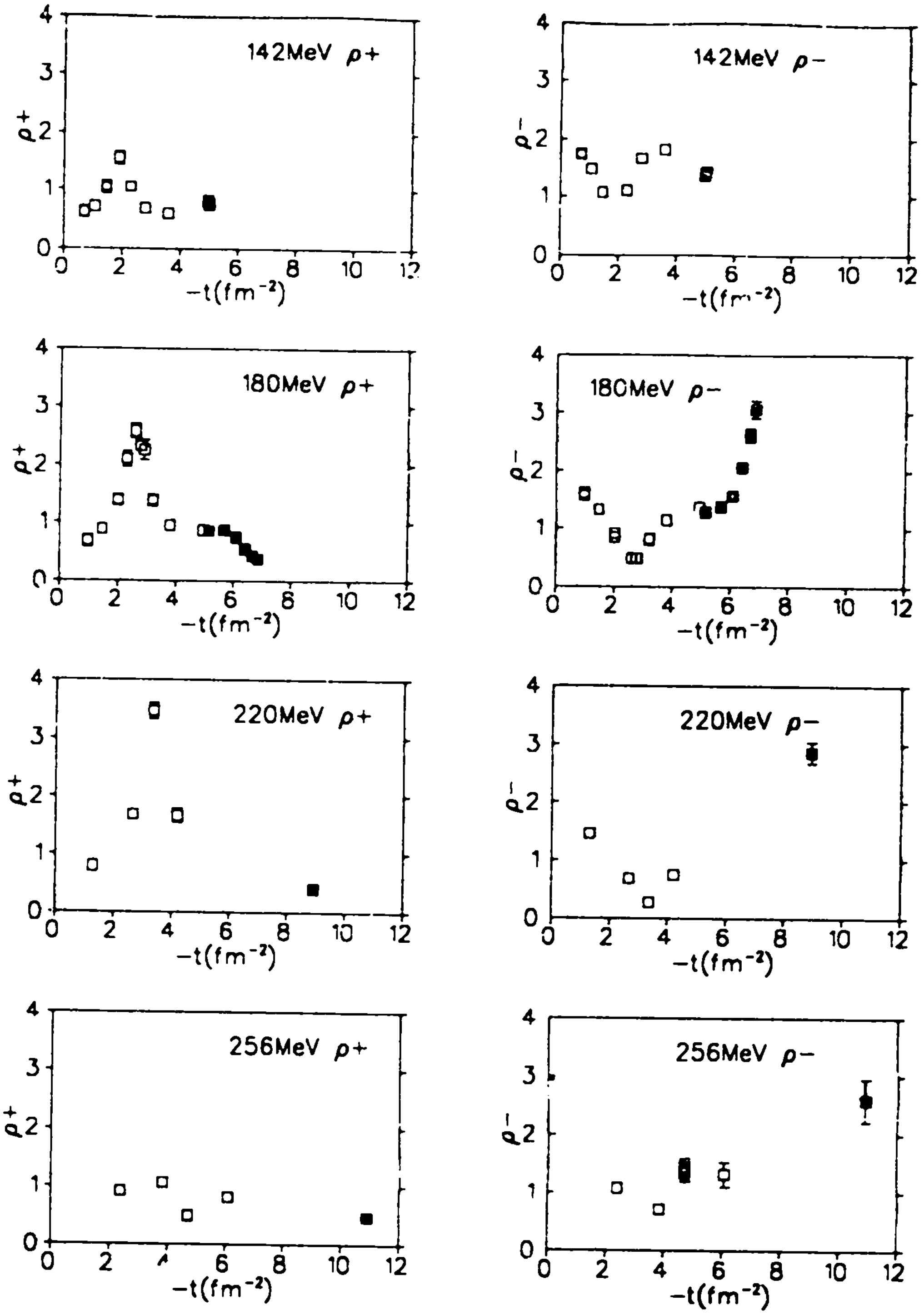

Figure 4.2: ρ^+ and ρ^- as functions of the momentum transfer. The back-angle shapes are consistent at all energies.

necessary to scatter from moving nucleons. Therefore, at back angles and single scattering, the NSF dip moves towards high momentum transfers. However, this dip effect *decreases* ρ^- and *increases* ρ^+ which are opposite the trends needed to explain the data, so one can conclude that this is not the dominant effect at back angles.

As single scattering becomes less likely at high momentum transfers, that is, at larger angles, multiple scattering should become proportionately more important. A very simple argument can predict qualitatively the back-angle trends seen in ρ^+ and ρ^- .

The second order scattering term ('double scattering') is

$$\Sigma_i t_i(q_1) G \Sigma_{j \neq i} t_j(q_2),$$

where q_1 and q_2 are the momenta transferred in the first and second scatter, respectively. Evaluation of this term is not trivial, and will not be attempted here. However, it obviously will be a sum over products of π-nucleon amplitudes. Now assume that each scatter will happen at the resonance energy, that is, assume that the nucleons are infinitely heavy, and consider ρ^+ . The denominator, π^{+3}He, can proceed by scattering first from a proton, and then from another proton, that is, the amplitude contains a product of two amplitudes that are large. Scattering from a proton then a neutron, or a neutron then a proton, is possible, but less likely. The numerator, π^+T, can only proceed by scattering from a proton then a neutron, or a neutron then a proton, that is by products of large and small amplitudes, or by scattering from a neutron then a neutron, the product of two small amplitudes. As the fraction of multiple scattering increases with scattering angle, the denominator increases faster than the numerator, causing an overall decrease in ρ^+ , as is seen in the data. For ρ^- , it is the numerator which can proceed by the product of two large amplitudes, namely $\pi^- n$, and so we expect a steady increase in ρ^- with angle, again as seen in the data. At 142 MeV, single scattering is more likely because of kinematical considerations, as shown in Fig. 1.5.

We should note that in double scattering, spin-flip scattering need not be forbidden on the paired nucleon. For example in π^{+3}He, the pion can flip the spin of one proton in the first interaction, and flip the spin of the second proton in the second interaction. This leaves the protons with opposite spin, still able to occupy the ground state. This could further enhance the scattering from the denominator in ρ^+ and the numerator in ρ^- , and contribute to the measured trends in these ratios.

θ_{lab}	θ_{cm}	-t	ρ^+	ρ^-	Exp.
40.0	43.5	0.7	0.628(0.011)	1.73(0.06)	546
40.0	43.5	0.7	0.617(0.016)	1.754(0.028)	905
50.0	54.2	1.1	0.711(0.019)	1.47(0.05)	546
60.0	64.7	1.5	1.02(0.03)		546
60.0	64.7	1.5	1.054(0.014)	1.066(0.017)	905
70.0	75.1	1.9	1.55(0.12)		546
80.0	85.3	2.3	1.045(0.024)	1.102(0.027)	905
90.0	95.4	2.8	0.689(0.019)	1.666(0.068)	905
110.0	115.0	3.6	0.607(0.015)	1.818(0.052)	905
158.0	160.0	5.0	0.811(0.024)	1.347(0.065)	1064
162.0	163.6	5.0	0.757(0.027)	1.401(0.086)	1064

Table 4.1: ρ^+ and ρ^- 142 MeV

θ_{lab}	θ_{cm}	-t	ρ^+	ρ^-	Exp.
40.0	44.0	1.0	0.692(0.014)	1.56(0.04)	546
40.0	44.0	1.0	0.676(0.009)	1.604(0.021)	905
50.0	54.7	1.5	0.880(0.021)	1.32(0.05)	546
60.0	65.3	2.0	1.37(0.04)	0.909(0.053)	546
60.0	65.3	2.0	1.392(0.021)	0.851(0.016)	905
65.0	70.5	2.3	2.10(0.14)		546
70.0	75.7	2.6	2.58(0.12)	0.496(0.027)	546
73.0	78.8	2.8	2.322(0.070)	0.504(0.023)	1032
75.0	80.9	2.9	2.25(0.17)		546
80.0	85.9	3.2	1.36(0.07)	0.829(0.057)	546
80.0	85.9	3.2	1.388(0.030)	0.812(0.022)	905
90.0	96.0	3.8	0.944(0.036)	1.14(0.07)	546
110.0	115.6	4.9	0.863(0.020)	1.371(0.056)	905
114.0	119.4	5.2	0.85(0.02)	1.28(0.04)	1064
125.0	129.8	5.7	0.87(0.02)	1.38(0.04)	1064
135.0	139.1	6.1	0.75(0.03)	1.56(0.08)	1064
145.0	148.3	6.4	0.55(0.02)	2.05(0.09)	1064
155.0	157.4	6.7	0.44(0.01)	2.62(0.11)	1064
168.0	169.2	6.9	0.38(0.01)	3.06(0.15)	1064

Table 4.2: ρ^+ , ρ^- , 180 MeV

θ_{lab}	θ_{cm}	$-t$	ρ^+	ρ^-	Exp.
40.0	44.4	1.3	0.789(0.015)	1.450(0.024)	905
60.0	65.9	2.6	1.675(0.047)	0.690(0.018)	905
69.0	75.3	3.3	3.466(0.134)	0.273(0.015)	1032
80.0	86.6	4.2	1.657(0.122)	0.755(0.057)	905
168.0	169.3	8.9	0.408(0.035)	2.86(0.18)	1064

Table 4.3: ρ^+ and ρ^- 220 MeV

θ_{lab}	θ_{cm}	$-t$	ρ^+	ρ^-	Exp.
50.0	55.7	2.4	0.91(0.04)	1.08(0.05)	1032
66.0	72.7	3.9	1.06(0.06)	0.71(0.05)	1032
75.0	82.1	4.7	0.50(0.04)/0.490(0.040)	1.44(0.14)/1.330(0.139)	1032
89.0	96.2	6.1	0.82(0.08)	1.31(0.21)	1032
168.0	169.4	10.9	0.478(0.035)	2.59(0.37)	1064

Table 4.4: ρ^+ and ρ^- 256 MeV. The two entries at 75° are from two separate analyses.

4.1.2 The Ratios r_1 and r_2

In the backward hemisphere, the charge-symmetric ratios r_1 and r_2 show similar behavior for all energies (see Fig. 4.3). At 180 MeV, assuming that $\sigma(\pi^+ D) = \sigma(\pi^- D)$, they cross each other around 100°; r_2 is ~ 1.0 in the backward hemisphere, r_1 climbs quickly to about 1.1 and stays there (see Fig. 4.4). The back-angle points at the other energies show the same trends as those at 180 MeV: r_1 is greater than 1.0, and r_2 approximately equals 1.0.

In single-scattering, we expect both r_1 and r_2 to be larger than 1.0, because of the proton repulsion in ^{3}He, which makes the form factor for ^{3}He less than that of T at each momentum-transfer value. The lack of structure is not surprising, as the π-nucleon amplitudes are smooth and non-zero in this region, see Fig. 1.1, and the form factors are well behaved as well up to the 8 fm^{-2} covered at 180 MeV (see Fig. 1.7).

Smith *et. al.* report a -1.5% asymmetry in the D cross sections at back angles, with uncertainties at the different angles near 0.6%. That is

$$\frac{\sigma(\pi^- D) - \sigma(\pi^+ D)}{\sigma(\pi^- D) + \sigma(\pi^+ D)} = -0.015,$$

or, $\sigma(\pi^+ D)/\sigma(\pi^- D) = 1.03$. To include this result, we must divide the values of ρD, used to calculate r_1 and r_2, by 1.03. Including the asymmetry increases the separation between r_1 and r_2 in the backward hemisphere (see Fig. 4.4). Including the asymmetry in the forward hemisphere would decrease the separation between r_1 and r_2; however, the asymmetry data exists only for angles greater than 60° and so the correction has not been applied to the forward-hemisphere ratios.

The Simple Model impulse approximation done in Sec. 1.6.4 gives large variations in r_1 and r_2 in both hemispheres for small variations in δ_r and δ_o. However, no combination of δ_r and δ_o made the ratios cross over as seen in the data.

The data are not inconsistent with the simple multiple-scattering picture given in the previous section. Consider r_2, for example. The numerator, π^-T, will be dominated, in double scattering, by the product $\pi^- n \times \pi^- n$, while the denominator, π^{+3}He, will be dominated by $\pi^+ p \times \pi^+ p$, so that the double-scattering systematics will be the same in both the numerator and denominator. As multiple scattering becomes more important with increasing angle (or increasing momentum transfer), we would expect a similar additive correction for both numerator and denominator, and no great variations in the ratio. As the nucleons in ^{3}He are slightly more separated than those of T, we would expect the multiple scattering from ^{3}He to be suppressed somewhat; thus both single and double scattering should tend to increase r_2 above 1.0. The same arguments indicate that r_1 should be above 1.0 as well.

The crossover of r_1 and r_2 must be considered whether or not the πD asymmetry is included in their determinations. The arguments in this section suggest that r_1 and r_2 are very sensitive to the nucleon distribution, and therefore to the form factors. Nevertheless, the inclusion of the more sophisticated form factors of Barshay and Seghal [Bar85] in the simple model did not produce such a cross over (see Sec. 1.7). In the calculation of Gibbs and Gibson, inclusion of a Coulomb term in the potential produced a similar crossover [WRG92], although it is not seen in the calculation by Kim *et. al.* (Sec. 1.7), using a similar term, but not proton-proton repulsion in ^{3}He.

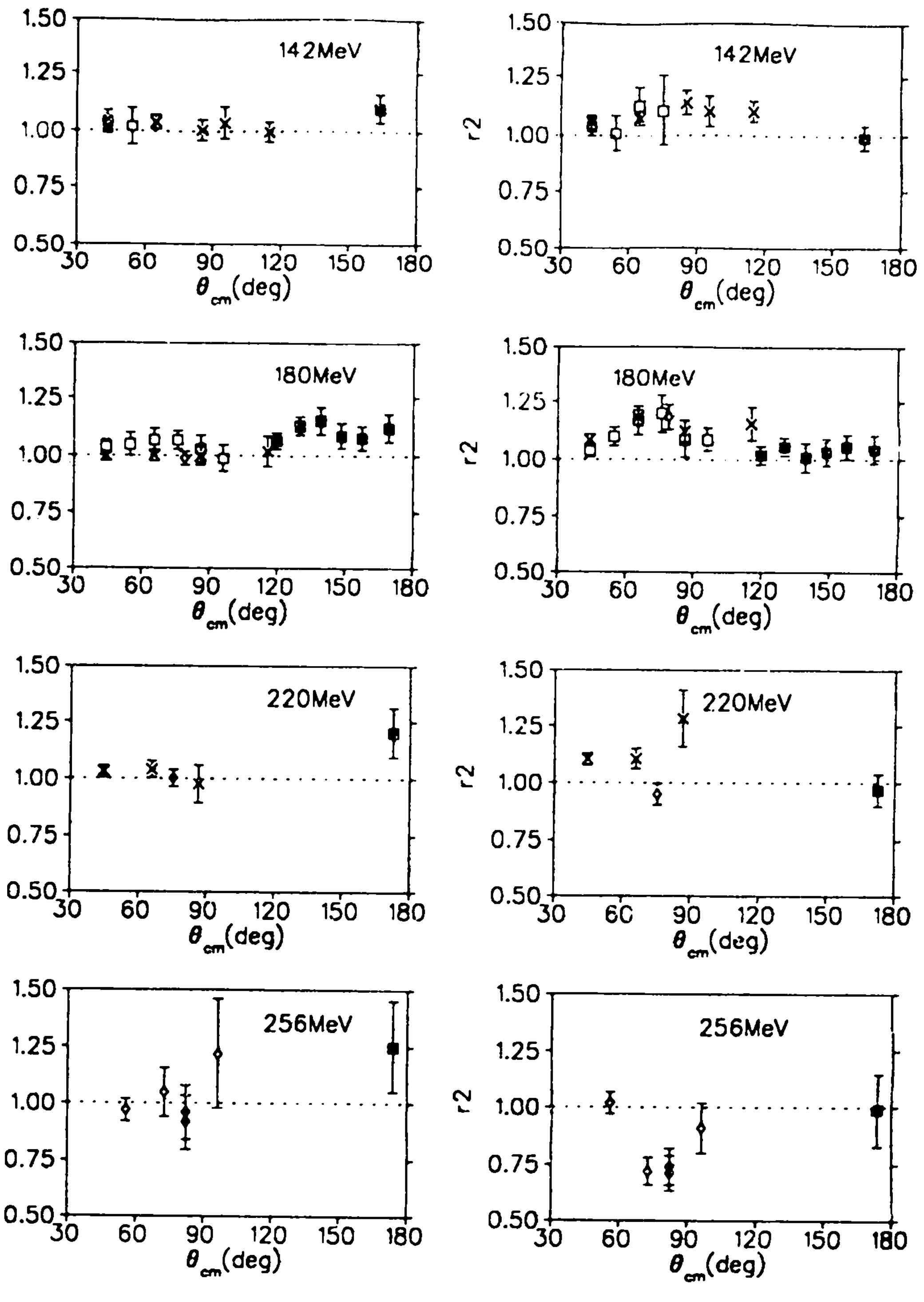

Figure 4.3: r_1 and r_2 from all of the experiments. □ Exp. 546 [Nef90], × Exp. 905 [Pil91], ◇ Exp 1032 [Pil92] and [Ber91], filled square, current experiments. The far-back point at each energy is consistent with the shape at 180 MeV.

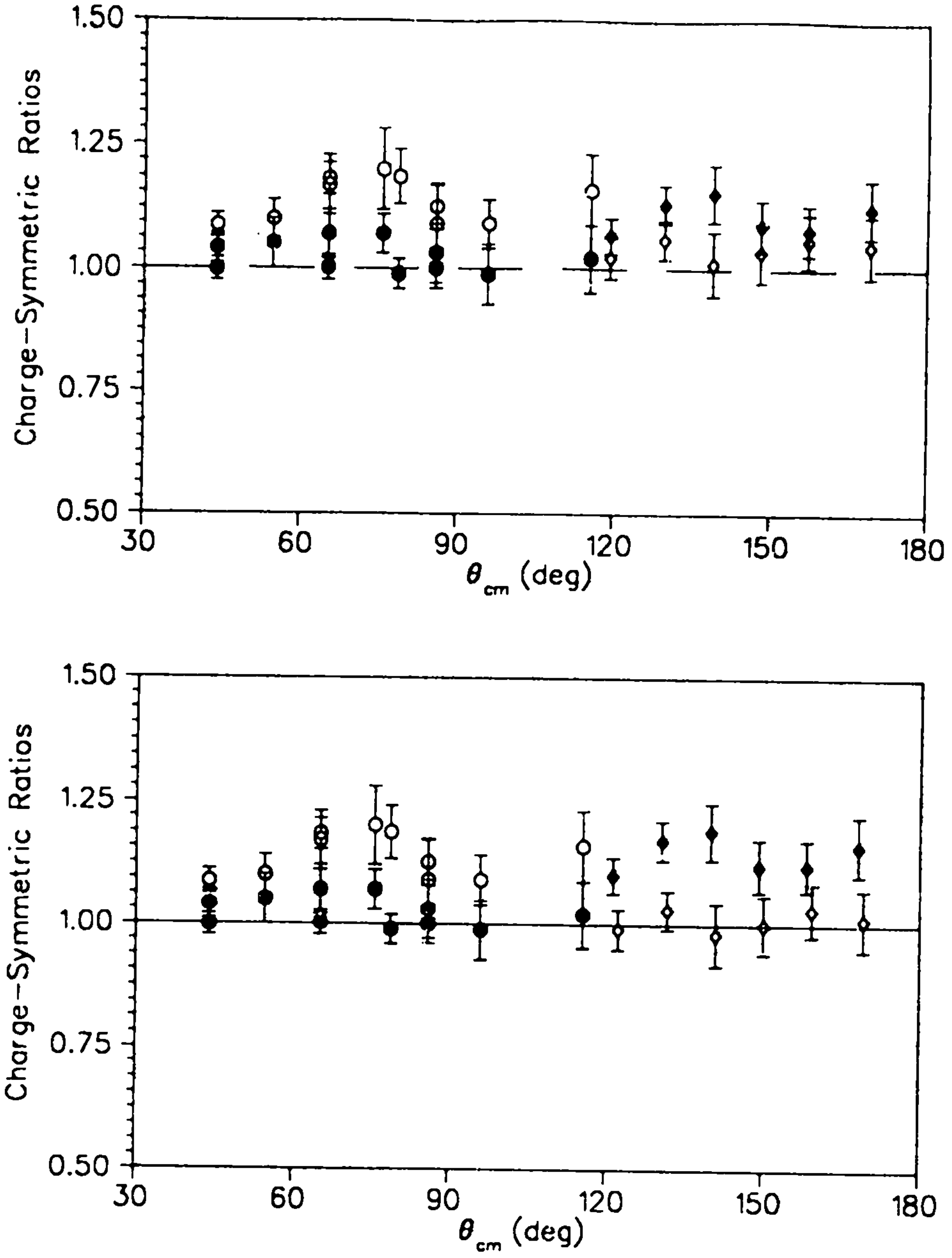

Figure 4.4: Compare r_1 and r_2. Open symbols r_1, closed r_2. The circles are the old data, the diamonds the current results. *Top:* Using the original ρD, that is assuming $\pi^+D = \pi^-D$. *Bottom:* With ρD changed in the backward hemisphere only to reflect the asymmetry reported by [Smi88].

θ_{lab}	θ_{cm}	-t	r_1	r_2	Exp.
40.0	43.5	0.7	1.04(0.05)	1.04(0.04)	546
40.0	43.5	0.7	1.021(0.027)	1.060(0.029)	905
50.0	54.2	1.1	1.02(0.08)	1.01(0.08)	546
60.0	64.7	1.5		1.13(0.08)	546
60.0	64.7	1.5	1.041(0.030)	1.079(0.030)	905
70.0	75.1	1.9		1.11(0.15)	546
80.0	85.3	2.3	1.007(0.046)	1.143(0.050)	905
90.0	95.4	2.8	1.038(0.069)	1.106(0.065)	905
110.0	115.0	3.6	0.997(0.045)	1.107(0.044)	905
158.0	160.0	5.0	1.10(0.06)	0.99(0.06)	1064
162.0	163.6	5.0	1.08(0.05)	1.01(0.06)	1064

Table 4.5: r_1 and r_2 142 MeV

θ_{lab}	θ_{cm}	-t	r_1	r_2	Exp.
40.0	44.0	1.0	1.04(0.03)	1.04(0.03)	546
40.0	44.0	1.0	0.998(0.022)	1.087(0.025)	905
50.0	54.7	1.5	1.05(0.05)	1.10(0.04)	546
60.0	65.3	2.0	1.07(0.05)	1.17(0.06)	546
60.0	65.3	2.0	1.002(0.025)	1.183(0.031)	905
70.0	75.7	2.6	1.07(0.04)	1.20(0.08)	546
73.0	78.8	2.8	0.989(0.030)	1.186(0.054)	1032
80.0	85.9	3.2	1.03(0.06)	1.09(0.08)	546
80.0	85.9	3.2	1.000(0.040)	1.126(0.047)	905
90.0	96.0	3.8	0.988(0.057)	1.09(0.05)	546
110.0	115.6	4.9	1.020(0.068)	1.159(0.072)	905
114.0	119.4	5.2	1.07(0.04)	1.02(0.04)	1064
125.0	129.8	5.7	1.13(0.04)	1.06(0.04)	1064
135.0	139.1	6.1	1.15(0.06)	1.01(0.07)	1064
145.0	148.3	6.4	1.09(0.05)	1.03(0.06)	1064
155.0	157.4	6.7	1.08(0.05)	1.06(0.06)	1064
168.0	169.2	6.9	1.12(0.06)	1.05(0.06)	1064

Table 4.6: r_1 , r_2 180 MeV

θ_{lab}	θ_{cm}	$-t$	r_1	r_2	Exp.
40.0	44.4	1.3	1.033(0.026)	1.107(0.026)	905
60.0	65.9	2.6	1.042(0.038)	1.109(0.045)	905
69.0	75.3	3.3	1.002(0.039)	0.915(0.048)	1032
80.0	86.6	4.2	0.976(0.084)	1.283(0.123)	905
168.0	169.3	8.9	1.21(0.11)	0.97(0.07)	1064

Table 4.7: r_1 and r_2 220 MeV

θ_{lab}	θ_{cm}	$-t$	r_1	r_2	Exp.
50.0	55.7	2.4	0.97(0.05)	1.02(0.03)	1032
66.0	72.7	3.9	1.05(0.11)	0.72(0.06)	1032
75.0	82.1	4.7	0.96(0.12)/0.917(0.119)	0.74(0.08)/0.711(0.077)	1032
89.0	96.2	6.1	1.22(0.24)	0.91(0.011)	1032
168.0	169.4	10.9	1.25(0.20)	0.99(0.16)	1064

Table 4.8: r_1 and r_2 256 MeV. The two entries at 75° are from two separate analyses.

4.1.3 The Superratio

R is the ratio that should be the most independent of first-order Coulomb effects, with the exception of the form factor variation due to p-p repulsion. At 180 MeV, where the angular distribution is complete, *R* does not seem to exhibit any structure in the backward hemisphere; rather it is fairly flat with a value of around 1.15 (see Fig. 4.5). It may be that the seeming dip around 120° is a real structure, but the error bars are not inconsistent with a smoother shape. At any rate, the value is consistently above 1.0, to at least two σ at all points. All of the optical-model calculations mentioned in Chap. 1 show a value near 1.0 in the region around 100°, where these experiments have the least data. However, considering the large error bars on the 115° point from the previous experiments, the data is not inconsistent with a dip there, followed by a slowly rising function at back angles. This shape was predicted by Gibbs and Gibson. Their curve for the prediction $\delta_e = -0.03$fm follows the data well, (Fig. 4.6).

The other energies have similar values for the lone back-angle points. Each is above 1.0, although the difference is less than two σ.

Note the surprising value at 256 MeV from Exp. 1032 [Pil92] [Ber91] at the NSF dip, and the seeming dip there to about 1.0 at 220 MeV. In addition, there is a single NSF dip point taken at 295 MeV [Ber91], which has not been plotted as there are no points at this energy in the current experiments, whose value is less than 1.0 as well. Possible explanations for these below-one results at the NSF dip will not be considered here, but we note that at this energy we are off the Δ resonance, and the simple pictures given for ρ^+ and ρ^- (Sec. 1.6.4), whose product make *R*, is no longer adequate.

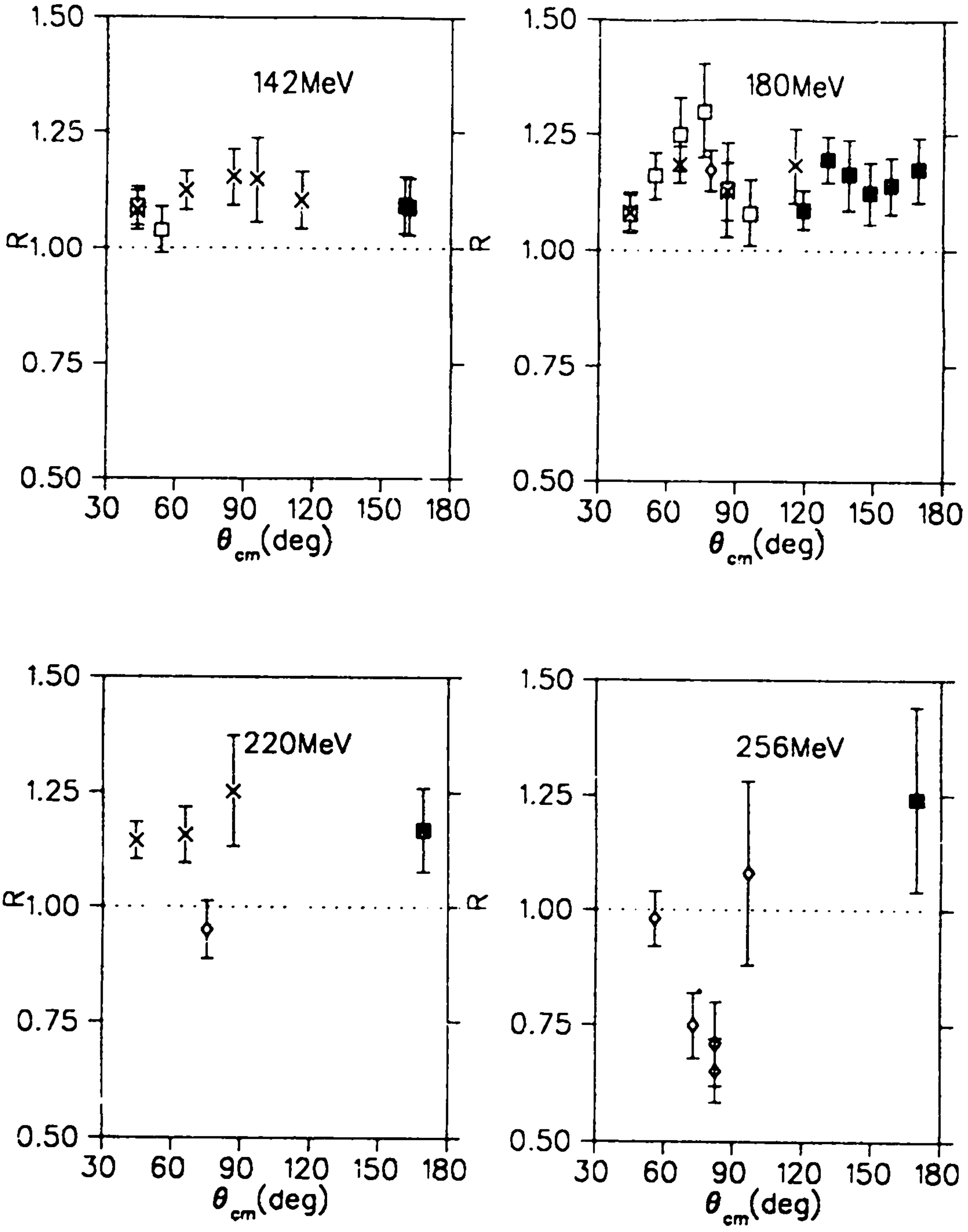

Figure 4.5: R for all the experiments. □ Exp. 546 [Nef90], × Exp. 905 [Pil91], ◇ Exp 1032 [Pil92] and [Ber91], filled square, current experiments.

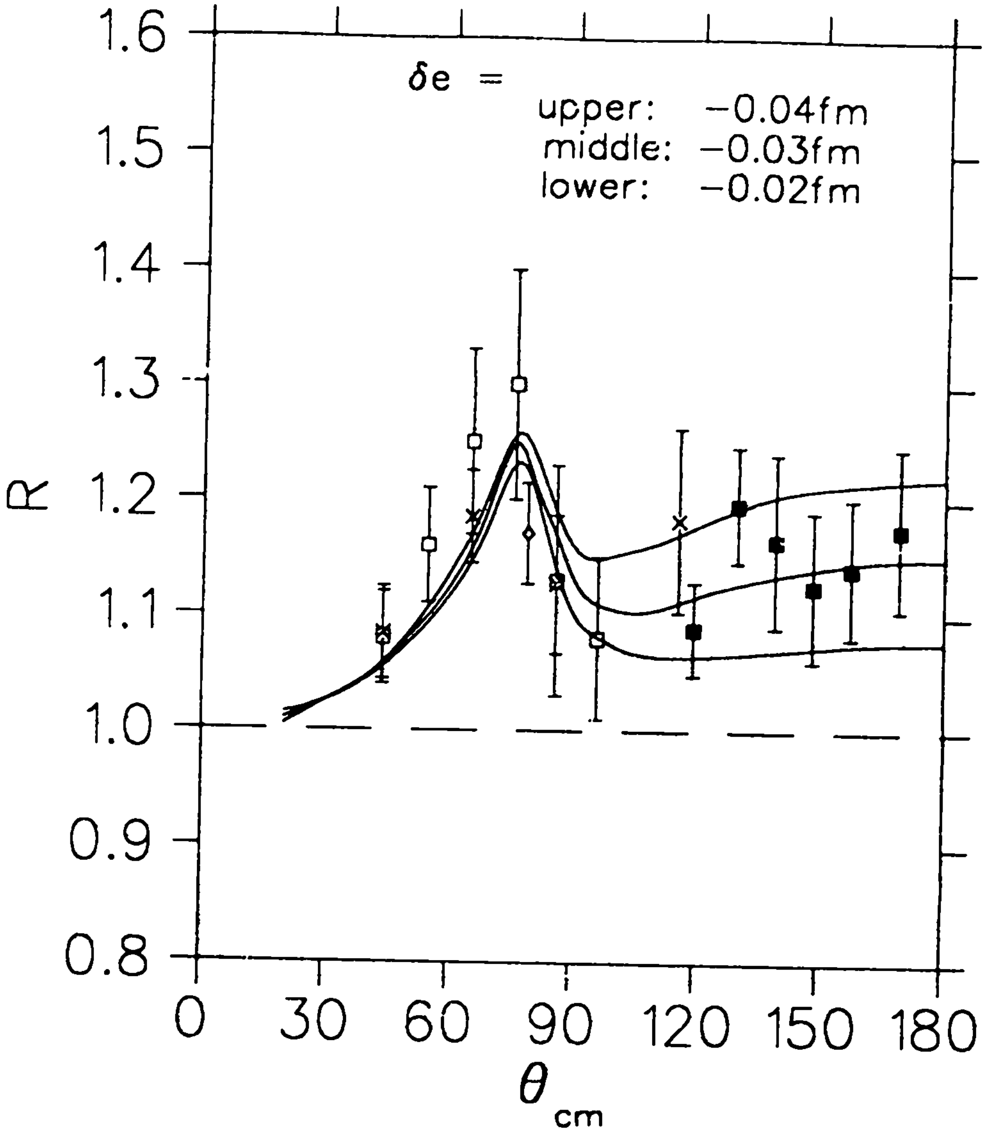

Figure 4.6: R at 180 MeV and the calculation by Gibbs and Gibson discussed in sec. 1.7. The three curves are for three values of δ_e . □ Exp. 546 [Nef90], × Exp. 905 [Pil91], ◇ Exp 1032 [Pil92] and [Ber91], filled square, current experiments.

θ_{lab}	θ_{cm}	-t	R	Exp.
40.0	43.5	0.7	1.09(0.04)	546
40.0	43.5	0.7	1.082(0.039)	905
50.0	54.2	1.1	1.04(0.05)	546
60.0	64.7	1.5		546
60.0	64.7	1.5	1.123(0.038)	905
70.0	75.1	1.9		546
80.0	85.3	2.3	1.152(0.061)	905
90.0	95.4	2.8	1.148(0.086)	905
110.0	115.0	3.6	1.104(0.064)	905
158.0	160.0	5.0	1.09(0.06)	1064
162.0	163.6	5.0	1.09(0.06)	1064

Table 4.9: R at 142 MeV. The blank entries are points where data was taken for r_2 but not r_1 during experiment 546, thus R cannot be computed there

θ_{lab}	θ_{cm}	-t	R	Exp.
40.0	44.0	1.0	1.08(0.04)	546
40.0	44.0	1.0	1.084(0.039)	905
50.0	54.7	1.5	1.16(0.05)	546
60.0	65.3	2.0	1.25(0.08)	546
60.0	65.3	2.0	1.185(0.036)	905
70.0	75.7	2.6	1.30(0.10)	546
73.0	78.8	2.8	1.171(0.044)	1032
80.0	85.9	3.2	1.13(0.10)	546
80.0	85.9	3.2	1.127(0.057)	905
90.0	96.0	3.8	1.08(0.07)	546
110.0	115.6	4.9	1.183(0.078)	905
114.0	119.4	5.2	1.09(0.04)	1064
125.0	129.8	5.7	1.20(0.05)	1064
135.0	139.1	6.1	1.16(0.08)	1064
145.0	148.3	6.4	1.13(0.06)	1064
155.0	157.4	6.7	1.14(0.06)	1064
168.0	169.2	6.9	1.18(0.07)	1064

Table 4.10: R 180 MeV

θ_{lab}	$\theta_{c.m.}$	$-t$	R	Exp.
40.0	44.4	1.3	1.144(0.037)	905
60.0	65.9	2.6	1.156(0.055)	905
69.0	75.3	3.3	0.946(0.062)	1032
80.0	86.6	4.2	1.251(0.121)	905
168.0	169.3	8.9	1.17(0.09)	1064

Table 4.11: R at 220 MeV

θ_{lab}	θ_{cm}	$-t$	R	Exp.
50.0	55.7	2.4	0.98(0.06)	1032
66.0	72.7	3.9	0.75(0.07)	1032
75.0	82.1	4.7	0.71(0.09)/0.652(0.068)	1032
89.0	96.2	6.1	1.08(0.20)	1032
168.0	169.4	10.9	1.24(0.20)	1064

Table 4.12: R 256 MeV. The two values at 75° are from separate analyses.

4.2 Cross Sections

The cross sections are the least accurate of the data obtained in these measurements, but their error bars are all small enough to make them useful. Data is plotted and tabulated from the previous and current experiments, with open and filled symbols, respectively. The plotted and tabulated data are all in the π-nucleus center-of-mass system. All cross sections are plotted and tabulated assuming there is *no* asymmetry in πD; that is all are normalized to $\sigma(\pi^+ D)$).

The most striking detail of the back-angle results is the pairing of the charge-symmetric pairs, π^+T and $\pi^-{}^3He$, and π^-T and $\pi^+{}^3He$. In single scattering, the former set is dominated by odd-nucleon scattering at resonance energies. At 180 MeV, these two cross sections are rather flat over the range of the current experiments, coming down from the small hump following the NSF dip. Together they make up r_1 , which is the charge-symmetric ratio that deviates from 1.0 at back angles. r_1 , and the cross section data, show that π^+T is consistently greater that $\pi^-{}^3He$ in this region. In single scattering, this is to be expected in the absence of significant structure due to the π-nucleon amplitudes, because of the larger T form factor.

The other two cross sections make up r_2 . They show a sharp rise between 140° and 180°. In single scattering, these cross sections are mostly even-nucleon scattering at resonance energies, and therefore primarily non-spin-flip. Since r_2 goes to 1.0 here, there is no difference in the scattering between the two, so it seems that the size differences are not important.

The back-angle rise in the cross sections of π^-T and $\pi^+{}^3He$ are responsible for the increase in ρ^- and the decrease in ρ^+ seen over those angles. It has been suggested in this chapter that a simple double-scattering model could explain the respective rise and fall in these ratios, and that such systematics would not be inconsistent with the mostly-flat backangle shapes of r_1 and r_2 . However, such a model cannot explain the *increase* in the π^-T and $\pi^+{}^3He$ cross sections at back angles. Figure 4.7 shows our elastic T-scattering data and ${}^4He$-scattering data from Brinkmoeller *et. al.* [Bri91]. To the extent that π^-T emphasizes scattering from the paired nucleons at the resonance energy, π^-T is similar to the scattering from ${}^4He$, which has all nucleons in spin pairs. The 180 MeV ${}^4He$ data is represented by the fourth dotted line from the top, directly above the π^-T data (filled squares). The similarity is obvious. Note especially that both the ${}^4He$ and π^-T data have a dip near 6 fm^{-2} momentum transfer. A similar shape is seen in the bottom dotted curve, which represents ${}^4He$ scattering at 240 MeV, but at higher momentum transfer. Also note the hump in the ${}^4He$ data between 3 and 6 fm^{-2}. One might expect to see a similar hump in the π^-T data, considering its other similarities with the ${}^4He$ data; it would be interesting to see whether the hump appears in the π^+T data. In the calculation of Gibbs and Gibson (Fig. 4.11), there is a variation in this region between the two.

Including the πD asymmetry numbers makes all of the π^-cross sections smaller by 3%, decreasing the π^-T – $\pi^+{}^3He$ gap slightly and increasing the gap

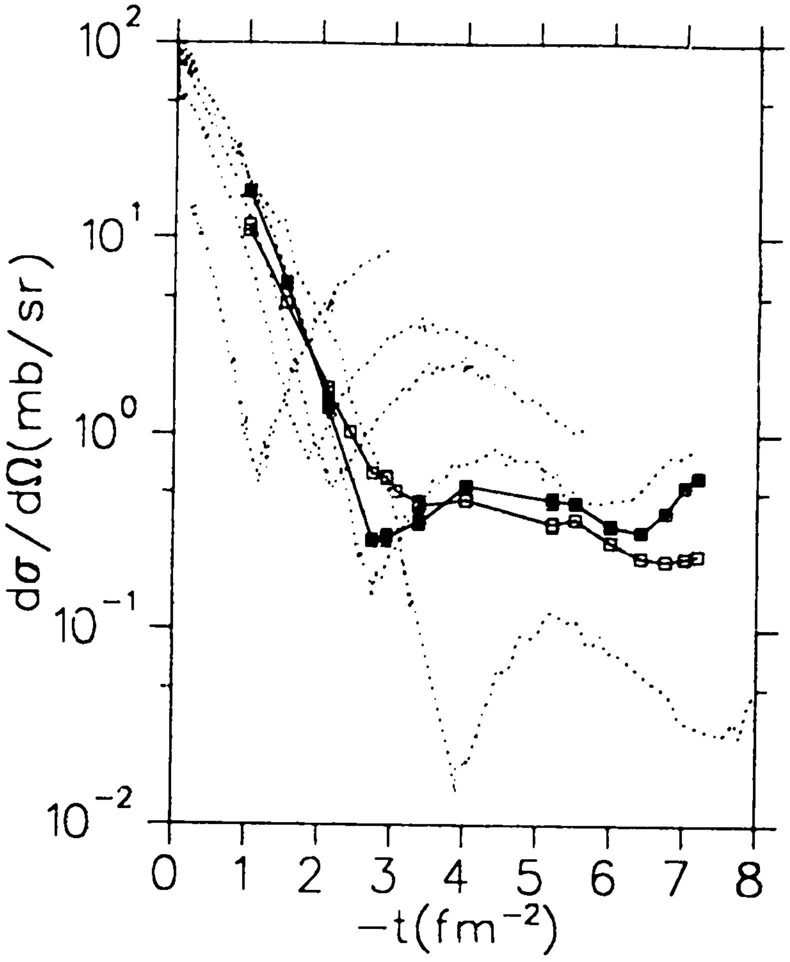

Figure 4.7: *Dotted:* π^{+4}He scattering at 90, 130, 150, 180 and 240 MeV, from top to bottom. *Filled squares:* π^-T at 180 MeV. *Open squares:* π^+T at 180 MeV. The dotted lines connect data points from [Bri91], but the actual points are not shown.

between π^+T and π^{-3}He. That is, r_1 is increased and r_2 is decreased (see Fig. 4.4).

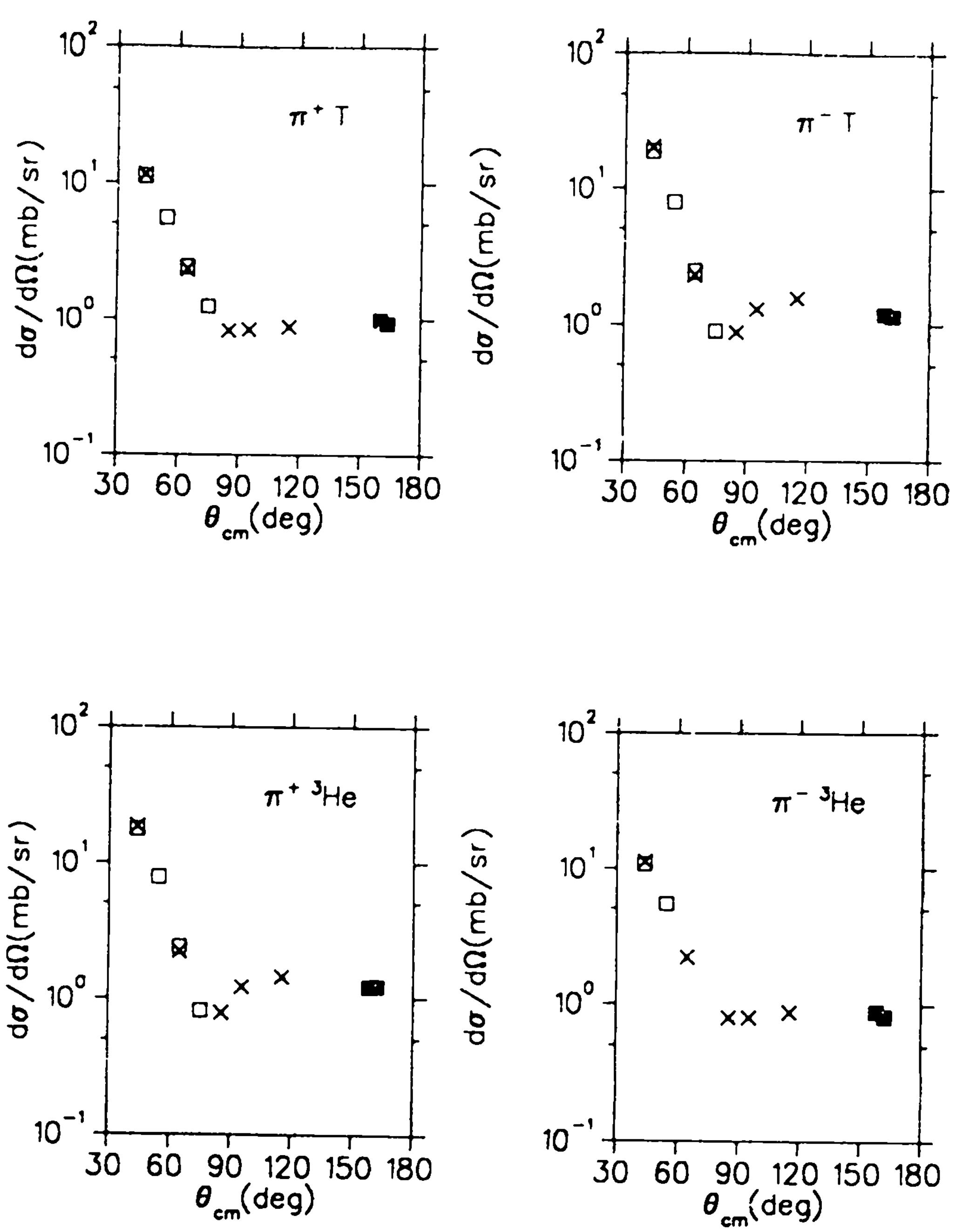

Figure 4.8: Cross sections at 142 MeV. □ Exp. 546 [Nef90], × Exp. 905 [Pil91], filled square, current experiments.

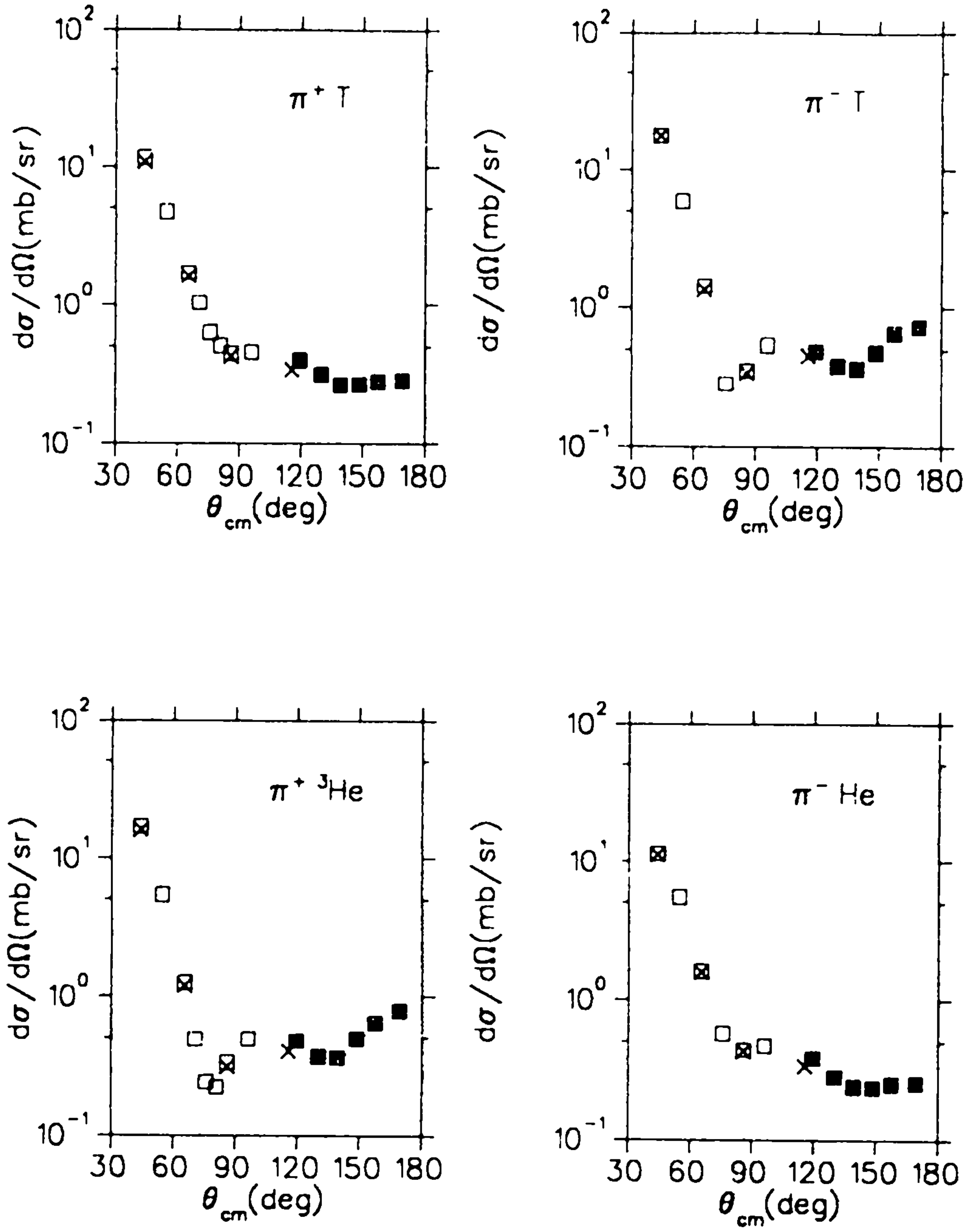

Figure 4.9: Cross sections at 180 MeV. □ Exp. 546 [Nef90], × Exp. 905 [Pil91], ◇ Exp 1032 [Pil92] and [Ber91], filled square, current experiments.

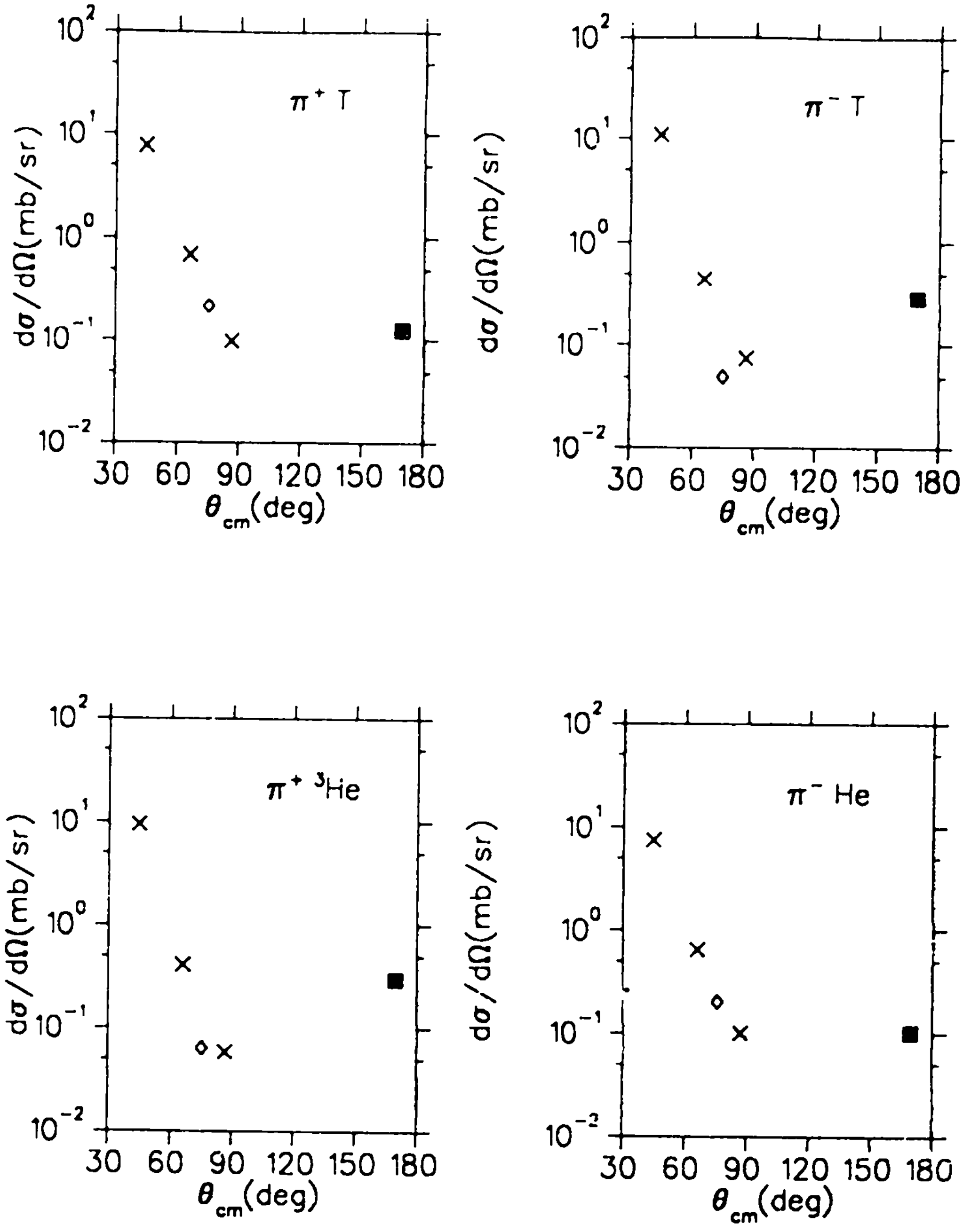

Figure 4.10: Cross sections at 220 MeV. × Exp. 905 [Pil91], ◇ Exp. 1032 [Pil92] [Ber91], filled square current experiments.

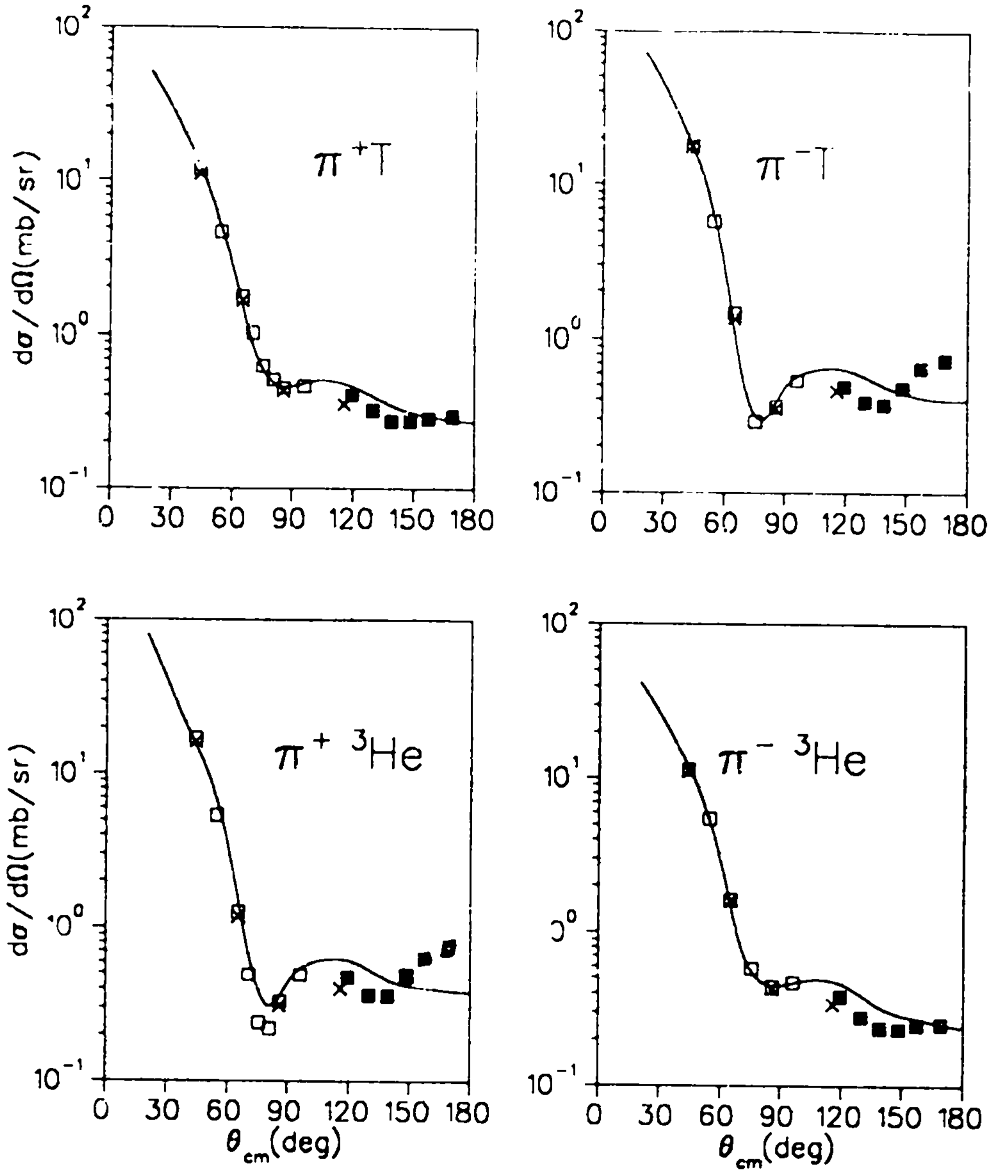

Figure 4.11: The data plotted with calculations by Gibbs and Gibson, which were discussed in sec. 1.7. The results are good in the NSF dip region. At back angles, the calculation is too low for the r_1 constituents $\pi^- T$ and π^{+3}He, and the rise in the r_2 constituents $\pi^+ T$ and π^{-3}He is not reproduced.

θ_{cm}(dg)	$d\sigma(\pi^+ T)$	$d\sigma(\pi^{+3}He)$	$d\sigma(\pi^- T)$	$d\sigma(\pi^{-3}He)$	Exp.
43.6	11.1(0.4)	17.7(0.6)	18.4(0.6)	10.7(0.5)	546
43.6	11.36(0.63)	18.41(1.02)	19.64(1.09)	11.24(0.62)	905
54.2	5.5(0.2)	7.8(0.3)	7.9(0.6)	5.4(0.4)	546
64.7	2.43(0.10)	2.39(0.10)	2.5(0.2)		546
64.7	2.34(0.18)	2.22(0.17)	2.36(0.19)	2.22(0.18)	905
75.1	1.25(0.07)	0.81(0.07)	0.9(0.1)		546
85.3	0.81(0.05)	0.78(0.05)	0.88(0.05)	0.80(0.05)	905
95.4	0.83(0.07)	1.21(0.09)	1.33(0.11)	0.80(0.07)	905
114.9	0.87(0.07)	1.44(0.12)	1.61(0.14)	0.88(0.08)	905
160.0	0.99(0.06)	1.21(0.07)	1.21(0.08)	0.89(0.06)	1064
163.6	0.93(0.05)	1.22(0.07)	1.17(0.06)	0.83(0.06)	1064

Table 4.13: Differential cross sections, 142 MeV, in the center-of mass. Cross sections are in mb/sr.

θ_{cm}(dg)	$d\sigma(\pi^+ T)$	$d\sigma(\pi^{+3}He)$	$d\sigma(\pi^- T)$	$d\sigma(\pi^{-3}He)$	Exp.
44.0	11.7(0.3)	17.0(0.4)	17.6(0.4)	11.3(0.3)	546
44.0	10.88(0.55)	16.11(0.81)	17.71(0.88)	11.12(0.55)	905
54.7	4.7(0.2)	5.4(0.2)	5.9(0.2)	5.5(0.2)	546
65.3	1.72(0.04)	1.25(0.04)	1.46(0.06)	1.61(0.07)	546
65.3	1.63(0.08)	1.18(0.07)	1.36(0.08)	1.59(0.09)	905
70.5	1.03(0.05)	0.49(0.03)			546
75.7	0.63(0.02)	0.24(0.01)	0.29(0.02)	0.58(0.01)	546
78.8					1032
80.9	0.51(0.03)	0.22(0.02)			546
85.9	0.45(0.01)	0.33(0.02)	0.36(0.02)	0.44(0.02)	546
85.9	0.43(0.03)	0.31(0.02)	0.35(0.02)	0.43(0.03)	905
96.0	0.46(0.02)	0.49(0.02)	0.54(0.02)	0.47(0.02)	546
115.6	0.35(0.03)	0.40(0.02)	0.46(0.04)	0.34(0.02)	905
119.4	0.41(0.02)	0.47(0.02)	0.49(0.02)	0.38(0.02)	1064
129.8	0.32(0.02)	0.37(0.02)	0.39(0.02)	0.28(0.02)	1064
139.1	0.27(0.02)	0.36(0.02)	0.37(0.02)	0.24(0.02)	1064
148.3	0.27(0.02)	0.49(0.04)	0.48(0.04)	0.23(0.02)	1064
157.4	0.29(0.02)	0.64(0.05)	0.66(0.05)	0.25(0.02)	1064
169.2	0.29(0.02)	0.78(0.05)	0.74(0.05)	0.25(0.02)	1064

Table 4.14: Differential cross sections, 180 MeV, in the center-of mass. Cross sections are in mb/sr.

θ_{cm}(dg)	$d\sigma(\pi^+T)$	$d\sigma(\pi^{+3}He)$	$d\sigma(\pi^-T)$	$d\sigma(\pi^{-3}He)$	Exp.
44.4	7.66(0.45)	9.51(0.56)	10.73(0.62)	7.44(0.45)	905
65.9	0.69(0.05)	0.41(0.03)	0.45(0.04)	0.65(0.05)	905
75.3					1032
86.6	0.097(0.006)	0.059(0.005)	0.076(0.005)	0.101(0.008)	905
169.3	0.12(0.01)	0.30(0.02)	0.29(0.02)	0.10(0.01)	1064

Table 4.15: Differential cross sections, 220 MeV, in the center-of mass. Cross sections are in mb/sr.

θ_{cm}(dg)	$d\sigma(\pi^+T)$	$d\sigma(\pi^{+3}He)$	$d\sigma(\pi^-T)$	$d\sigma(\pi^{-3}He)$	Exp.
55.7	1.6(0.1)	1.70(0.1)	1.8(0.1)	1.7(0.1)	1032
72.7	0.12(0.01)	0.12(0.02)	0.081(0.008)	0.12(0.01)	1032
82.1	0.038(0.005)	0.08(0.01)	0.055(0.007)	0.041(0.007)	1032
96.2	0.031(0.003)	0.037(0.004)	0.034(0.004)	0.0250(0.004)	1032
169.4	0.052(0.005)	0.11(0.01)	0.105(0.01)	0.041(0.006)	1064

Table 4.16: Differential cross sections, 256 MeV, in the center-of mass. in mb/sr.

Chapter 5

Summary and Conclusion

The scattering cross sections and their ratios measured in this work extend the picture of pion scattering from $A = 3$ nuclei in the region of the Δ_{33} resonance to angles near 170° in the laboratory. The scattering ratios and cross sections show consistent trends and match up well with forward-angle data.

In the backward hemisphere, $\rho^+ \equiv d\sigma(\pi^+\mathrm{T})/d\sigma(\pi^{+3}\mathrm{He})$ falls and $\rho^- \equiv d\sigma(\pi^-\mathrm{T})/d\sigma(\pi^{-3}\mathrm{He})$ rises with angle to a much greater extent than predicted by a single-scattering impulse approximation. The exception is at 142 MeV, the only point with energy below the π-nucleon resonance energy of 180 MeV; however plotting these data as a function of momentum transfer squared shows that the data are consistent over all of the energies measured. ρ^+ and ρ^- are *not* charge symmetric. It was shown in Sec. 1.6.4 that their forward-hemisphere values could be well predicted by the single-scattering, fixed-scatterer, impulse model described there. The only important input to that calculation was the values of the π-nucleon amplitudes. That calculation fails in the backward hemisphere. It was suggested in Sec. 4.1.1. that as kinematical considerations dictated a proportionately greater role for multiple scattering in the backward hemisphere, the trends in ρ^+ and ρ^- might be explained by a very simple double-scattering picture. This picture cannot explain the back-angle cross sections and so can not be correct as given. Nevertheless, multiple scattering looks like a very important part of the back-angle shapes for ρ^+ and ρ^- . Conversely, these two ratios may provide a good test for multiple-scattering calculations, especially if they remain as insensitive to nucleon-distribution considerations as they were in the forward hemisphere. Indeed, it seems wiser to test these theories in regions far from the NSF dip, with its various sensitivities, and come back to the dip region when all the parts of the scattering problem are worked out.

$r_1 \equiv d\sigma(\pi^+\mathrm{T})/d\sigma(\pi^{-3}\mathrm{He})$ and $r_2 \equiv d\sigma(\pi^-\mathrm{T})/d\sigma(\pi^{+3}\mathrm{He})$ are the nominally charge-symmetric ratios. In the forward hemisphere, r_2 is greater than 1.0 and r_1 is ~ 1.0. r_1 and r_2 should be less sensitive to the π-nucleon amplitudes because of their charge-symmetric nature. Thus, we expect them to be more sensitive to the form factors. The hump in r_2 in the region of the NSF dip is a complicated function of amplitude changes and nuclear distributions. Small variations in the inputs to simple calculations can cause large variations in that region. It may be possible to reproduce the hump with many different parameter combinations, and so it is important that they be based on physical arguments. In the simple calculation shown in Sec. 1.6.4, as well as in the potential-interaction calculation of Gibbs and Gibson discussed in Sec. 1.7, small variations in the parameters describing the spatial nucleon distribution make large variations in the backward hemisphere. In the latter calculation, this is shown in the values of the Superratio, which is the product or r_1 and r_2 . Once again, one might expect to use the backward-hemisphere data to work out a part of the scattering problem, in this case the form-factor inputs, before coming back to the more difficult dip region.

The smooth, straightforward shapes of r_1 and r_2 that result from including the πD asymmetry data make calculations in the backward hemisphere very attractive. However, we should note that such effects as the interaction-energy difference in the numerator and denominator due to Coulomb acceleration of the incoming pions by the charged protons (two in the denominator and one in the numerator) must not be overlooked in even basic calculations of r_1 and r_2 , as their deviations from 1.0 are only on the order of ten percent, so that small effects could be a significant fraction of the result.

The Superratio ($R = r_1 \times r_2$) has been well predicted by Gibbs and Gibson, based on a potential-interaction model that includes the Coulomb interaction. The back-angle magnitude of $\sim$ 1.15 and overall smoothness are the same features that describe its constituents r_1 and r_2 . The πD asymmetry has no effect on R because the D normalizations cancel. The authors' R curve for $\delta_p = -0.03$ fm and $\delta_n = 0.035$ fm is a good match to the data.

The cross sections behave as predicted by the single-scattering impulse approximation up to about 80°. At very large angles, the two r_2 members, π^-T and π^{+3}He rise steeply. This rise is what causes the complementary fall and rise in ρ^+ and ρ^- , and is not predicted by the various potential-model calculations discussed in Sec. 1.7. Comparison with ^{4}He scattering data shows a similar rise, and suggests that the fact that the primary scattering is from spin-paired nucleons is somehow behind this trend. As mentioned above, a correct multiple-scattering calculation may be important in describing this part of the data.

The ^{4}He data shows a distinct hump following the NSF dip in the region where the data is missing for T and ^{3}He, around 100°. As this is the region of the possible crossover in r_1 and r_2 , as well as the region where some of the potential model calculations of R return to 1.0, filling in this area would be a worthwhile effort. It would also be interesting to see whether there are any differences in this region between the two cross sections with the rise at the farthest-back angles, π^-T and π^{+3}He, and the two which were flatter there, π^+T and π^{-3}He.

The back-angle data does not allow any simple new statements about nuclear-charge-symmetry breaking. The Superratio calculation of Gibbs and Gibson gives neutron radii which are most closely approximated in a nuclear model that includes some asymmetry in the nucleon-nucleon amplitudes beyond the Coulomb interaction [Gib91]. Including the πD asymmetries of Smith *et. al.* [Smi88], another nominally-charge-symmetric system, enhances the r_1 r_2 separation. A calculation that matched the ratio data would lend credence to the reported πD asymmetry, and so to NCSB.

In short, to make definitive statements about charge symmetry, a very good calculation of the nominally-charge-symmetric ratios r_1 and r_2 is needed. The calculation must include a fairly complete treatment of all of the scattering details, including multiple scattering, as the measured effect is small. At that time, we shall see if the uncertainties associated with r_1 and r_2 allow a precise enough determination of the scattering parameters to permit precise conclusions about NCSB. However, at the least we might expect this process to lead to a good understanding of the Coulomb contributions to the problem, and yield the precise shape of the form factors. In that case, more precise re-measurements of some points to constrain certain parameters would be warranted.

In Sec. 1.8, the goals of this work were listed as: providing a back-angle extension to the πT and π^3He scattering data base, testing the back-angle predictions discussed in Sec. 1.7, and exploring the relative CSB by the non-spin-flip amplitudes, in a region where the spin-flip amplitudes are ~ 0. The data exist now, and so the first goal is met. The angular distribution is a poor match for the predictions of r_1 r_2 and R in [Kim86], [Kim87] and [Bar85], however the match is good with the predictions in [Gib91]. In the latter, the three curves given by the authors in their R prediction span the data, however the error bars are not really small enough to absolutely choose between these curves. Finally, it appears that CSB, which was seen in r_2 in the forward hemisphere, is seen with similar magnitude in r_1 in the backward hemisphere, and therefore that a simple distinction regarding CSB between the spin-flip and non-spin-flip amplitudes is not possible.

Bibliography

[Alb82] M. Albu, T. Angelescu, M. Antonova, F. Balestra, S. Bossolasco, *et. al.*, Instituto Nazionali Di Fisica Nucleare, Laboratori Nazionali di Frascati, internal publication: LNF-82/27(R), (1982)

[AmUp] J. F. Amann, Backangle Development Log Book, Unpublished

[Arn85] R. A. Arndt, J. M. Ford, and L. D. Roper, Phys. Rev. D **32**, 1085 (1985)

[Ate81] L. G. Atencio, J. F. Amann, R. L. Boudrie and C. L. Morris, Nucl. Instrum. Methods 187, 381 (1981)

[Bar85] S. Barshay and L. M. Sehgal Phys. Rev. C **31**, 2133 (1985)

[Bec82] D. H. Beck, J. Asai, and D. M. Skopik, Phys. Rev. C **25**, 1152 (1982)

[Ber] B. L. Berman, Private Communication

[Ber91] B. L. Berman, D. B. Barlow, W. J. Briscoe, K. S. Dhuga, S. J. Greene, S. K. Matthews, A. Mokhtari, B. M. K. Nefkens, C. Pillai, J. W. Price, I. Slaus *et. al.*, Pion Scattering from T and ^{3}He, Proceedings of the International Workshop on the Interaction of Pions with Nuclei, (1991), Penyscola, Spain, *and* K. S. Dhuga, private communication.

[Bin78] F. Binon, P. Duteil, M. Gouanere, L. Hugon, J. Jansen, J. -P. Lagnaux, H. Palevsky, J. -P. Peigneux, M. Spighel, and J. -P. Stroot, Nucl. Phys **A298**, 499 (1978)

[Bri86] W. J. Briscoe, B. L. Berman, A. Mokhtari, M. F. Taragin, B. M. K. Nefkens, C. Pillai, J. A. Wightman, G. Kim, D. B. Barlow, M. E. Sadler and D. Isenhower and Ivo Slaus, LAMPF proposal #1064, (1986)

[Bri87] W. J. Briscoe, B. L. Berman, K. S. Dhuga, A. Mokhtari, M. F. Taragin, D. Zubanov, R. Caress, N. J. Nicholas, S. K. Matthews, C. Pillai, B. M. K. Nefkens, D. B. Barlow, J. Price, R. Kessler, M. E. Sadler, D. Isenhower, S. Greene, B. Gibson, W. Gibbs, LAMPF proposal #1155, (1987)

[Bri89] W. J. Briscoe and B. H. Silverman, Phys Rev C **39**, 282 (1989)

[Bri91] B. Brinkmoller. C. L. Blilie. D. Dehnhard. M. K. Jones, G. M. Martinez S. K. Nanda. S. M. Sterbenz. Yi-Fen Yen. L. G. Atencio. S. J. Greene. C. L. Morris. S. J. Seestrom. G. R. Burleson. K. S. Dhuga. J. A. Faucett R. W. Garnett. K. Maeda. C. Fred. Moore. S. Mordechai. A. Williams. S. H. Yoo. L. C. Bland Phys. Rev. C **44**. 2031 (1991)

[Bur86] G. R. Burleson. W. B. Cottingame. K. S. Dhuga. J. A. Faucett. C. P. Fontenla. J. F. Amann. R. L. Boudrie. S. J. Greene. C. L. Morris. N. Tanaka. Z. F. Wang. D. Yusnukis. M. Brown. R. R. Kiziah. E. C. Milner. C. F. Moore. S. Mordechai. D. Oakley. P. A. Seidl. C. L. Blilie. D. Dehnhard. S. Nanda. S. J. Seestron-Morris. J. D. Zumbro. and K. Maeda. Nucl Instrum Methods **A247**. 327 (1986)

[Bri89] W. J. Briscoe and B. H. Silverman. Phys Rev C **39**. 282 (1989)

[Col65] H. Collard. R. Hofstadter. E. B. Hughes. A. Johansson. M. R. Yearian,R. B. Day. and R. T. Wagner. Phys. Rev. **138**. B 57 (1965)

[Cot84] W. B. Cottingame. G. R. Burleson. M. Brown. R. Kiziah. D. Oakley. C. Milner. P. Seidl and N. Tanaka Los Alamos Report: LA-10201-MS. (1984) Unpublished

[Eis80] J. M. Eisenberg and D. S. Koltun
Theory of Meson Interactions with Nuclei John Wiley and Sons. New York. (1980)

[Gib91] W. R. Gibbs and B. F. Gibson. Phys. Rev. C **43**. 1012 (1991)

[Jus85] F. P. Juster. S. Auffret. J. M Cavedon. J. C. Clemens. B. Frois. D. Goutte. M. Huet. P. Leconte. J. Martino. Y. Mizuno. X. H. Phan. S. Platchkov. S. Williamson. I. Sick. Physical Review Letters **55**. 2261 (1985)

[Kal80] J. Kallne. J. F. Davis. J. S. McCarthy. R. C. Minehart. R. R. Whitney. R. L. Boudrie. J. McClelland. A. Stetz. Phys. Rev. Letters **45**. 517 (1980)

[Ker59] A. Kerman. H. McManus. and R. Thaler. Ann. Phys. **8**. 551 (1959)

[Kim86] Y. T. Kim. M. Krell and L. Tiator. Phys Lett **B172**, 287 (1986)

[Kim87] Kr. T. Kim. Y. E. Kim. R. H. Landau . Phys. Rev. C **36**, 2155 (1987)

[Kis55] L. S. Kisslinger. Phys. Rev. **98**. 761 (1955)

[LAM84] LAMPF Users' Handbook. Available from the LAMPF visitor's center. (1984. rev.)

[Lan75] R. Landau, Ann. Phys. **92**, 205 (1975)

[Mal] H. R. Maltrud, Private Communication

[McC77] J. S. McCarthy, I. Sick and R. R. Whitney, Phys. Rev. C **15**, 1396 (1977)

[Mor82] C. L. Morris, Nucl. Instrum. and Methods, **196**, 263 (1982)

[Mor85] C. L. Morris, J. F. Amann, R. L. Boudrie, N. Tanaka, S. J. Seestrom, L. C. Bland, P. A. Seidl, R. Kiziah, and S. J. Greene, Nucl. Instrum. and Methods, **A238**, 94 (1985)

[Nef90] B. M. K. Nefkens, W. J. Briscoe, A. D. Eichon, D. H. Fitzgerald, A. Mokhtari, J. A. Wightman, and M. E. Sadler, Phys. Rev. C **41**, 2770 (1990)

[Ott85] C. R. Ottermann, E. T. Boschitz, W. Gyles, W. List, R. Tacik, R. R. Johnson, G. R. Smith, and E. L. Mathie, Phys. Rev. C **32**, 928 (1985)

[Pil91] C. Pillai, D. B. Barlow, B. L. Berman, W. J. Briscoe, A. Mokhtari, B. M. K. Nefkens, and M. E. Sadler Phys. Rev. C **43**, 1838 (1991)

[Pil92] C. Pillai, D. B. Barlow, R. S. Kessler, B. M. K. Nefkens, J. W. Price, B. L. Berman, W. J. Briscoe, K. S. Dhuga, S. K. Matthews, S. J. Greene. *To be submitted to Phys. Rev. C*

[Gre89] S. J. Greene, LAMPF Safe Operating Procedure no. 141, (1989)

[Gre92] S. J. Greene, private communication.

e81] S. J. Seestrom, Ph. D. Thesis, for the University of Minesota, The Structure of ^{13}C Studied by Pion Scattering Near the [3,3] Resonance, Los Alamos Report: LA-8916-T (1981) Unpublished

[Smi88] G. R. Smith, D. R. Gill, D. Ottewell, G. D. Wait, P. Walden, R. R. Johnson, R. Olszewski, R. Rui, M. E. Sevior, R. P. Trelle, J. Brack, J. J. Kraushaar, R. A. Ristinen H. Chase, E. L. Mathie, V. Pafilis, R. B. Shubank, N. R. Stevenson, A. Rinat, and Y. Alexander, Phys. Rev. C **38**, 240 (1988)

[Str79] K. Stricker, H. McManus, J. A. Carr, Phys. Rev. C **19**, 929 (1979)

[Tay72] J. R. Taylor
Scattering Theory: The Quantum Theory of Nonrelativistic Collisions
Robert E. Krieger Publishing Company, Malabar, Florida (1972)

[Til87] D. R. Tilley, H. R. Weller and H. H. Hasan, Nucl. Phys **A474**, 1 (1987)

[WRG92] W. R. Gibbs, private communication.